Hugo Pedro Martins Carriço Proença

Towards Non-Cooperative Biometric Iris Recognition

University of Beira Interior

Department of Computer Science

October 2006

Hugo Pedro Martins Carriço Proença

Towards Non-Cooperative Biometric Iris Recognition

Thesis submitted to the Department of Computer Science for the fulfillment of the requirements for the degree of Doctor of Philosophy made under the supervision of Doctor Luís A. Alexandre, Assistant Professor at the Department of Computer Science of University of Beira Interior, Covilhã, Portugal

University of Beira Interior
Department of Computer Science
October 2006

Acknowledgements

This is dedicated to everyone that contributed to the achievement of this work. To all of them i let my sincere grateful.

First, I would like to express my gratitude to my supervisor, Doctor Luís A. Alexandre, for his expertise, gentle guidance and encouragement, which ensured that progress was continuously maintained. I am pleased to conclude that our discussions, during the last three years, strongly contributed to the development of this work.

I would like to express my grateful to the University of Beira Interior, specially to my colleagues of the Department of Computer Science, for the enjoyable working environment that they contributed to. Also, to the Institute of Telecommunications - Covilhã Laboratory - for the given support.

I owe particular thanks to the people that contributed for the earliest stage of this work, by offering themselves as volunteers, in the construction of the $UBIRIS$ database, as well to the Optics Center and Center of Multimedia (CREA), both of the University of Beira Interior.

Last, but not least, I would like to thank to all the people close to myself in the last years, for their strong support, encouragement, friendship and love. I am grateful for their understanding for the time during which I was absent due to this research work.

Abstract

Reliable personal recognition is critical to many processes. Nowadays, modern societies give higher relevance to systems that contribute to the increase of security and reliability, essentially due to terrorism and other extremism or illegal acts. In this context, the use of biometric systems has been increasingly encouraged by public and private entities in order to replace or improve traditional security systems. Basically, the aim is to establish an identity based on *who the person is*, rather than on *what the person possesses* or *what the person remembers* (e.g., an ID card or a password).

Within this context, iris is commonly accepted as one of the most accurate biometric traits and has been successfully applied in such distinct domains as airport check-in [107] or refugee control [13]. However, for the sake of accuracy, present iris recognition systems require that subjects stand close (less than two meters) to the imaging camera and look for a period of about three seconds until the data is captured [45]. This cooperative behavior is required in order to capture images with enough quality for the recognition task. However, it strongly restricts the range of domains where iris recognition can be applied, specially those where the subjects' cooperation is not expectable (e.g., criminal/terrorist seek, missing children).

The overcome of this requirement - users' cooperation - is the main focus of this thesis, i.e., the analysis and proposal of methods for the automatic recognition of individuals, using images of their iris and without requiring them any active participation, in order to achieve accurate covert human recognition.

Our main objective is to overcome the users' cooperation constraints in the biometric iris recognition. Profiting from the extremely low probability of false matches observed in the current iris-based biometric proposals, the external iris visibility and the fact that its capture is minimally intrusive, our aim consists in taking a step ahead in the development of a non-cooperative iris biometric recognition system.

However, it is highly probable that images captured at-a-distance, without users cooperation and within highly dynamic capturing environments lead to the appearance of extremely heterogenous images, with several other types of information in the captured iris regions (e.g., iris obstructions by eyelids or eyelashes and reflections). For the terms of our work and of this thesis, all these factors are considered as *noise*.

After analyzing the actual iris recognition methods and finding that they have small robustness to noise factors, our work was oriented to the proposal of more robust iris recognition methods, that must be able to deal with noise and achieve accurate recognition, based in images captured within non-cooperative environments. Essentially, this thesis is related with the purpose of robust noise detection and handling in the iris biometrics, maintaining minimal recognition error rates.

Along this thesis several proposals to increase the iris recognition robustness to noise are described, among which we enhance, first, a method to perform the segmentation of noisy iris images, a method to detect and localize the noise regions that result of non-cooperative imaging settings. Second, using the information about the localized noisy iris regions, we propose methods that deal with those noise regions. A method to compute the quality of each extracted feature is described. This method avoids that the features extracted from typically noisy regions can corrupt the biometric signature. Finally, a feature selection and a new iris classification strategy increase the adaptability of the recognition system to the dynamics of non-cooperative environments whereas localized noise regions that could corrupt the whole biometric signature are avoided.

Our experiments show a significant increase in the recognition accuracy. Moreover, the fact that our proposals can be used together with most of the iris recognition proposals is regarded as a strong point.

Resumo

O reconhecimento automático da identidade de um indivíduo é um processo crítico para um elevado número de acções quotidianas. Presentemente, as sociedades atribuem relevância crescente a sistemas que contribuam para aumentar os níveis de segurança e fiabilidade, essencialmente devido a preocupações com o terrorismo ou outros actos extremistas. Neste contexto, o uso de sistemas biométricos tem sido crescentemente encorajado, quer por entidades públicas ou privadas, com vista a substituir ou aumentar os níveis de segurança tradicionais. Basicamente, o objectivo é estabelecer uma identidade para um individuo, baseado *no que ele é* em vez de *o que ele possui* ou *o que ele sabe* (por exemplo, um cartão de identificação ou uma palavra-passe).

Neste sentido, a íris é comummente aceite como um dos sinais biométricos mais exactos e tem sido utilizada com sucesso em domínios tão distintos como o controlo de entradas em aeroportos [107] ou o registo de refugiados e eleições [13]. No entanto, de forma a atingir os níveis de exactidão pretendidos, os sistemas actuais de reconhecimento de íris exigem que os indivíduos a reconhecer se posicionem perto do dispositivo de captura de imagem (menos de dois metros) e olhem para ele por um período de cerca de três segundos, até que os dados necessários sejam registados [45]. Este comportamento cooperativo é necessário por forma a adquirir imagens com suficiente qualidade, mas restringe a gama de domínios onde a utilização de sistemas biométricos baseados em íris pode ser efectuada (por exemplo, procura de terroristas ou crianças desaparecidas).

Tornar desnecessário o procedimento cooperativo por parte dos indivíduos a reconhecer é o assunto principal desta tese. Nela são descritos e experimentalmente comparados métodos de efectuar o reconhecimento automático de indivíduos, utilizando imagens da sua íris e sem lhes requerer qualquer acto de participação no processo, por forma efectuar o reconhecimento de forma encoberta, sem que os utilizadores sequer se apercebam.

Após a análise dos métodos actuais de reconhecimento biométrico baseado em imagens da íris e tendo observado a sua pouca tolerância a factores de ruído, o nosso trabalho foi

orientado para a proposta de métodos de reconhecimento mais robustos, capazes de lidar com imagens ruidosas e alcançar reconhecimento fiável nessa circunstancias. Essencialmente, esta tese aborda a detecção e tratamento robusto de ruído em imagens de íris para propósitos biométricos, mantendo taxas de erro reduzidas.

Nesta tese estão descritos métodos para aumentar a robustez ao ruído dos algoritmos de reconhecimento de íris, entre os quais realçamos primeiro os métodos para efectuar a segmentação de imagens de íris ruidosas e o método para detectar e localizar regiões ruidosas em imagens de íris segmentadas e normalizadas. De seguida, usando a informação acerca da localização de cada região com ruído, são descritos métodos que lidam com esse tipo de informação. É descrito um método para calcular a qualidade de cada uma das características extraídas para a assinatura biométrica e evitar que as características mais ruidosas possam corromper a assinatura biométrica. Descrevemos ainda métodos de selecção de características e uma nova estratégia de classificação de íris que aumentam a adaptabilidade dos sistemas de reconhecimento aos ambientes onde estão a funcionar, evitando simultaneamente que as regiões ruidosas possam corromper a totalidade da assinatura biométrica.

As experiência feitas mostram um decréscimo substancial nas taxas de erro. O facto das nossas propostas poderem ser utilizadas conjuntamente com a maioria dos algoritmos actuais de reconhecimento de íris é visto como uma vantagem.

Contents

List of Figures

List of Tables

Notation

Symbols

σ	Parameter that controls the shape of some function.
Δ_r	Increment of radius r.
$G_\sigma(r)$	Gaussian kernel of r width and angular aperture σ.
$I_{i,j}$	Intensity of the pixel located at column i and row j.
$I_{\theta,r}$	Pixel intensity of the image represented in polar coordinates with angular and module coordinates θ, r.
M_{pq}	Regular geometric moment of order pq.
$W_{i,j}^L$	Image window centered at position (i, j) with $L \times L$ pixels.
F_{pq}	Feature image resultant of the M_{pq} moments.
$\|.\|$	Absolute value.
$\|\|.\|\|$	Cardinality of a set.

Abbreviations

API	Application Programming Interface
ASM	Angular Second Moment
BATH	University of Bath Iris Image Database
BSMB	Biometric Specific Memory Block
BSP	Biometric Service Provider
CASIA	Institute of Automation Chinese Academy of Sciences Iris Image Database
CBEFF	Common Biometric Exchange File Format
CCD	Charge-Coupled Device Camera
EER	Equal Error Rate
DLL	Dynamic Link Library
DPI	Dots Per Inch
FAR	False Accept Rate
FRR	False Rejection Rate
ICAO	International Civil Aviation Organization
ICE	Iris Challenge Evaluation Iris Database Image
ID	Identification
ISO	International Organization for Standardization
JPEG	Joint Photographic Experts Group Image Format
KNN	K-Nearest Neighbours
LED	Light Emitting Diodes
MAC	Message Authentication Code
MMU	Multimedia University Iris Image Database
NEO	Iris Noisy Factor (eyelids obstruction)
NLO	Iris Noisy Factor (eyelash obstruction)
NLR	Iris Noisy Factor (lighting reflections)
NMB	Iris Noisy Factor (motion blurred)
NOA	Iris Noisy Factor (off-angle)
NOI	Iris Noisy Factor (out-of-iris)
NPF	Iris Noisy Factor (poor focused)
NPS	Iris Noisy Factor (inaccurate segmentation of inner iris border)
NPI	Iris Noisy Factor (partial iris)
NSS	Iris Noisy factor (inaccurate segmentation of inner iris border)
NSR	Iris Noisy Factor (specular reflections)

ROC	Receiver Operating Curve
SB	Signature Block
SBH	Standard Biometric Header
SOM	Kohonen Self-Organizing Maps
TIFF	Tagged Image File Format
UBIRIS	University of Beira Interior Iris Image Database
WVU	West Virginia University Iris Image Database

Chapter 1

Introduction

Reliable personal recognition is critical to many processes. Nowadays, modern societies give higher relevance to systems that contribute to the increase of security and reliability, essentially due to terrorism and other extremism or illegal acts. In this context, the use of biometric systems has been increasingly encouraged by public and private entities in order to replace or improve traditional security systems. Basically, the aim is to establish an identity based on *who the person is*, rather than on *what the person possesses* or *what the person remembers* (e.g., an ID card or a password).

Pattern recognition - the act of taking in raw data and making an action based on the category of the pattern [30] - has been performed by humans for the last thousands of years in order to assure survival. In the computer science compass, it constitutes a field within the machine learning area and contributed in the last decades for the solution of many of our daily problems (e.g., character and speech recognition, medical diagnosis, DNA sequence identification, computer virus and spyware detection).

Biometrics can be seen from a pattern recognition perspective, where some physiological or physical subjects' data is captured in order to output their respective identity. Considering the recent mandates of several governments for the nationwide use of biometrics, it constitutes a grand challenge for the field itself. Pattern recognition systems have never been tried at such large scales nor have dealt with such a wide use of sensitive personal information [52].

Figure 1.1 illustrates the typical structure of a pattern recognition system in its most simplified form. Initially, a sensor gathers the raw data that will be used as source for all subsequent processing. This is usually known as the *data capture*. Common data formats

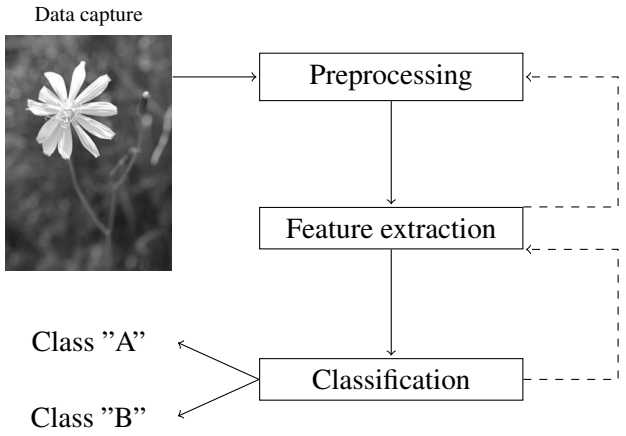

Figure 1.1: Typical stages of a pattern recognition system (adapted from [30]).

are images and sounds recordings, respectively 2-D and 1-D signals.

Next, the data is *preprocessed* in order to simplify further operations and eliminate eventual undesired data (noise). Due to its complexity, this stage is commonly subdivided in several modules, among which the *segmentation* is found. It consists on the isolation of the sections or regions of the captured data and in the localization of each data component. As it is the first stage of any pattern recognition system, it directly deals with the high dynamism of the data capturing devices and conditions and is clearly the one where robustness plays a more important role. Also, the concept of *data normalization*, which makes the data more propitious for further processing, should be referred too.

The *feature extraction* yields a statistical representation of the data. Its goal consists in the characterization of the data by several measures (features) that ideally should be invariant to the input transformations resultant of the dynamic data capture conditions. It is usual to identify irrelevant input transformations, such as translation, scale or rotation changes, projective distortions or deformations in portions of the data. This stage usually demands valuable advices from human experts in the specific knowledge domain and it strongly determines the accuracy of the system itself.

Finally, *classification* takes the features generated in the prior stage and makes use of their information to output a decision, or class. Roughly, it can be made following three distinct approaches: the first is the simplest and is based in the intuitive concept of *similarity*. Template matching is an example. The second is the *statistical* and assumes that the data and its patterns were generated by a probabilistic system. This approach includes methods

based in the Bayes decision rule, K-nearest neighbors and Parzen windows. Finally, the third approach constructs the *decision boundaries* through the optimization of some error criterium. Examples are the Fisher linear discriminant, multi-layer perceptrons, decision trees and support vector machines.

Sometimes, the classification stage is followed by a *post-processing* module, which makes use of the classification output to decide the final action of the system. The concepts of risk and of cost measurement associated with the wrong classification are evolved in this stage.

As knowledge domain, pattern recognition has made considerable achievements in the biometrics field and the results must be considered satisfactory. Under constrained data capturing conditions, systems based in several biometric traits (e.g., fingerprint, iris, retina) achieve minimal error rates.

Within this context, iris is commonly accepted as one of the most accurate biometric traits and has been successfully applied in such distinct domains as airport check-in [107] or refugee control [13]. However, for the sake of accuracy, present iris recognition systems require that subjects stand close (less than two meters) to the imaging camera and look for a period of about three seconds until the data is captured [45]. This cooperative behavior is required in order to capture images with enough quality for the recognition task. However, it strongly restricts the range of domains where iris recognition can be applied, specially those where the subjects' cooperation is not expectable (e.g., criminal/terrorist seek, missing children).

The overcome of this requirement - users' cooperation - is the main focus of this thesis, i.e., the analysis and proposal of methods for the automatic recognition of individuals, using images of their iris and without requiring them any active participation, in order to achieve accurate covert human recognition.

1.1 Motivation and Objectives

As illustrated by figure 1.2, the complexity of designing a biometric system can be seen as a function of three variables. Many application domains require that the biometric system operates on the extreme of one of the three axes and such systems have already been deployed with satisfactory results. Considering that the main premise of the ideal biometric system is to maximize the probability of outputting a correct decision, the grand

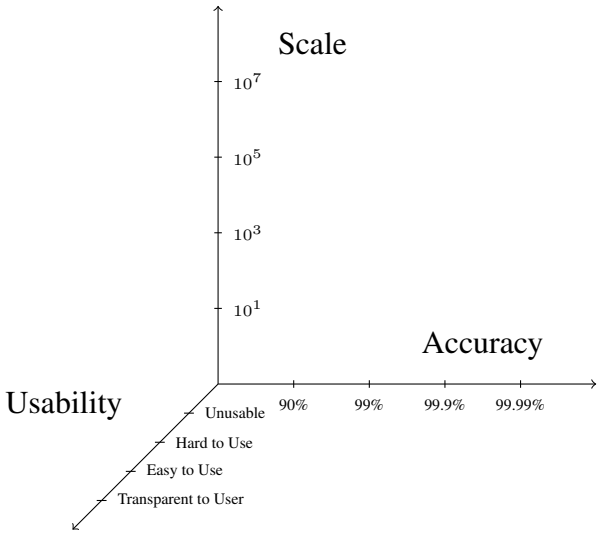

Figure 1.2: Biometric systems characterization [52].

challenge[1] consists in the planning and implementation of a system that could operate on the extremes of all the three axes simultaneously, which contribute for the widespread adoption of biometrics. The fundamental obstacles that must be overcome were the main motivation of our research work and of this thesis.

As stated before, iris recognition is presently used for several purposes with very satisfactory results. Under rigid image capture conditions it is possible to obtain good quality images and achieve impressing accuracy, with very low error rates. However, these error rates substantially increase, specially the false rejections, when the images do not have enough quality and the captured irises contain several other types of information. This is a problem commonly identified by several authors (e.g., [120], [67] and [116]). Therefore, for the sake of accuracy, present iris recognition systems require the subjects' cooperation, which can be regarded as a weak point concerning users comfort and the range of domains where iris recognition could be applied.

Our main objective is to overcome the users' cooperation constraints in the biometric iris recognition. Profiting from the extremely low probability of false matches observed in the current iris-based biometric proposals, the external iris visibility and the fact that its capture is minimally intrusive, our aim consists in taking a step ahead in the development of a biometric system that operates simultaneously in the extremes of the three axes represented in figure 1.2 .

[1] A fundamental problem in science and engineering with broad economic and scientific impact [52].

This type of system will significantly broaden the range of domains where biometrics can be applied, specially to those where the subjects cooperation is not expectable or those where the probability of counterfeit measures by malicious users demands strong attention.

It is highly probable that images captured at-a-distance, without users cooperation and within highly dynamic capturing environments lead to the appearance of extremely heterogenous images, with several other types of information in the captured irises regions (e.g., iris obstructions by eyelids or eyelashes and reflections). For the terms of our work and of this thesis, all these factors are considered as *noise*.

After analyzing the actual iris recognition methods and finding that they have small robustness to noise factors, our work was oriented to the proposal of more robust iris recognition methods, that must be able to deal with noise and achieve accurate recognition, based in images captured within non-cooperative environments. Essentially, this thesis is related with the purpose of robust noise detection and handling in the iris biometrics, maintaining minimal recognition error rates.

1.2 Contributions

Figure 1.3 gives a block diagram that overviews the main contributions of our research work and of this thesis. Our proposals are represented and the publications that resulted from each stage of our work identified. They include:

- the discussion and comparison between the most common biometric traits, as well the revision of the state-of the art of iris recognition, contained in chapter 2.

- the construction of a new iris image database [89], freely available through the web for research purposes. As described in chapter 3, this database has characteristics that clearly distinguish it from the remaining public and free ones and was remarkably well accepted within the academic and research environments.

- the proposal of a more robust iris segmentation method [93], able to deal with highly heterogeneous and noisy iris images. This method is suitable for its application in the non-cooperative image capturing setting.

- the study of the influence that small iris segmentation errors have in the final recognition accuracy and the proposal of a method able to identify these inaccuracies [94].

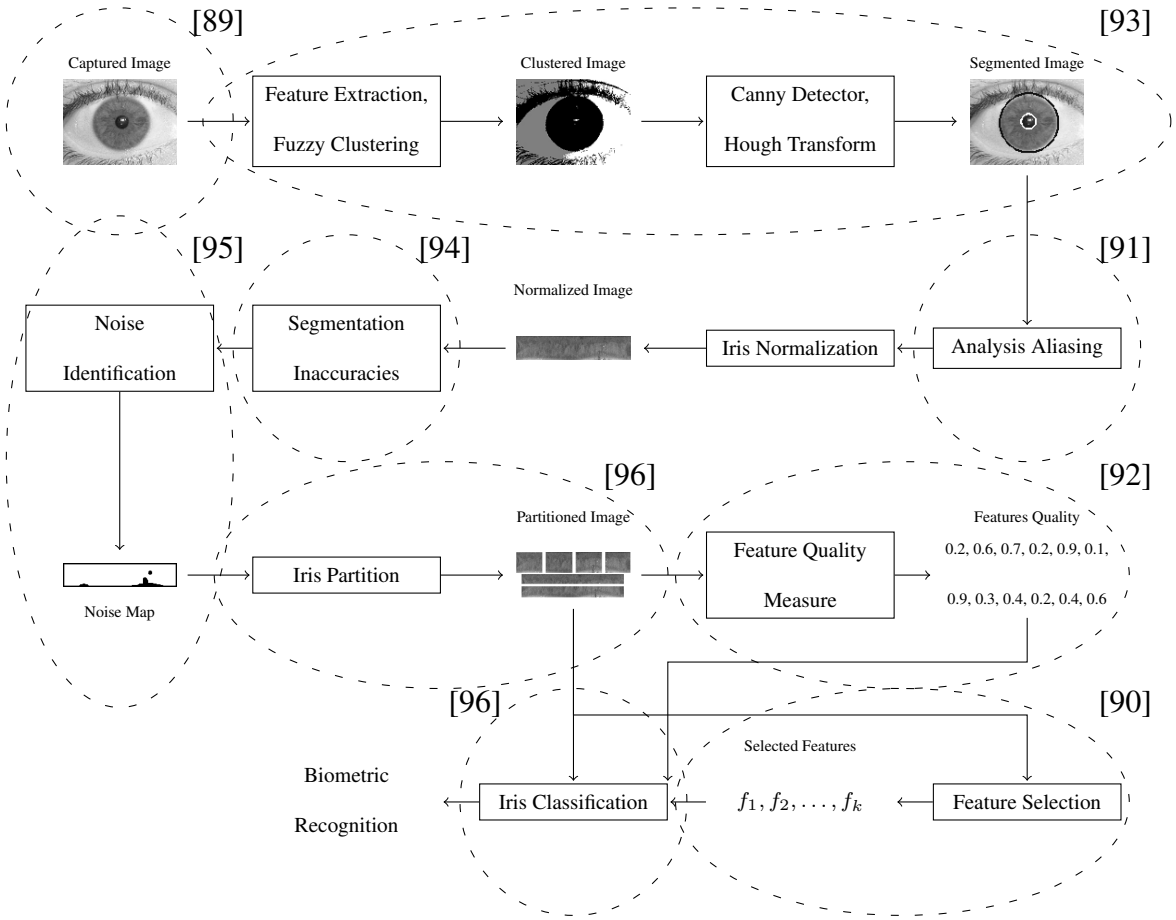

Figure 1.3: Overview of the main contributions of our research work.

- the analysis of the probability of aliasing in the iris normalization stage and the identification of the maximum and minimum sampling rates that must be used in the process to avoid this problem [91].

- the proposal of a method for the identification of noise regions in normalized iris images [95]. This method produces a binary map that can be used in further stages, namely in the feature extraction, comparison and selection.

- the proposal of an iris classification method [96] based on the iris partition, in the independent feature extraction on each partition and in the further iris classification through a fusion rule. This strategy avoids that localized noise regions in the iris images corrupt the whole biometric signature and degrade the recognition accuracy.

- the proposal of a feature quality measure, used in the feature comparison [92] stage,

which avoids that features extracted from predominantly noisy iris regions can be taken into account in the feature comparison.

- the proposal of a supervised feature selection method [90] that operates after the physical installation of the image capturing framework and contributes for the adaptability of the recognition system to the specific characteristics of the image capturing environment where it will operate in.

1.3 Thesis Outline

The remainder of this thesis is organized as follows: chapter 2 introduces the main concepts associated with biometrics, the most common biometric traits, their classification and measures of effectiveness. Further, a review of the iris recognition state-of-the-art is given and some discussion about the non-cooperative biometric recognition is presented. A detailed description of the existent public and freely available iris image databases is given in chapter 3, with particular emphasis on the $UBIRIS$ database. Chapter 4 summarizes the most common iris segmentation methods and reports their small robustness when dealing with noisy images. Based on this, an iris segmentation method for non-cooperative image capturing environments is proposed.

An overview of the most common strategies for noise detection is given in chapter 5, and a detailed description of our proposal is further presented. Chapter 6 describes the problems associated with feature extraction, comparison and selection in the classification of noisy iris images. In order to overcome these problems, three methods that contribute for the recognition robustness and accuracy within noisy environments are presented. Finally, chapter 7 presents the conclusions, summarizes our achievements and points possible directions for further work.

In the appendixes we describe the implemented framework used in the experiments (appendix A) and overview the main characteristics of each data set used in the experiments (appendix B).

Chapter 2

State-Of-The-Art

In this chapter we introduce the basic concepts related with biometrics, namely its main modes of functioning and a possible classification. We compare the most common biometric traits and some measures of the biometrics effectiveness are given.

Regarding iris recognition, we overview the anatomy of the human eye and review the biometric iris recognition state-of-the-art, with particular emphasis to three iris recognition methods, considered relevant and representative of the majority of the proposals. Further, we discuss the non-cooperative iris recognition and describe some of the tasks required to its achievement. Finally, we identify the most common types of noise contained in the iris images captured in non-cooperative imaging setting, that constitute the main obstacle towards the non-cooperative iris recognition.

2.1 Biometrics

This section provides an introduction to biometrics and its history, emphasizing the characteristics that motivated its growing relevance.

Searching for a definition of *biometrics* in both specialized and general information sources, leads to several variants, among which are:

- The study of automated methods for uniquely recognizing humans based upon one or more intrinsic physical or behavioral traits [119].

- A method of verifying an individual's identity based on measurements of the individual's physical features or repeatable actions where those features and/or actions are

both unique to that individual and measurable [111].

- Biometrics is the science and technology of measuring and analyzing biological data. In information technology, biometrics refers to technologies that measure and analyze human body characteristics, such as fingerprints, eye retinas and irises, voice patterns, facial patterns and hand measurements, for authentication purposes [24].

- Biometrics is the science of measuring physical properties of living beings using suitable body characteristics [10].

- Any automatically measurable, robust and distinctive physical characteristic or personal trait that can be used to identify an individual or verify the claimed identity of an individual [121]

As can be seen, notions of $biological$, $measuring$ and $recognition$ are common to any definition, and point to the most relevant characteristics behind the term. From our viewpoint, biometrics can be regarded as the *automated measurement and enumeration of biological characteristics, in order to obtain a plausible quantitative value that, with high confidence, can distinguish between individuals*.

Although less automatized, biometrics has been used - at least - for centuries. In the 14^{th} century, the Portuguese writer João de Barros reported its first known application. He wrote that Chinese merchants stamped children's palm print and footprints on paper with identification purposes [119]. Also, it is believed that the ancient civilizations of Egypt and China performed some type of biometric recognition.

In the western world, until the late 1800s the automatic recognition of individuals was largely done using "photographic memory". In 1883, the French police and anthropologist Alphonse Bertillon developed an anthropometric system, known as Bertillonage [25], to fix the problem of identification of convicted criminals. As illustrated by figure 2.1, this was a quite complex procedure that could take up to twenty minutes and is considered the first scientific system widely used to identify criminals [119]. Its basis was the measurement of certain lengths and widths of the head and body and the recording of individual markings, such as tattoos and scars. However this system's faded when it was discovered that some people share the same measures and several people could be treated as one.

The failure of Bertillonage motivated the use of fingerprinting, which is presently almost standardized worldwide. In 1880, the British scientific journal *Nature* published an article

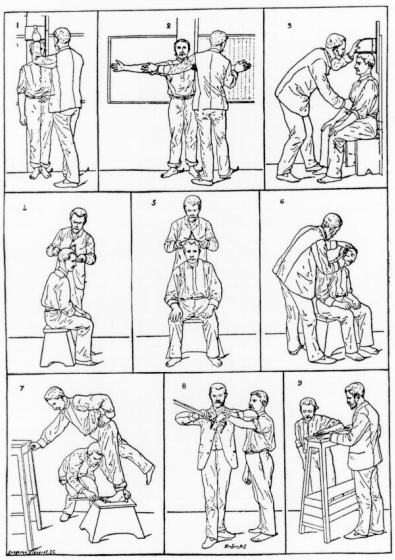

Figure 2.1: Anthropometric system by Alphonse Bertillon [25].

by Henry Faulds and William James describing the uniqueness and permanence of fingerprints. This motivated the design of the first elementary fingerprint recognition system by Sir Francis Galton and improved by Sir Edward R. Henry. Having quickly disseminated, the first fingerprint system in the United States was inaugurated by the New York State Prison Department in 1903 and the first known convicted due to fingerprint evidences was reported in 1911 [3].

Presently, due to increasing concerns associated with security and the war on terrorism, biometrics has considerably increased its relevance. It has moved from a single and almost standardized trait (fingerprint) to the use of more than ten distinct traits. An increasing number of companies, either private or governmental, either with military or civil purposes, invest an enormous amount of human and financial resources into the development of biometric systems. New methods are constantly being proposed and the prices for the hardware and the software technology are continuously falling, making the application of biometrics systems more feasible to low and mid-level budgets. Furthermore, biometrics technology can be seen as a return to the ways of nature, since from centuries humans perform its distinction based in physical and physiological features, such as the facial structure or voice.

2.1.1 Modes of Functioning

Independently of the used trait, the biometric applications follow the procedure illustrated in figure 2.2. The process begins by the data capturing, where the *biometric sample* is acquired. Next, through the feature extraction a *biometric signature* is created, that is further compared with a specific or several biometric signatures registered in the database. These are commonly designated as *biometric templates* and were collected during the *enrollment* process and correspond to a verified subject identity. If the comparison between biometric signatures has enough similarity, it is assumed that both of these were extracted from the same person, otherwise, they must have been extracted from different persons.

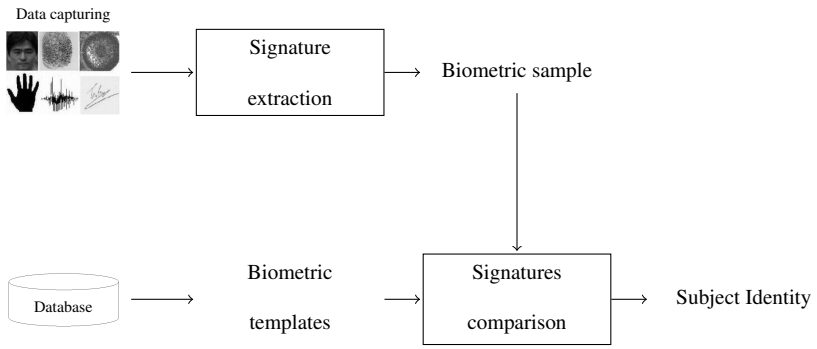

Figure 2.2: Typical stages of a biometric recognition process (adapted from [118]).

The number of comparisons between the biometric sample and templates determines a basic distinctions among the two modes of performing biometric recognition: verification and identification.

In the verification mode, also named as *positive recognition*, the system verifies the authenticity of a claimed enrolled identity, trying to answer the question: *is this person who he/she claims to be*? This requires that, together with the biometric sample, the subject's id must be given to the recognition algorithm. Further, the comparison between the biometric template correspondent to that identity and the sample is performed. If the similarity is high enough, the claimed identity is accepted, meaning that both biometric signatures were extracted from the same person. Otherwise, the identity is denied, meaning that the enrolled and the sample signatures were extracted from different subjects.

The identification mode, often named as *negative recognition*, tries to answer the question: *who is this person*?, or sometimes: *is this person in the database*? After acquiring the required data and extracting the biometric sample, a comparison is made with the N

enrolled identities, in order to find the identity from which the sample was collected. In this mode, it is usual to output a list of the k most probable identities of a biometric sample.

2.1.2 A Classification of Biometric Systems

Biometric systems can be classified according to six perspectives [23], as a function of the characteristics of the recognition procedure itself:

Overt / covert If the user is aware about the acquisition of his biometric data, the application is defined as *overt*; otherwise, is defined as *covert*. This is clearly one of the most concerning characteristics of a biometric system, regarding the privacy issue.

Habituated / non-habituated When the majority of the people that interacts with the biometric system are every-day users, the recognition is performed in the *habituated* mode. If the average frequency of use from each user is low, the recognition is performed in the *non-habituated mode*. This is relevant to the degree of cooperation and training demanded from the users.

Attended / non-attended If the user is observed and guided by supervisors during the process, the biometric recognition is performed *attended*; if not, the use is considered *non-attended*. Obviously, the easy-of-use of the recognition system is much more relevant in the non-attended mode.

Standard / non-standard environment When all the conditions can be controlled and the recognition takes place indoors within constrained conditions, it is considered that the recognition is performed within a *standard* environment; if not, the use is called in *non-standard* environment.

Public / private If the users are not employees of the organization that owns the recognition system, the application is *public*; if the users are employees, the application is called *private*.

Open / closed If the system uses completely proprietary formats, the application is considered *closed*. Otherwise, when the system is able to exchange data with others, it is called *open* and, once again, privacy and legal issues should be addressed.

Based on the above description and on the purposes mentioned in the introductory chapter, this thesis is about the covert, non-habituated, non-attended, non-standard, public and

open iris biometric recognition, which is highly dynamic and propitiates the highest levels of heterogeneity of the data that the system will have to deal with. Obviously, some of these characteristics condition others. For instance, if the recognition is performed covertly, the characteristic habituated/non-habituated is meaningless.

2.1.3 Biometric Traits

This section is devoted to the description of the most common traits that are presently used for biometric purposes. Although there is some discussion about the potential use of other traits as biometric basis, the presented traits are those with higher acceptability by the research community and have commercial applications based in it, which increases its credibility in the biometric compass.

DNA

The deoxyribonucleic acid (DNA) is represented through a one-dimensional code, unique for each person. The only exception are identical twins, which can represent a serious problem, regarding security and forensic applications [21].

DNA identification is based on techniques that use the non-coding tandemly repetitive DNA regions. Humans have 23 pairs of chromosomes containing their DNA blueprint. One member of each chromosomal pair comes from the mother, the other comes from the father. Every cell in a human body contains a copy of this DNA. The large majority of DNA does not differ from person to person, but 0.10 percent of a person's entire genome would be unique to each individual, which represents 3 million base pairs of DNA.

This method is considered to have some drawbacks, as the easy contamination and sensitivity, the impossibility to perform real-time recognition and severe privacy issues, due to the fact of the DNA can reveal susceptibility to some diseases.

Due to many distinguishable characteristics between the DNA and the remaining biometric traits, the discussion about its inclusion as a biometric trait subsists.

Ear

Using ears for the recognition of individuals has been interesting for the research community for, at least, 100 years [58]. During crime scene investigation, ear marks are often used for identification in the absence of valid fingerprints [97]. Although in 1989 Iannarelli [41] analyzed over 10000 ears and concluded about the existence of enough dissimilarities to be used for biometric purposes, the ear uniqueness is questioned.

Commonly, there are at least three methods for ear recognition: taking a photo of an ear, taking *earmarks* by pushing ear against a flat surface and taking thermogram pictures of the ear.

However, just as a face maybe covered with a scarf, the ears maybe partially or completely covered by hair or ear muffles. This implies the requirement of users cooperation, in order to acquire acceptable ear images. Apart from this, rotation, even small, is another common problem.

Despite these problems, there are some advantages that propitiate its use: the requirement of images with smaller dimensions and resolution, its uniform color distribution and less variability with expressions.

Face

The importance of facial features for human recognition cannot be overstated. Facial images are the most common biometric characteristic used by humans to perform personal recognition.

This is a non intrusive and suitable trait to perform covert recognition. Three types of feature extraction methods can be distinguished: generic methods based on edges, lines, and curves; feature-template-based methods that are used to detect facial features such as eyes and structural matching methods that take into consideration geometrical constraints on the features [126].

Although performance of commercially available systems is reasonable, there is still significant room for improvement, since false rejection rate is about 10% and the false accept rate is about 1% [86]. These systems face strong difficulties when the faces are captured under different angles and uncontrolled ambient illumination. Moreover, it is still questioned if a face itself is sufficient basis for reliably recognition of a subject, as, for instance, twins have very similar faces. Another problem could be with counterfeit, as users can dramatically change the appearance of their face, through decorative objects or even through plastic surgeries.

As main advantages, it must be enhanced the high acceptability and universality of face recognition. Users perceive the recognition system as an automated mechanism that exclusively performs a trivial task. Another strong point is the existence of widely used databases, as, for instance, $FERET$ [87], that are used for algorithm benchmarking and facilitate the research and development of new proposals.

Facial Thermogram

It is possible to capture the pattern of heat radiated by the human body with an infrared camera. That pattern is considered to be unique for each person, enabling its potential use for biometric purposes.

It was observed that the capturing of face images through an infra-red camera produces a unique facial signature when heat passes through the facial tissue and is emitted from the skin. These facial signatures are often called facial thermograms. It is claimed that a face thermogram is unique to each individual and is less vulnerable to disguises. Face thermograms may depend heavily on a number of factors such as the emotional state of the subjects, or body temperature, and like face recognition, face thermogram recognition is view-dependent [51].

It is a noninvasive method, although image acquisition is rather difficult when other heat emanating surfaces are near the body.

Another advantage could be the potential use to perform covert recognition, as well its difficult counterfeit. Even plastic surgery, which does not reroute the flow of blood through the veins, is believed to have no effect on the formation of the face thermogram. Face thermogram is a non intrusive biometric technique. Comparing to the visual face recognition several advantages must be enhanced: it can perform the image capturing within very low ambient light, the vascular structure may have more distinguishable information between subjects and less temporal variability within per subject.

In short, this relatively recent technology has an enormous potential for recognition with high security constraints. Although discussion subsists about the uniqueness of a face thermogram, it is believed that this technology will have high impact in the near future, essentially in the covert recognition compass.

Finger Geometry

Although people's hands and fingers are unique, they are not as easily distinguished as other traits, like fingerprints or irises.

Systems that measure hand and finger geometry use a digital camera and light. The aligning of the fingers against several pegs is required to ensure an accurate reading. Then, a camera takes one or more pictures and uses this information to typically determine the length, width, thickness and curvature of the fingers.

As it is considered a simple technique with high user acceptability and minimal intrusion degree, commercial hand geometry-based verification systems have been installed in

hundreds of locations around the world.

Its relatively low level of uniqueness leads that businesses and schools, rather than high-security facilities, typically use hand and finger geometry readers to authenticate users, not to identify them. Disney theme parks, for example, use finger geometry readers to grant ticket holders admittance to different parts of the park.

Finger-based biometric systems have a few strengths and weaknesses. Since fingers are less distinctive than fingerprints or irises, some people are less likely to feel that the system invades their privacy. However, the geometry of many fingers changes over time due to injury, changes in weight or arthritis and can be affected by several other factors (e.g., jewelry).

Fingerprint

A fingerprint is a pattern of ridges and furrows located on the tip of each finger. Fingerprints were used for personal identification for many centuries and the matching accuracy is acceptable. In the past, patterns were extracted by creating an inked impression of the fingertip on paper. Today, compact sensors provide digital images of these patterns.

The recognition process starts by capturing the finger image by direct contact with a reader device, that can also perform some validation procedures to avoid counterfeit measures (check of temperature and pulse). The uniqueness of a fingerprint can be determined by the pattern of ridges and furrows as well as by the minutiae points. These are local ridge characteristics that occur at either a ridge bifurcation or a ridge ending. The feature values typically correspond to the position and orientation of certain critical points, known as minutiae points. The matching process involves comparing the two-dimensional minutiae sample and template patterns.

Among the main advantages for the use of fingerprints are the higher levels of acceptability and their easy of use, as well the fact that it is a matured technology with several years of proven effectiveness. Also, the fact that its technology is legally accepted and that millions of enrolled fingerprints exist, are important.

As disadvantages, it is considered vulnerable to noise and distortion brought on by dirt and twists. Also, since physical contact between the finger and the scanning device is required, the surface can become oily and cloudy after repeated use and reduce the sensitivity. Hygienic considerations must be considered too.

Gait

Although it was originally performed through the use of physical devices attached to the

subjects' legs, the vision-based gait biometrics has recently received a lot of attention, and the first known effort towards recognition was made by Niyogi and Adelson in the early 1990s [84].

The human gait is a periodic activity with each gait cycle covering two strides: the left foot forward and right foot forward strides. Each stride spans the double-support stance to the legs-together stance as the legs swing past each other and back to the double-support stance. Potential information in the basis of gait biometrics can derive from two aspects: shape and dynamics. Based on these two types of information, gait recognition is commonly performed through three distinct approaches: temporal-aligned based (analysis of the time-series features as, for instance, of the whole subject silhouette), static-parameter based (analysis of parameters that characterize gait dynamics, such as stride length, cadence and speed) and silhouette shape-based (emphasizes the silhouette shape similarity and disregards any temporal information) [62].

However, gait vulnerability to changes in the walking surface, walking speed or in the carrying conditions were reported. Due to these, gait-based biometric systems tend to present high false rejection rates. Also, since video-sequence is used to capture the required data, it is considered as one of the most computationally expensive methods [21]. The fact that it can be easily and conscientiously modified by the users, contributes to a higher probability of circumvention.

Hand Geometry

Hand geometry for biometric purposes is used since the early 1980s. Since hand geometry is not thought to be as unique as other biometric traits, its use is often related with low security applications and, sometimes, associated with other security procedures.

A variety of measurements of the human hand, including its shape and lengths and widths of the fingers, can be used as biometric characteristics. Feature extraction computes the widths and lengths of the fingers at various locations of the captured image. These metrics define the feature vector of the user's hand. Current research work seeks for new features that could increment the discriminant capacity between different hands, as well the design of a deformable model for the hand, in order to increase robustness.

As main advantages, it can be referred that the hand geometry-based biometric systems are easy to use and inexpensive. Additionally, operational environmental factors such as dry weather, or individual anomalies such as dry skin, generally have no negative effects on identification accuracy.

However, it should be stressed that its main disadvantage is its relative low discriminating capacity. Also, the hand geometry may not be invariant over the lifespan of an individual, especially during childhood. In addition, an individual's jewelry or limitations in dexterity (e.g., arthritis), may pose further challenges in extracting the correct hand geometry information. Finally, the relative large dimensions of the subjects hands and the requirement of contact to perform recognition makes it unappropriate for certain applications (e.g., laptop computers access) [51].

Hand Vein

It is believed that the pattern of blood veins is unique to every individual, even among identical twins. Moreover, palms have a broad and complicated vascular pattern that has minor variations over lifetime and is not considered intrusive.

An individual's vein pattern image is captured by radiating his/her hand with near-infrared light. The reflection method illuminates the palm and captures the light given off by the region after diffusion through the palm. The deoxidized hemoglobin in the vein vessels absorbs the infrared ray, thereby reducing the reflection rate and causing the veins to appear as a black pattern. This vein pattern is then verified against a preregistered pattern to authenticate the individual.

As veins are internal and have a wealth of differentiating features, attempts to forge an identity are extremely difficult, thereby enabling a high level of security. In addition, the sensor of the palm vein device can only recognize the pattern if the deoxidized hemoglobin is actively flowing within the individual's veins, which increases the counterfeit difficulty [7].

Among the disadvantages, we found the high level of cooperation required and the fact that it demands physical contact between the subject and some part of the system. Apart from the deterioration in the accuracy, this fact is considered an hygienic concern.

Iris

The iris begins to form in the third month of gestation and the structures creating its pattern are largely complete by the eighth month. It is the annular region of the eye bounded by the pupil and the sclera (white part of the eye) on either side. Its complex pattern can contain many distinctive features such as arching ligaments, furrows, ridges, crypts, rings, corona, freckles and a zigzag collarette [21].

Each iris is unique and even irises of identical twins are different. Furthermore, the iris is more easily imaged than retina; it is extremely difficult to surgically tamper iris texture information and it is possible to detect artificial irises. Although the early iris-

based identification systems required considerable user participation and were expensive, efforts are underway to build more user-friendly and cost-effective versions. To obtain a good image of the iris, identification systems typically illuminate the iris with near-infrared light, which can be observed by most cameras yet is not detectable by humans.

Among potential disadvantages for its use remains the weak public acceptance of the iris imaging for biometric purposes, due to old-fashioned thoughts about iridology [51].

The available results of both accuracy and speed of iris-based identification are highly encouraging and point to the feasibility of large-scale recognition using iris information. Due to this and to the above described characteristics, it is common to consider iris as one of the best biometric traits, although this evaluation is dependent of the specific purpose.

Keystroke

It is believed that each person types on a keyboard in a distinguishable way, such that the analysis of the different rhythms that a subject types in the keyboard can be used for its recognition.

This technology examines either dynamics as speed and pressure, the length of time each key is held down, the time elapsed between hitting certain keys and the tendencies to switch between a numeric keypad and keyboard numbers. The extracted features are statistical in nature and specifically designed to characterize the keystroke dynamics over writing samples of 200 or more characters. Most of these are averages and standard deviations of key press duration times and of transition times between keystroke pairs, such as digraphs [117].

The main advantage of the use of keystroke-based biometrics is its potential for continuous monitoring [121]. Oppositely to other traits, the keystroke information can be continuously analyzed by the recognition system, decreasing the probability of active counterfeit measures. Moreover, since users are accustomed to authenticating themselves through usernames and password, most keystroke biometric methods are completely transparent and are well accepted by users.

Among potential disadvantages, privacy concerns must be considered, as the way a subject strokes can be used to infer information about its potential rentability and work effectiveness, for instance [21].

Odor

Olfaction has an extremely high importance in the human being. Since it is one of the five main senses, many philosophers and scientists have tried to comprehend the sense of smell. It is a difficult task, because people often have problems with finding words even to

describe their smell sensations. The main problem, associated with odor perception is that there is no physical continuum as sound frequency in hearing or Newton's circle in color vision [57].

The odor biometrics is based on the fact that, virtually, each human smell is unique. Common sensorial systems are composed by three main stages: calibration, recording and restoration. The first is continuously performed in order to establish a baseline response, denoted as "response to fresh air". Later, when the signal suffers significant changes, the recording of the subject's data is performed and the final stage corresponds to the time required to restore the sensor to the initial stage [2].

Apart from being potentially affected by deodorants or perfumes, it is claimed that the human odor is strongly affected by seasonal habits, diets or medication treatments. Moreover, the use of body odor sensors brings up the privacy issue as the body odor carries a signifiable amount of sensitive personal information and it is possible to diagnose diseases or activities of the last hours [99].

Palmprint

Similarly to the widely used fingerprints, the palms of the human hands contain unique patterns of ridges and valleys. Since a palm is larger then a finger, a palmprint is expected to be even more distinguishable than a fingerprint.

Palmprint scanners need to capture a larger area with similar quality as fingerprint scanners, which makes them more expensive. Typically, the analysis of the palm's principal lines, wrinkles, and textures is performed. These line structures are stable over the human lifetime and normally people do not feel uneasy to have their palmprint images captured.

Therefore, palmprint recognition offers promising future for medium-security access control system. Although this is not as stabilized and matured as the fingerprint technology, several research studies have been made with the purpose of extracting higher discriminating features from the palmprint information. Presently, there are two popular approaches to palmprint recognition. One transforms palmprint images into specific transformation domains and apply texture-based analysis methods (Gabor filters, wavelets decompositions). The other approach applies a technology close to the one used for fingerprint: extract the main lines and creases from the palm and further perform the comparison between the minutia information (e.g., through graph matching).

Compared to other biometric traits, the facts that a higher level of cooperation is demanded to users and the required physical contact between the users and the capturing

device, should be regarded as disadvantages. Also, the fact that the human hand is a fundamental tool for the majority of the people increases the probability of physical damages or diseases.

Retina

Retinal scan measures the blood vessel patterns in the back of the eye. The pattern formed by veins beneath the retinal surface in an eye is stable and unique and is, therefore, feasible for recognition. Digital images of retinal patterns can be acquired by projecting a low intensity beam of visual or infrared light into the eye and capturing an image of the retina using optics similar to a retinoscope. The fact that the retina is small, internal, and difficult to measure makes the capturing of its image more difficult and with higher demanded efforts to users than most of the other traits

Retina matching is accomplished either through 2D or 3D image processing techniques. Retina information procedures usually apply edge enhancing techniques and vessel crossings localization. Other techniques rely on the identification of vessels using adaptive thresholding techniques, followed by graph-matching techniques that find the best match between the vessels localization [71] [39].

Since it is protected in the eye itself, and is not easy to change or replicate the retinal vasculature, this is considered as one of the most secure biometric traits. Retina based systems are used for high security applications, as the access to prisons [51].

Oppositely, because users perceive the technology as intrusive, unfriendly and with high cooperative demands, this type of biometric trait has not gained high popularity. [121]. Also, it is accepted that retinal vasculature can reveal some medical conditions (e.g., hypertension or diabetes), which is another factor deterring the public acceptance of retinal scan-based biometrics. The high cost should be referred too.

Signature

Signature can be regarded as unique and results from both behavioral and hand geometry variations associated to each subject. The way a person signs his or her name is known to be characteristic of that individual since centuries, although the analysis of the signature dynamics is recent.

There are two major strategies to perform signature recognition: image-based and dynamics analysis. The first approach is the most classical and is based on the visual appearance of the signature. The latter analyzes both speed, direction and pressure of writing, stroke order and its major weak point results of the specific hardware dependence [121].

There are, at least, three advantages over other biometric techniques: it is a socially accepted identification method already in use in bank and credit card transactions, most of the new generation of portable computers and personal digital assistants use handwriting as main input channel and, oppositely to finger, iris or retina patterns, a signature may be changed by the user, similarly to a password [76].

However, the use of signature-based biometrics has several weaknesses. Individuals with muscular illnesses and people who sometimes sign with only their initials might result in high false rejection rates. Often, signatures dramatically change over a period of time and are influenced by physical and emotional conditions of the subjects. Additionally, since many users are unaccustomed to signing on a tablet, some subjects' signatures may differ from their signatures on ink and paper, increasing the potential for false rejection [76].

Voice

Oppositely to the majority of the biometric traits, that are image-based, voice possesses the singularity of dealing with acoustic information. The most relevant features of a subject's vocal pattern are determined by physical characteristics as the vocal tracts, mouth, nasal cavities and lips shape. These are low varying features over adult lifetime, although the individual behavior and social environments can highly influence the subject's voice.

As described by Delak and Grgic [21], feature extraction techniques typically measure formants or sound characteristics unique to each person's vocal tract and the pattern matching algorithms are similar to those used in the face recognition.

Speech-based authentication is currently restricted to low-security applications because of the high variability in an individual's voice and poor accuracy performance of typical speech-based authentication systems [51].

As advantages, the fact that most existing voice-based systems are designed for use with standard telephone networks, makes it possible to support a broad range of deployments for voice based biometric applications [68]. This turned the technology as the focus of considerable efforts by the telecommunication industry and by the United States government intelligence community, which continues to work on improving its reliability [121].

2.1.3.1 Factors that Influence the Biometric Traits

According to Matyas Jr. and Riha [53], every biometric system depends on the features, whether genotypic or phenotypic it is based on. Similarly to Daugman [19], authors divide the biometric traits into two types. *Genotypic* refers to the traits that are defined by the

genetic makeup of the individual and do not change over time. *Phenotypic* refers to the actual expression of a feature, through the interaction of genotype, its development and surrounding environment.

According to these, all biometric traits can be placed somewhere along the continuous line with genotypic and phenotypic endpoints, with some traits placed firmly at either extreme (e.g., signature dynamics at the phenotypic extreme) and others somewhere in the middle (e.g., face). The origin of the biometric traits is relevant due to its influence on the systems' error rates. For instance, the dynamics of the phenotypic features over time strongly increases the false rejection rates, while the fact that identical twins share their genetic code sets limits upon the false acceptances.

Fried [33] and A. Bromba [10] classified the origin of the biometric traits into three different types: *genotypic* are traits that are defined by the genetic individual constitution, *randotypic* are those formed early in the development of the embryo, and claimed that the shape of these are distributed randomly through the entire population. Usually the latter are considered the most valuable features for biometric purposes due to the necessity of absolute uniqueness feature sets per subject. Finally, *behavioral* traits are those aspects that a subject develops through training or repeated learning.

The analysis of these variants enabled us to establish a parallelism between the phenotypic and randotypic-behavioral trait types. The latter can be seen as two sub classes of the former and specify the type of interaction between subject and environment. If it was formed with subject conscientiousness, it is behavioral, otherwise is randotypic.

Further, we analyzed the classification of the above described proposals and established our own classification for the origin of the biometric traits, following the schema proposed by Fried and Bomba. The first column of table 2.1 identifies the biometric trait and the others contain the influence of the respective type on the trait. Values are percentile and "100%" and "0%" denote, respectively, maximum and minimum influence, according to the above described information sources.

2.1.3.2 Comparison Between the Most Common Biometrics Traits

Following the proposal of Jain *et al.* [50], biometric systems can be evaluated regarding seven parameters: uniqueness, universality, permanence, collectability, performance, acceptability and circumvention.

Trait	Genotypic	Randotypic	Behavioral
DNA	48%	48%	4%
Ear	40%	40%	20%
Face	40%	40%	20%
Facial Thermogram	20%	50%	30%
Finger Geometry	25%	62.5%	12.5%
Fingerprint	25%	62.5%	12.5%
Gait	30%	10%	60%
Hand Geometry	25%	62.5%	12.5%
Hand Vein	45%	45%	10%
Iris	1%	98%	1%
Keystroke	1%	1%	98%
Odor	37.5%	25%	37.5%
Palmprint	25%	62.5%	12.5%
Retina	1%	98%	1%
Signature	1%	1%	98%
Voice	42%	29%	29%

Table 2.1: Factors of influence of the biometric traits.

The *uniqueness*, often designated as accuracy, distinctiveness or singleness, is probably the most relevant characteristic of a biometric trait. It measures the degree of dissimilarity of the trait between individuals and its capacity of being separable. This feature strongly determines the probability of false acceptances by the system. *Universality* measures the scope of the trait, the number of people where it occurs. Obviously, the optimal biometric trait should occur in as many people as possible. *Permanence* is the quality of being immutable over time, measuring the probability of the biometric trait suffering significant changes over lifetime. This parameter has strong impact in the false rejection rates of the system. *Collectability* or measurability, is the characteristic that expresses the technical and humane easiness in the capture of the relevant trait information. This value plays a role in the users' comfort, which can easily dictate between the biometric system adoption or rejection. The *performance* as to do with the time required to perform the biometric

recognition, once the data is captured. It is relevant in order to distinguish between the computational requirements of the recognition process. *Acceptability* or intrusiveness, is a measure related with socio-cultural users' concerns, as well as with privacy concerns associated with the data capturing. Finally, the *circumvention* measures how easy it is to counterfeit the system, which has high relevance in the security compass.

Trait	Uniqueness	Universality	Permanence	Collectability	Performance	Acceptability	Circumvention
DNA	87%	95%	94%	19%	19%	15%	55%
Ear	46%	58%	85%	50%	53%	100%	50%
Face	44%	92%	50%	84%	25%	99%	37%
Facial Thermogram	95%	100%	25%	100%	69%	85%	100%
Finger Geometry	23%	58%	70%	75%	47%	70%	50%
Fingerprint	78%	47%	91%	62%	98%	49%	71%
Gait	25%	50%	25%	100%	21%	100%	50%
Hand Geometry	54%	57%	54%	78%	50%	67%	59%
Hand Vein	57%	52%	53%	52%	50%	56%	97%
Iris	96%	93%	97%	62%	98%	50%	95%
Keystroke	17%	23%	28%	56%	25%	67%	50%
Odor	70%	89%	85%	25%	21%	50%	37%
Palmprint	96%	50%	100%	50%	97%	50%	50%
Retina	94%	86%	66%	29%	98%	23%	100%
Signature	35%	39%	34%	83%	23%	97%	33%
Voice	39%	49%	31%	59%	23%	99%	33%

Table 2.2: Comparison between the most common biometric traits (adapted and averaged from [49], [125], [61], [10], [80], [42], [40], [46], [122] and [110]).

Table 2.2 contains a comparison between the most common biometric traits. The classifi-

cation of each item is denoted in percentage and "100%" and "0%" correspond respectively to the *best* and *worst* values in any of the items. Each value was obtained through averaging and weighting of the classifications proposed in [49], [125], [61], [10], [80], [42], [40], [46], [122] and [110]. Obviously, the attributed weight to each of the classifications is subjective. We considered the authors reputation, the type of publication and the justifications presented for each classification. Nevertheless, the analysis of this table enables an overall perspective about the main strong and weak points of each trait. Although this discussion depends of the analyzed sources of classification, there are observations that can be taken with minimal subjectivity. First, the division between *soft* and *hard* biometrics, based in the uniqueness of the biometric trait. Signature and voice can be classified as soft biometric traits, as their uniqueness is strongly discussed in the research community. However, similarly to the analysis of the gender, weight and eye color, these biometric traits are easily collected, making them propitious for the use in systems with low security requirements or with minimal probability of counterfeit measures. At the other extreme are those traits with guaranteed uniqueness, as iris, retina and facial thermogram. Since these are usually more difficult to collect, the capture of these traits has often low acceptability, due to cultural, political or religious concerns.

For the purposes of our work, one of the most important features is the ability to perform covert recognition, which can be performed by the ear, face, facial thermogram, gait, iris and odor traits. Among these, iris and facial thermogram must be enhanced, as they provide higher uniqueness and circumvention values. However, the thermal data is often considered low permanent, with the correspondent impact in the false rejection rates.

Apart from being the biometric trait with highest average value between the seven analyzed parameters (84.42%), its simultaneous high levels for uniqueness, permanence, universality and circumvention turned the iris into the most appropriate for our work and a natural choice towards the non-cooperative biometric iris recognition.

2.1.4 Effectiveness Measures

The objective evaluation and comparison between biometric systems can be a hard task. Apart from being impossible to give a single value that reflects the accuracy of a recognition system, to get comparable results it is required that the same measures of accuracy are used, under the same data sets and following the same protocol. For different biometric traits, this is obviously an unsurmountable task, although several measures provide information about

the accuracy of a single biometric recognition system.

Let $NRAI$ and $NSRI$ be, respectively, the total and well succeeded recognition processes performed by impostors. The proportion between these two value produces the $False\ Acceptance\ Rate$ (FAR), which measures the probability of confusing two identities. Obviously this is the most important measure, regarding security.

$$FAR = \frac{NSRI}{NRAI} \tag{2.1}$$

Simultaneously, a system may be evaluated by the probability that the identity of the valid users is denied. Let $NRRV$ and $NRAV$ be, respectively, the total and failed recognition attempts performed by registered users. The proportion between these values produces the $False\ Rejection\ Rate$ (FRR), which has great relevance in the comfort that the biometric system affords to its users.

$$FRR = \frac{NRRV}{NRAV} \tag{2.2}$$

FAR and FRR are dual measures and meaningful exclusively when presented together. Its values are determined by the level of similarity T required to accept a comparison between biometric signatures. As this value decreases, there is respectively a direct and inverse correspondence in the FRR and FAR. According to the requirements and priorities of the biometric application, it is an obligation of its administrators to adjust the value of T and, simultaneously, approximating the expectable values of the FAR and FRR.

Figure 2.3 illustrates two typical ways of measuring the accuracy of a biometric system. Figure 2.3a denotes the values for the FAR (dashed line) and FRR (continuous line) as function of the value of T (demanded dissimilarity to match a comparison). The point where the two lines intersect is a very common measure of the biometric systems accuracy: the $Equal\ Error\ Rate$ (ERR). This value gives the average error rate when the FAR and FRR are approximately equal and is probably the only value with individual significance. Figure 2.3b illustrates a $Receiver\ Operating\ Curve$ (ROC), which reflects the variability of both the FAR and FRR according to each other. The area under the curve is also regarded as an accuracy measure.

The described measures are the most common in the evaluation of the recognition accuracy and are meaningful in the verification mode. The following measure is suitable for the identification mode and is based on the number of wrong identification attempts ($NWIA$) and on the total identification attempts (NIA). The $False\ Identification\ Rate$ (FIR) is

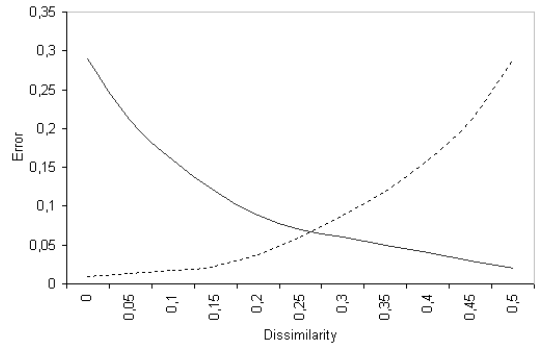

(a) *Typical FAR (dashed line) and FRR (continuous line) curves, as functions of the maximum dissimilarity T to match a comparison between iris signatures.*

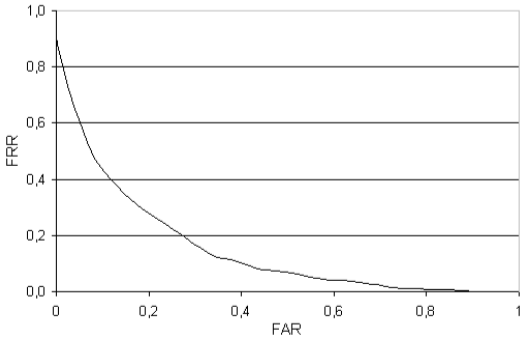

(b) *Typical ROC curve, reflecting the relation between the FAR and FRR.*

Figure 2.3: Illustration of two curves that typically measure the accuracy of a biometric system.

given by:

$$FIR = \frac{NWIA}{NIA} \tag{2.3}$$

In a somewhat distinct perspective, the following two measures represent the probability of the failure of the recognition process even before its start, due to inappropriate data capturing. The $Failure\ to\ Enroll$ (FTE) and $Failure\ to\ Acquire$ (FTA) are respectively the measures for probability of failure in the data capturing in the enrollment and in the recognition stages. This distinction gains higher relevance in the non-cooperative setting, due to the less constrained data capturing conditions. Let NEA and $NFEA$ denote respectively the total and failed enrollment attempts. The FTE is given by:

$$FTE = \frac{NFEA}{NEA} \tag{2.4}$$

Similarly, let NCA and $NFCA$ denote respectively the total and failed recognition processes due to inappropriate data capturing. The FTA is given by:

$$FTA = \frac{NFCA}{NCA} \tag{2.5}$$

2.2 Iris Recognition

This section is totally related with the utilization of the iris for biometric purposes. We start by an overall description of the eye's anatomy followed by the identification of the most important regions of the human iris. Further, we identify the most typical stages of common iris recognition proposals and describe the most relevant approaches to each of these stages.

2.2.1 Eye and Iris Anatomy

In this sub-section we start with the description of the human eye anatomy, followed by a highly detailed description of the iris, which is the most relevant part of the eye for the purposes of our work.

2.2.1.1 Eye Anatomy

Figure 2.4 schematizes the most relevant parts of the human eye [108]. As with the majority of the mammals, the eye is roughly globular in shape and hollow and can be divided into two main segments - anterior and posterior - which are surrounded by a leathery envelope that acts as a protection: the *sclera*. This is a tough and fibrous tissue consisting of highly compacted and interweaved fibers and bands. When seen from the front, sclera is commonly, and incorrectly, referred to as the white of the eye [9].

Regarding the anterior eye segment, it extends internally from the anterior hyaloid face forward and is externally demarcated by the limbus. It includes the structures in front of the vitreous humor: the cornea, iris, ciliary body and lens. The *cornea* acts as a window at the front of the eye and provides about 85% of the focusing power of the eye. It is made up of a tissue similar to that of sclera, with the relevant exception of having no blood vessels. Just beneath the cornea is a fluid-filled space called the *anterior chamber*, which bathes the whole of the anterior segment providing nourishment and removal products to the lens and cornea. The *ciliary body* is the source of the above mentioned fluid and houses the muscular fibers that enable the eye to focus. Overlying the lens, there is a structure with an opening in the whole: the iris. It is made of an elastic tissue and its function is to control the amount of light that enters the iris whole: the pupil. Behind the iris is the lens, which role consists in assuring that the light rays some to a sharp focus on the retina.

The posterior eye segment comprises the back two-thirds of the eye and includes the vitreous humor, retina, choroid and optic nerve. The first is the the clear aqueous solution

that fills the space between the lens and the *retina*, which is a thin layer of nervous tissue - supplied with oxygen and cleaned by the *choroid* - that is responsible for gathering the light and perform its conversion to the electrical signals that are sent through the *optic nerve* to the brain. This process gives us the sense of light and the ability to see and interpret shapes, colors and dimensions.

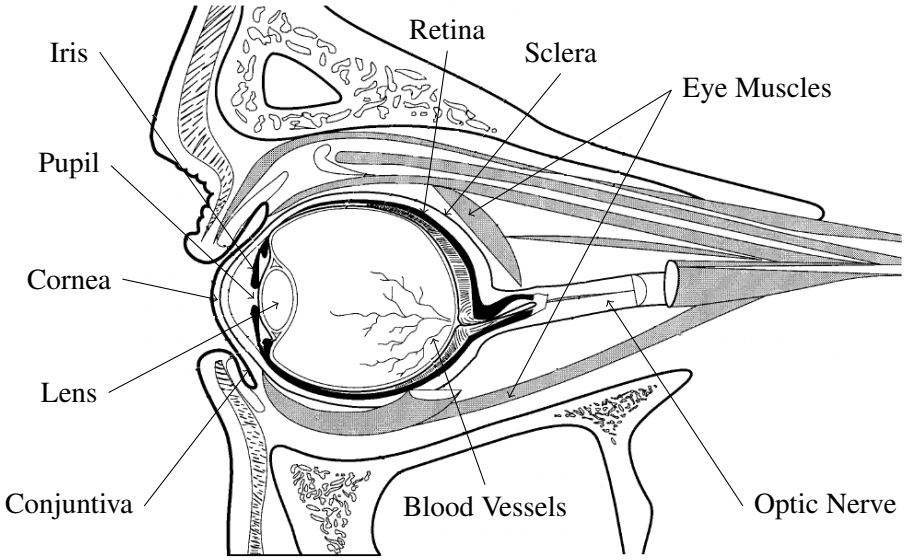

Figure 2.4: Anatomy of the human eye (adapted from [115]).

2.2.1.2 Iris Anatomy

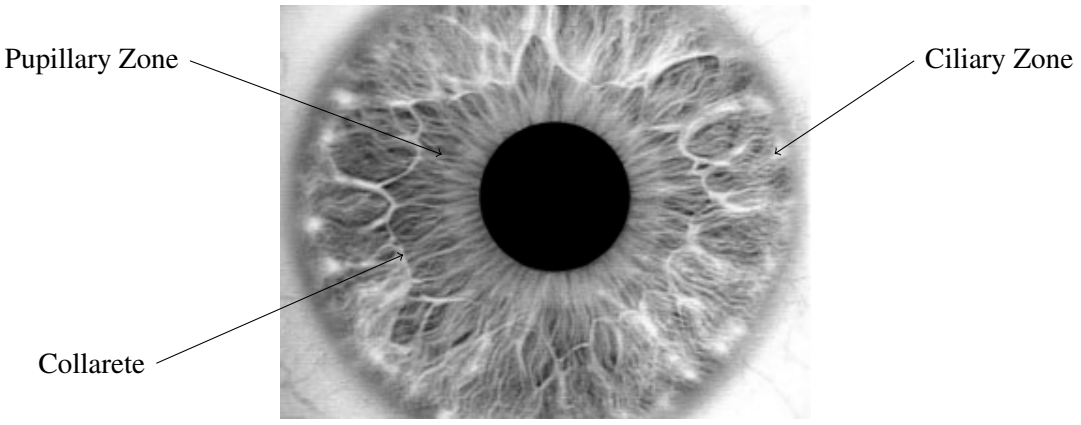

Figure 2.5: Morphology of the human iris (adapted from [102] and [77], picture from [17]).

Illustrated by figure 2.5, the iris consists of a pigmented fibrovascular tissue, known as *stroma*. The stroma connects a sphincter muscle (with the purpose of contract the pupil) and a set of dilator muscles to open it. It is divided into two major regions: the *pupillary* and the *ciliary zone*.

The pupillary zone is the inner portion of the iris whose edges form the pupillary iris border. The ciliary zone is the outer portion of the iris, which extends itself into the iris origin in the ciliary body. The region that separates the pupillary and scleric portions is designated as the collarette. This is typically the region where the sphincter and dilator muscles overlap.

The iris begins to form during the third month of gestation and the structure is complete by the eight month, although pigmentation continues into the first year after birth [77]. The visible features of the iris arise in the trabeculum, which is a meshwork of connective tissues with arching ligaments, crypts, contraction furrows, a corona and pupillary frill, coloration and freckles. Although the anterior layer covering the trabecular framework creates the predominant iris texture seen with visible light, additional discriminating information can be given by the location of all of these sources of radial and angular variation. Together, as mentioned by Daugman [17], they provide a distinguishable and unique signal.

The texture and minutia of the iris is believed to have high random morphogenesis and no genetic penetrance in its expression. Since the appearance of each iris depends of the initial conditions in the embryonic mesoderm from which it develops, the phenotypic of two iris with the same genetic genotype (e.g., identical twins or the both eyes of a subject) have distinguishable minutia. Past studies about the iris texture concluded that the inter-subject variability of its pattern spans about 250 degrees-of-freedom and have an entropy of about 3.2 bits per square-millimeter [17].

These biological characteristics and the chaotic appearance of the iris patterns turned it as one of the most suitable traits for biometric purposes. As discussed in the comparison between the most common traits, iris is generally accepted as one of the most promising biometric traits and is the subject for the development and proposal of many biometric recognition algorithms. In the following section, we detail the typical iris recognition stages and present its state-of-the-art, with emphasis to the almost standard Daugman's recognition method that, apart from being the first proposed, is the basis for the large majority of the deployed and commercial iris recognition systems.

2.2.2 Typical Stages of Iris Recognition

Figure 2.6 illustrates the typical stages of iris recognition systems. In spite of the specificities of the different proposals, they share the given structure. The initial stage deals with iris segmentation. This process consists in localizing the iris inner (pupillary) and outer (scleric) borders, assuming either circular or elliptical shapes for both of the borders.

In order to compensate the variations in the pupil size and in the image capturing distances, it is common to translate the segmented iris region into a fixed length and dimensionless polar coordinate system. This stage is usually accomplished through the method proposed by Daugman [18].

Regarding feature extraction, iris recognition approaches can be divided into three major categories: phase-based methods (e.g., [18]), zero-crossing methods (e.g., [8]) and texture analysis based methods (e.g., [120]).

Finally, the comparison between iris signatures is made, producing a numeric dissimilarity value. If this value is higher than a threshold, the system outputs a *non-match*, meaning that each signature belongs to different irises. Otherwise, the system outputs a *match*, meaning that both signatures were extracted from the same iris.

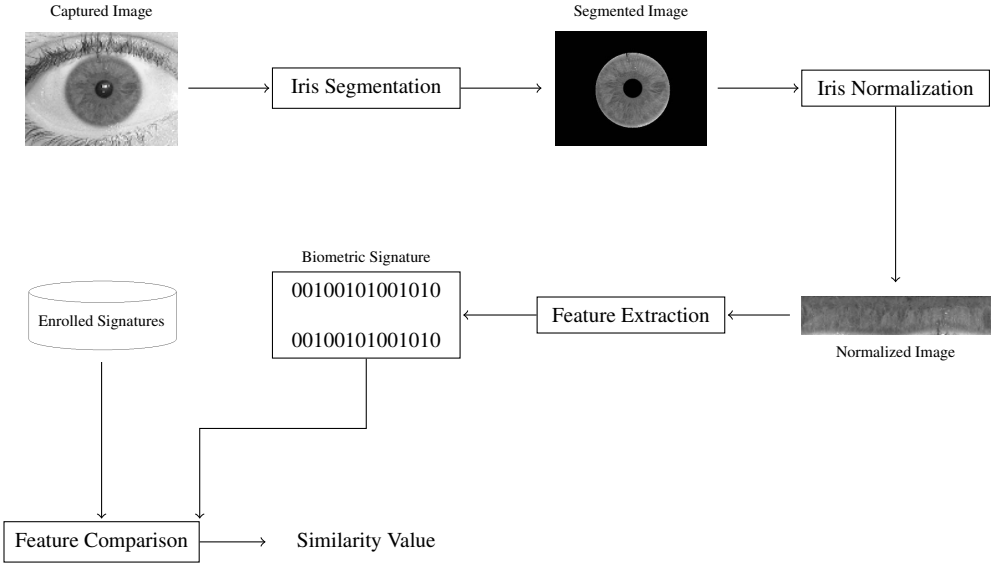

Figure 2.6: Typical stages of the iris recognition.

Having overview the main stages of iris recognition and mentioned some of the most relevant approaches, in the next sub-sections, we describe some usual approaches to perform

each of the above identified stages.

2.2.2.1 Iris Segmentation

In 1993, J. Daugman [18] presented one of the most relevant methods, constituting the basis of the majority of the functioning systems. Regarding the segmentation stage, this author introduced an integro-differential operator to find both the iris inner and outer borders. This operator remains actual and was proposed in 2004 with minor differences by Nishino and Nayar [83].

Similarly, Camus and Wildes [11] and Martin-Roche *et al.* [70] proposed integro-differential operators that search the $\mathbb{N}^3$ space, with the objective of maximizing the equations that identify the iris borders.

Wildes [120] proposed iris segmentation through a gradient based binary edge-map construction followed by circular Hough transform. This is the most common method, that has been proposed with minor variants by Cui *et al.* [16], Huang *et al.*[37], Kong and Zhang[55], Ma *et al.*[66], [63] and [67].

Liam *et al.* [59] proposed one interesting method essentially due to its simplicity. This method is based in thresholds and in the maximization of a simple function, in order to obtain two ring parameters that correspond to iris inner and outer borders.

Du *et al.* [29] proposed the iris detection method based on the prior pupil segmentation. The image is further transformed into polar coordinates and the iris outer border is detected as the largest horizontal edge resultant from Sobel filtering. However, this approach may fail in case of non-concentric iris and pupil, as well as for very dark iris textures.

Morphologic operators were applied by Mira and Mayer [74] to obtain iris borders. They detected the pupillary and scleric borders by applying thresholding, image opening and closing.

Based on the assumption that the pixels' intensity of the captured image can be well represented by a mixture of three Gaussian distributions, Kim *et al.* [54] proposed the use of Expectation Maximization [22] algorithm to estimate the respective distribution parameters. They expected that 'Dark', 'Intermediate' and 'Bright' distributions contain the pixels corresponding to the pupil, iris and reflections areas.

2.2.2.2 Iris Normalization

Due to the varying size of the pupil and of the distance and angle of the image capturing framework, the size of the captured irises can have high variations, increasing the complexity of the recognition task. Robust representations for pattern recognition must be invariant to changes in the size, position, and orientation of the patterns. In the iris recognition compass, this requires a representation of the iris data invariant to the dimension of the captured image. This is influenced by the distance between the eye and the capturing device, by the camera optical magnification factor and by the iris orientation, caused by torsional eye rotation and camera angles. As described in [20], the invariance to all of these factors can be achieved through the translation of the captured data into a double dimensionless polar coordinate system. As figure 2.7 illustrates, this translation process is based both in polar (θ) and radial (r) variables.

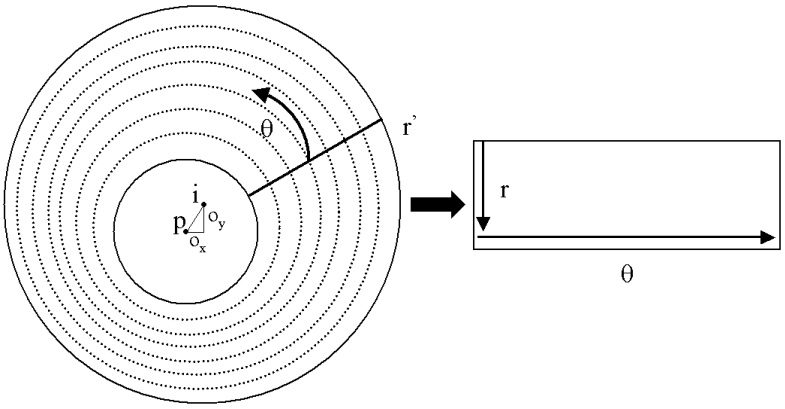

Figure 2.7: Normalization of the iris image through the *Daugman rubber sheet*.

The rubber sheet model assigns to each point on the iris, regardless of its size and pupillary dilation, a pair of real coordinates (r, θ), where r is on the unit interval [0, 1] and θ is an angle in $[0, 2\pi]$. The remapping of the iris image $I(x, y)$ from raw cartesian coordinates (x, y) to the dimensionless non concentric polar coordinate system (r, θ) can be represented as:

$$I(x(r, \theta), y(r, \theta)) \rightarrow I(r, \theta) \tag{2.6}$$

where $x(r, \theta)$ and $y(r, \theta)$ are defined as linear combinations of both the set of pupillary boundary points $(x_p(\theta), y_p(\theta))$ and the set of limbus boundary points along the outer perime-

ter of the iris $(x_s(\theta), y_s(\theta))$ bordering the sclera, which are detected in the iris segmentation stage, as:

$$\begin{cases} x(r,\theta) = (1-r) * x_p(\theta) + r * x_s(\theta) \\ y(r,\theta) = (1-r) * y_p(\theta) + r * y_s(\theta) \end{cases} \tag{2.7}$$

2.2.2.3 Feature Extraction

As stated above, from the viewpoint of feature extraction, recognition approaches can be divided into three major categories: phase-based methods (e.g., Daugman [18]), zero-crossing methods (e.g., Boles and Boashash [8] and Roche *et al.*[70]) and texture analysis based methods (e.g., Wildes [120], Kim *et al.*[54] and Ma *et al.*[66]).

Daugman [18] uses multiscale quadrature wavelets to extract texture phase information and obtain an iris signature with 2048 binary components. Once again, this proposal acted as basis for others with minor differences, as Ma *et al.* [65].

To characterize the iris texture, Boles and Boashash [8] computed the zero-crossing representation of a 1D wavelet at different resolutions of concentric circles. Wildes [120] proposed the characterization of the iris texture through a Laplacian pyramid with 4 different levels (scales).

One of the most common approaches consist in the dyadic wavelet decomposition either using Haar, Mallat or other mother wavelets. This can be found in several proposals, among which are Ali and Hassanien [1], Ma *et al.* [63] and Lim *et al.* [60],

Other creative approaches can be found in Huang *et al.* [38], that used the values resultant of the independent coefficient analysis to characterize the iris texture. Muron *et al.* [78] proposed the codification of the whole information through the power of the Fourrier spectrum. Du *et al.* [29] proposed feature extraction through the computation of invariant local texture patterns. Nam *et al.* [79] proposed the study of the directional properties of the image in order to create a binary signature, through the analysis of the image's second derivatives.

2.2.2.4 Feature Comparison

Although the method chosen to compare between iris signature is highly conditioned by the feature extraction strategy, the feature comparison is generally performed through the use of distance metrics: Hamming (e.g., Daugman [18], Tisse *et al.* [112]), Euclidean (e.g., Huang *et al.* [38]), Weighted Euclidean (e.g., Zhu *et al.* [127] and Ma *et al.* [66]) or methods based

on signal correlation (Wildes [120]).

More specific proposals were given by Lim *et al.* [60], through the utilization of a competitive learning neural network to achieve classification and by Ma *et al.* [63], through a modified nearest neighbor to compare the acquired and the enrolled samples and assign the proper entity.

2.2.3 Some Relevant Iris Recognition Methods

In the following sub-sections we describe with detail some of the most relevant iris recognition methods. Apart from the Daugman's method, that acts as the basis and main comparison term for other proposals, we describe the methods proposed by Wildes [120] and Tan *et al.* [64]. The choice of these methods was motivated by the analysis of the iris recognition literature and by the description of the algorithms with commercial applications [31].

2.2.3.1 Daugman's Method

As described in [18], the Daugman's recognition method is composed by the following stages:

- Iris segmentation. The author describes an integro-differential operator that searches for the maximal difference between the average intensity of circumferences with consecutive radius values. This operator is described in section 4.2.1.

- Normalization. After the segmentation of both iris borders, to compensate the variations in the size of the pupil, we translated the images to dimensionless polar coordinate system through a process known as the *Daugman Rubber Sheet* [18], which is described in section 2.2.2.2.

- Feature Extraction. The iris data encoding was accomplished through the use of two dimensional Gabor filters. These spatial filters have the form:

$$G(x,y) = e^{-\pi[(x-x_0)^2/\alpha^2+(y-y_0)^2\beta^2]}.e^{-2\pi i[u_0(x-x_0)+v_0(y-y_0)]} \tag{2.8}$$

  where (x_0, y_0) defines the position in the image, (α, β) is the filter width and length and (u_0, v_0) specify the modulation, with spatial frequency $w_0 = \sqrt{u_0^2 + v_0^2}$ and direction θ_0=arctan(v_0/u_0).

The real parts of the 2-D Gabor filters are truncated to be zero volume and achieve illumination invariance. For each resulting bit the sign of the real and imaginary parts from quadrature image projections is analyzed and, through quantization, assigned binary values: 1 and 0 respectively for positive and negative projection values.

- Feature Comparison. The feature extraction binarization process allows the utilization of the Hamming distance as the similarity measure for two iris signatures. Given two binary sets with N bits: $A = \{a_1, ..., a_N\}$ and $B = \{b_1, ..., b_N\}$, the Hamming distance is:

$$HD(A, B) = \frac{1}{N} * \sum_{i=1}^{N} a_i \otimes b_i \tag{2.9}$$

being $a \otimes b$ the logical XOR operation. Thus, for two completely equal and different signatures, the value of the Hamming distance will be respectively 0 and 1.

2.2.3.2 Wildes' Method

In [120], Wildes describes a machine vision system for noninvasive biometric assessment. It is divided into three parts: image acquisition, image segmentation and image matching.

- Image Acquisition. Due to its relatively small dimensions, the author considered the image acquisition as one of the major challenges for automated iris recognition. First, it is stressed the importance of acquiring iris images with sufficient resolution and sharpness to support recognition. Second, the requirement of good contrast in the iris pattern, without resorting to a level of illumination that annoys the subject. The captured images must be centered and the artifact (e.g. specular reflections and optical aberrations) should be eliminated as much as possible. Based in these concerns, the author describes an optical framework for the iris capturing from a distance of 20 cm. using a 80 mm. lens.

- Iris Localization. Image acquisition will capture the iris as part of a larger image that also contains data corresponding to the region surrounding the eye. Therefore, it is important to localize that portion of the acquired image that corresponds to the iris. The author performs its contour fitting in two steps. First, the image intensity information is converted into a binary edge-map. Second, the edge points vote to instantiate particular contour parameter values. The edge-map is recovered through a

gradient-based edge detection, that consists of thresholding the magnitude of the image intensity gradient convolved with a two-dimensional Gaussian Kernel G defined by:

$$G(x,y) = \frac{1}{2\pi\sigma^2} e^{-\frac{(x-x_0)^2+(y-y_0)^2}{2\sigma^2}} \tag{2.10}$$

where (x_0, y_0) is the center of the kernel and σ its standard deviation. In order to incorporate directional tuning, the image intensity derivatives are weighted to favor certain ranges of orientation prior to taking the magnitude. Figure 2.8 illustrates edge-maps with (figure 2.8a) and without (figure 2.8b) orientation favors.

(a) Edge-map with vertical orientation favor. (b) Edge-map without orientation favors.

Figure 2.8: Morphology of the human eye.

Regarding the detection of the limbic boundary, the derivatives are weighted to be selective for vertical edges, as the probability for the detection of edges correspondent to eyelids is minor. The voting procedure is realized via the circular Hough transform [43], defined as:

$$H(x_c, y_c, r) = \sum_{j=1}^{n} h(x_j, y_j, x_c, y_c, r) \tag{2.11}$$

where

$$h(x_j, y_j, x_c, y_c, r) = \begin{cases} 1 & \text{if } g(x_j, y_j, x_c, y_c, r) = 0 \\ 0 & \text{otherwise} \end{cases} \tag{2.12}$$

and

$$g(x_j, y_j, x_c, y_c, r) = (x_j - x_c)^2 + (y_j - y_c)^2 - r^2 \tag{2.13}$$

The triple parameter that maximizes H is a reasonably choice to represent the contours of interest, the iris inner and outer borders. Regarding the upper and lower eyelids, they are fitted in a similar fashion using parameterized parabolic arcs in place of the circle parametrization $g(x_j, y_j, x_c, y_c, r)$.

- Pattern Matching. After the identification of the region correspondent to the iris, the final task is to decide if the captured pattern matches a previously enrolled. The author decomposes this task in four parts: alignment, representation, comparison and decision.

  1. Alignment. The author uses an image registration technique to compensate scaling and rotation. It warps the newly acquired image $I_a(x, y)$ into alignment with a database image $I_d(x, y)$ according to a mapping function $(u(x, y),\ v(x, y))$ such that for all (x, y), the image intensity at (x, y) - $(u(x, y),\ v(x, y))$ in I_a - is close to that at (x, y) in I_d. The mapping function (u, v) is taken to minimize

  $$\int_x \int_y \Big(I_d(x, y) - I_a(x - u, y - v)\Big)^2 dxdy \tag{2.14}$$

  while constrained to capture a similarity transformation of image coordinates (x, y) to (x', y'):

  $$\begin{pmatrix} x' \\ y' \end{pmatrix} = \begin{pmatrix} x \\ y \end{pmatrix} - sR(\phi) \begin{pmatrix} x \\ y \end{pmatrix} \tag{2.15}$$

  where s is a scaling factor and $R(\phi)$ a matrix representing rotation by ϕ.

  2. Representation. An isotropic band-pass decomposition is proposed, derived from application of Laplacian of Gaussian filters to the image data. These filters can be defined as:

  $$-\frac{1}{\pi\sigma^4}\Big(1 - \frac{\rho^2}{2\sigma^2}\Big)e^{-\frac{\rho^2}{2\sigma^2}} \tag{2.16}$$

  where σ is the standard deviation of the Gaussian and ρ is the radial distance of the point to the filter center. This procedure can be implemented through a Laplacian pyramid. Given an image I, it is iteratively convolved with a low pass

filter and down sampled by a factor of two in each dimension. This multi scale representation of the image is used as the biometric iris signature. Oppositely to the Daugman's system, this representation is derived directly from the filtered image for size on the order of the dimension of the captured iris image.

3. Comparison. In this stage a procedure based on the normalized correlation between both iris signatures is used. Let A_1 and A_2 be two arrays of size $n \times m$. Also, let μ_1 and μ_2 be respectively the mean of A_1 and A_2 and σ_1 and σ_2 be the standard deviation of A_1 and A_2. The normalized correlation can be defined as:

$$\frac{1}{nm\sigma_1\sigma_2}\sum_{i=1}^{n}\sum_{j=1} n(A_1(i,j)-\mu_1)(A_2(i,j)-\mu_2) \tag{2.17}$$

The author applies the correlations over small 8×8 blocks in each of the four spatial frequency bands resultant from the Laplacian pyramid representation. Further, these values are combined into a single value via the median statistic, yielding four goodness-of-match values.

4. Decision. This stage combines the previously obtained four values into a single accept/reject judgement, through the Fisher linear discriminant. Let n be the number of samples q_i (four comparisons between multi scale measurements), n_A of which are authentics and n_I from impostors. Fisher's linear discriminant defines a weight vector w such that the ratio of intra- and inter-class variance is maximized for the transformed samples $w^T q$. Let μ_A and μ_I be the d-dimensional mean values respectively for $q \in A$ and $q \in I$. A measure of variance within a class C can be given by a scatter matrix with form:

$$S_C = \sum_{q \in C}(q-\mu_C)(q-\mu_C)^T \tag{2.18}$$

In this case, the total within class scatter is given by $S_{intra} = S_A + S_I$. A corresponding measure of the variance between classes can be defined in terms of the scatter matrix $S_{inter} = (\mu_A - \mu_I)(\mu_A - \mu_I)^T$. Thus, the following expression describes the ratio of intra- and inter-class variance of the transformed samples wq:

$$\frac{w^T S_{inter} w}{w^T S_{intra} w} \tag{2.19}$$

Finally, the w that maximizes this ratio is given by:

$$w = S_{intra}^{-1}(\mu_A - \mu_I) \tag{2.20}$$

In order to apply this discriminant to the classification task a separation point must be defined. Values above this point will be taken as derived from class A and values below this point will be taken as derived from class I. The author takes the separation point as the midpoint between the transformed means of the samples from A and I, which can be proven to be optimal if the probabilities of the measurements given either class have normal distributions and equal variance.

2.2.3.3 Ma *et al.* Method

Ma *et al.* [64] described an iris recognition algorithm based in the characterization of key local variations. It is composed of five main stages:

- Iris Localization. The authors approximate both the pupillary and scleric borders as circles. The procedure starts by roughly iris region finding followed by the exact computation of the parameters correspondent to both iris borders, according to a procedure similar to that of Wildes' [120] proposal.

- Iris Normalization. In order to compensate the variations in pupil size and in image capturing distance, authors apply the normalization process to the segmented iris image described by Daugman [18].

- Image Enhancement. Since there is a non-uniform brightness and low contrast of the normalized iris images, the authors perform image enhancement based in the subtraction of the estimated background illumination of small blocks (32×32) of the image. Such processing compensates for the non-uniform illumination.

- Feature Extraction. Considering the characteristics of the iris as a sort of transient signals, authors construct a set of 1-D intensity signals, according to the following equation:

$$S_i = \frac{1}{M}\sum_{j=1}^{M} I_{(i-1)*M+j}, i = 1, \ldots, N \tag{2.21}$$

where I is the normalized image of $K \times L$ and I_x denotes the x^{th} row of the image. M is the total number of rows used to form S_i and N is the total number of 1-D signals. Each signal is a combination of M successive horizontal scan lines of the image, reflecting its local variations along the horizontal direction. Further, authors used the dyadic wavelet decomposition and the *Mallat* as mother-wavelet. Analyzing the local minimums and maximums of the resultant signal at the analyzed scales, the authors observed that each pair of local extremum points corresponds to faint characteristics variations in the original iris image. For each signal S_i, the position of those points at two scales are concatenated to form the corresponding features:

$$f_i = \{d_1, \ldots, d_m, d_{m+1}, \ldots, d_{m+n}, p_1, p_2\} \tag{2.22}$$

where m and n are respectively the number of components from both scales and d_i denote the position of the local variations in the 1-D signal. p_i represents the type of the first extremum point at each scale. Further, the features correspondent to different scales (intensity signals) are concatenated in the feature vector f:

$$f = \{f_1, f_2, \ldots, f_N\} \tag{2.23}$$

where N is the total number of 1-D intensity signals.

- Matching. This stage is accomplished through a two-step approach:

  1. The original feature vector is expanded into binary form. At each position, the components p_i are set to 1 or -1 according to the type of extremum point. Authors set the maximums to 1 in the binary sequence and the minimums to -1, building a binary feature vector given by:

     $$Ef = \{Ef_1, Ef_2, \ldots, Ef_N\} \tag{2.24}$$

     where Ef_i denotes the binary expansion of feature component f_i.

  2. The similarity between two binary sequences is computed through the XOR function, given by:

     $$D = \frac{1}{N} \sum_{i=1}^{N} \frac{1}{2L} \sum j = 1^2 \Big(Ef^1_{(i,j)} \otimes Ef^1_{(i,j)} \Big) \tag{2.25}$$

where Ef^1 and Ef^2 denote two different binary feature vectors, $\otimes$ is the "XOR" operator, L is the length of the binary sequence and N is the total number of 1-D intensity signals.

2.2.4 Non-Cooperative Iris Recognition

In this thesis, we use the *non-cooperative iris recognition* term as the process of automatic recognize individuals using images of their iris captured at a distance and without requiring any active participation. As it is illustrated by figure 2.9, it is, in theory, possible to apply real-time face and eye detection algorithms that provide information about the localization of the subjects' irises and enable its automatic capturing through high resolution imaging systems.

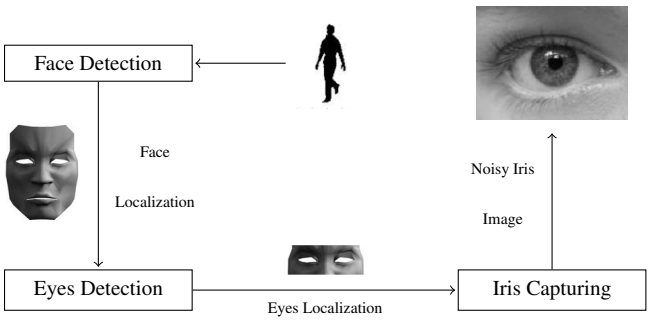

Figure 2.9: Main stages of the non-cooperative iris recognition.

This type of use has motivated increasing interests and was the subject of several recent studies. Following the recognition process proposed by Du *et al.* [29], in [28] the authors investigated the performance of the use of a partial iris part for recognition. They analyzed 3 different kinds of partial iris images: "left-to-right" (left middle part of the iris), "outside-to-inside" and "inside-to-outside" (respectively the outer and inner parts of the iris). In their experiments, the authors observed a distinguishable and unique signal when analyzing the inner parts of the iris and concluded that it is possible to use only portions of the iris for human identification. From our viewpoint, the utilization of the $CASIA$ database constituted a weak point, regarding the desired simulation of non-cooperative environments.

Dorairaj *et al.* [27] described an iris recognition system that deals with off-angle images. They started by the estimation of the gaze direction, through the Hamming distance between the Independent Component Analysis of a frontal view image and the captured one. Further,

they applied a projective transformation that brings the captured iris image to frontal view. This enables the execution of the recognition process as if the captured image were a frontal view. Apart from images of the $CASIA$ database, the authors used others captured in their institute to experimentally confirm their conjectures and achieve high accuracy in the recognition of off-angle images.

In a paper that addresses the challenges on non-cooperative iris recognition, Sung *et al.* [109] roughly identified the potential problems that must be overcome. They considered the problem of lighting conditions as being insurmountable, unless special lighting methods are introduced. The problem of off-angle images, when the gaze of the subjects is not directed to the camera, motivated the proposal of a slightly uncommon segmentation method composed by the initial inner eye corner detection followed by a least square elliptical fit to the limbic edge pixels. In order to identify the information degradation resultant from the non-cooperative image capturing, specially on the acquisition of defocused images, the authors propose a method based on wavelet packet maximum Shannon entropy reconstruction for measuring the image information. The feature extraction was made through the classical convolution with a bank of complex-valued 2D Gabor filters. They concluded that the feature comparison by means of correlation and classification through the nearest neighbor produce better results than Hamming distance and thresholding in less quality images, although they used a small database for the experiments.

Fancourt *et al.* [32] claim the feasibility of human iris recognition at up to 10 meters distance. Through an imaging framework composed by a telescope and a infrared camera, they varied distance, capture angle, environmental lighting, and eyewear and analyzed the recognition accuracy. Based in a local correlation matcher, the authors reported a minor performance degradation with distance, off-angle images and eyewear. However, similarly to [28], their results where obtained when the captured images do not contain significant portions of noise, specifically due to lighting heterogeneity.

The above described proposals claim the possibility to capture images with enough quality in less cooperative modes and achieve accurate human recognition in these situations. This enables the covert biometric recognition, which has considerable privacy concerns. In the following section we briefly discuss some of these concerns.

2.2.4.1 Privacy Concerns

It is accepted that biometrics is a technology that will either great benefit or burden modern societies in a near future. With the increasing number of infrastructures for performing reliable automatic recognition and the ability to associate one identity with a personal behavior or characteristic, concerns are growing over whether this information might be abused and violate individuals' rights to anonymity. It is questioned that the accountable and responsible use of biometric systems can it fact protect the individual privacy, while others argue the prevalence of the privacy issues [88].

Privacy is the ability to lead a life free of intrusions, remaining autonomous and able to control the access to its personal information. The use of biometrics can, specially in the covert mode, lead to circumstances when the user is not aware of the amount of information collected, as well of its uses. The problem is enhanced by the fact that biometrics don't use information about the person, but rather information of the person, intrinsic to each one.

Biometrics create an environment in which organizations have enormous power over individuals [100]. This can be regarded as contrary to the patterns that have been associated with the rise of personal freedoms and free societies. It could be argued that this kind of technology undermines democracy, since it potentiates people to be marginalized.

On the other hand, modern societies have increasing security requirements, motivated essentially by terrorist acts. Biometrics constitute a crucial tool against this type of phenomenons and considerably increase the security levels in a broad range of applications (e.g., air travels, sports events or weapons access).

Schneier [103] observed that biometric traits are unique identifiers but are not secret and, at specific circumstances, are easy to steal (e.g., to get a non-licensed picture of a person's face in order to counterfeit a face recognition system). He concluded about a weakness, concerning privacy. In other perspective, the requiring of automated mechanisms to access a resource leads that system administrators can easily track all accesses to the resource, as well infer information about users' behavior.

Some of the individual biometric traits could be considered undignified to be captured. In addition, some are heavily connected with the forensic sciences and can carry negative connotations because of their prevalent use in such domains (e.g., fingerprint). The hygiene of the biometric sensors might as well be a concern.

Prabhakar *et al.* [88] identified three systematic privacy concerns:

- Unintended functional scope. Because biometric traits are biological in origin, the collectors might glean statistical information about the captured signal and correlate this information with certain type of genetic disorders or other deceases. Such derived medical information could be used to discriminate segments of the population.

- Unintended application scope. The link between different biometric signals of an individual could be used to infer information and accumulate power over individuals and their autonomy.

- Covert recognition. As some of the biometric characteristics are easily visible, it is often possible to obtain a biometric sample without a person's knowledge, enabling the covert recognition of previously enrolled people. In this situation, people who desire to remain anonymous in any particular situation could be denied their right.

In short, we observed the existence of several cultural, social and legal issues for the massive adoption of biometrics. Although the technology has potential to increase the security and reliability of many of the modern societies trivial activities, it is also propitious for privacy privacy abuses, essentially due to the unappropriate use of the captured information.

2.2.4.2 Face Localization Methods

Face detection is the first step for non-cooperative iris recognition. Numerous techniques have been developed to detect faces in images [123]. Given a single image, the goal is to identify all image regions that contain a face, regardless of its three-dimensional position, orientation and lighting conditions.

Based in a cellular neural-network / non-linear algorithm, the authors of [73] propose a system for real-time face detection in uncontrolled environments. In [36], through the use of the multilevel Ising model, a dynamic attention map is built, assigning each Ising spin to *face* or *non-face* and further using the multilevel Ising search to reduce the number of spin candidates and achieve computational efficiency.

2.2.4.3 Eye Detection Methods

Eye detection and tracking in images has been the subject of several proposals. These usually operate in images containing the region correspondent to the subjects' head and can be regarded as the preceding stage to the high definition iris capturing.

The authors of [34] describe an integrated framework to capture images of the human eyes at a distance. It is composed by a video-camera with wide field of view and a high resolution digital still camera with narrow field of view. The video-camera first localizes the human face and provides this information to the digital camera to focus the region corresponding to the subject's eyes.

In [128], an integrated eye tracker for robust eye detection under variable lighting conditions is described. The method starts with a preprocessing stage that minimizes the interference from different illumination sources and further detects the potential eye localizations through the use of support vector machines.

In [35], the authors propose a method to both localize and track human eyes in non-controlled lighting conditions. They combine particle filtering with the Expectation-Maximization algorithm.

2.2.4.4 Types of Noise in the Captured Iris Images

This section is specially relevant in the context of our work. Here we identify and describe the most common noise factors that result of non-cooperative image capturing processes, either at-a-distance, without users' cooperation and within heterogeneous lighting conditions.

Based in observations of the available iris image databases and in our experimental imaging processes, we identified eleven factors that we considered as noise: the iris obstruction by eyelids (NEO) or eyelashes (NLO), specular (NSR) or lighting reflections (NLR), poor focused images (NPF), partial (NPI) or out-of iris images (NOI), off-angle iris (NOA), motion blurred irises (NMB) and pupil (NPS) or sclera (NSS) portions wrongly considered as belonging to the iris.

Iris obstructions by eyelids (NEO) The biological function and natural eyelid movement can obstruct relevant portions of the iris, specially in its vertical extremes (figure 2.10). Commonly, NEO noise regions are one of the largest and appear in the lower regions of the segmented and normalized iris images.

Iris obstructions by eyelashes (NLO) Eyelashes can obstruct portions of the iris in two distinct forms as they appear isolated or grouped. If an eyelash is isolated (upper eyelid of figure 2.11), it appears as a very thin and darker line in the iris region. The existence of multiple eyelashes in the iris regions generates a uniform darker region (near the upper eyelid of figure 2.10).

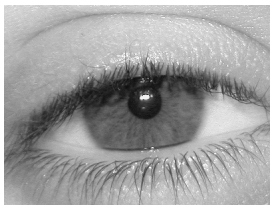

Figure 2.10: Noisy iris image due to eyelids and eyelashes obstructions.

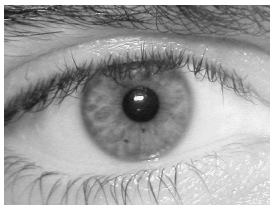

Figure 2.11: Noisy iris image due to isolated eyelashes obstructions.

Lighting reflections (NLR) These type of noise regions usually correspond to reflections from artificial light sources near to the subject, although they can appear in the image capturing within natural lighting environments. These reflections have high heterogeneity, as they can appear with a broad range of dimensions and localized in distinct regions of the iris. These areas have intensity values close to the maximum and are exemplified by the region on the upper and left portion of the iris of figure 2.12.

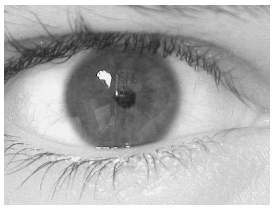

Figure 2.12: Noisy iris image due lighting reflections.

Specular reflections (NSR) This type of reflections corresponds to reflected information from the environment where the user is located or is looking at. As illustrated by the highest intensity region in the upper portion of the iris of figure 2.13, these reflections can obstruct large regions, or even the majority, of the iris. Commonly, they have lower intensity values than the lighting reflections and can correspond to a wide range of objects that the user is surrounded by.

Poor focused images (NPF) Due to the moving elements that interact in the non-cooperative capturing and to the limited depth-of-field of any imaging system, the image focus is

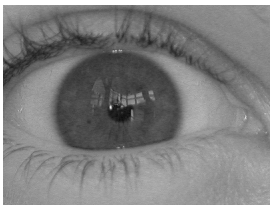

Figure 2.13: Noisy iris image due specular reflections.

one of the biggest concerns. Sometimes, small deviations (centimeters) in the image capturing distance can propitiate the existence of images with severe focus problems, that, almost invariably, lead to the increment of the false rejection rates. A poor focused image is illustrated by figure 2.14.

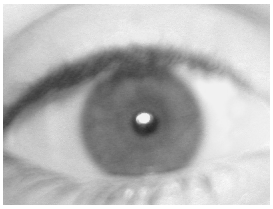

Figure 2.14: Noisy iris image due to poor focus.

Partial captured irises (NPI) The image capturing at a distance and with subjects head and body movements propitiates that the close-up eye images could contain exclusively portions of the iris. Depending of the amount of information missing, this can be obviously a relevant obstacle to biometric recognition, which is illustrated by figure 2.15.

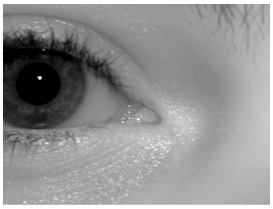

Figure 2.15: Partial captured iris.

Out-of-iris images (NOI) This is an extreme noisy factor and, obviously, obstructs any attempt of biometric recognition. However, it must be considered, in order to avoid false acceptances motivated by the execution of the recognition algorithms based in non-iris areas. An example of a capture without any portion of the iris visible is shown in figure 2.16.

Figure 2.16: Out-of-iris image.

Off-angle iris (NOA) Due to rotation of the subjects head and eyes, it is possible to capture iris images with the iris not aligned with the imaging direction, as exemplified by figure 2.17. These off-angle images have elliptical shape for the region corresponding to the iris. They demand the use of projection techniques, in order to deal with the iris data as if it was not off-angle.

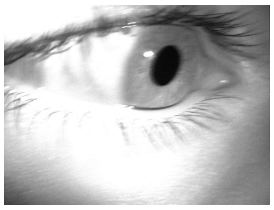

Figure 2.17: Off-angle iris image.

Motion blurred images (NMB) Once again due to several moving parts that interact in the iris image capturing, the iris image can be blurred by motion. Since it is the most frequent and quickest type of interacting movement, we observed that the eyelids movement has an significant contribute to this type of noise, as illustrated by figure 2.18.

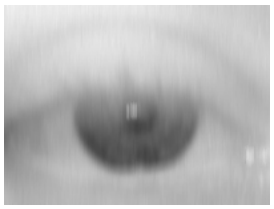

Figure 2.18: Motion blurred iris image.

Pupil wrongly considered as belonging to the iris (NPS) When the segmentation of the pupillary iris border is not accurate, some portions of the iris will be wrongly considered as belonging to the iris. Those areas appear at the upper part of the normalized

and segmented iris image and have usually lower intensity values than those that correspond to the iris, as exemplified by figure 4.8.

Sclera wrongly considered as belonging to the iris (NSS) Similarly to the above described type of noise, when the segmentation of the scleric iris border is not accurate, portions of the sclera are wrongly considered as belonging to the iris and appear in the lower part of the segmented and normalized iris images.

The analysis of the above described noise factors allowed us to divide them into two major classes: local and global. The first correspond to noise that corrupts localized regions of the image, whereas the remaining regions remain noise-free and possibly enable the execution of the recognition task. As described in the following chapters, the detection, localization and robust handling of local noise factors can significantly improve the robustness of iris recognition and represent an achievement towards non-cooperative recognition. Oppositely, the global noise factors affect the image as a whole and, depending of its intensity, can constitute a definitive obstacle to the recognition process.

2.3 Summary

This chapter introduced the main biometric concepts. First, a definition was given , based on the synthesis of several others. We compared the two main modes of biometrics functioning and presented a possible classification and respective comparison between the most common biometric traits, according to six different perspectives.

After having briefly justified the choice for the use of iris for the purposes of our work, we focused in the anatomy of the human eye, with obvious emphasis to the iris. Later we overview the main stages of typical iris recognition and presented some of the most common methods for each of these stages.

Finally, in the non-cooperative recognition compass, we described some of the privacy concerns and focused on the description of the noise factors that result of the non-cooperative image capturing.

Chapter 3

Iris Image Databases

In this chapter we describe the main characteristics of the public and freely available iris image databases for biometrics purposes. Through examples, we illustrate the types of noise that images from each database contain. Based on the analysis of these noise factors, we present the main motivations that led us to the construction of $UBIRIS$ database and highlight the main distinguishable factors in the comparison with the remaining ones. Further, we detail the optical framework used in both image capturing sessions of the $UBIRIS$ database and briefly present some statistics about its images.

3.1 Public and Free Databases

The biometrics research and development demands the analysis of human data. Obviously, it is unrealistic to perform the test of algorithms in data captured on-the-fly, due to the enormous uneasiness that this would imply. Moreover, the fair comparison between recognition methods demands similar input data to valorize and contextualize their results. Therefore, when it comes to the test of recognition methods, standard biometric databases assume high relevance and become indispensable to the development process.

Regarding the iris biometrics compass, there are presently, apart from the $UBIRIS$, five public and freely available iris image databases. In the following subsections we describe the main characteristics of their images and turn our attention to the analysis of the noise factors - defined in section 2.2.4.4 - that each database contains. We considered the analysis of these noise factors and the images heterogeneity as the most important parameters, concerning the terms and purposes of our work. Through illustration, we exemplify some

of the most common types of noise that each database contains.

3.1.1 BATH Database

The University of Bath ($BATH$) iris image database is constantly growing and at present contains over 16000 iris images taken from 800 eyes of 400 subjects. It results of a project which aims to build an "high quality iris image resource" [114]. The majority of the database comprises images taken from students and staff of the University of Bath [1].

The images are of very high quality, taken with a professional machine vision camera, mounted on a height-adjustable camera-stand. The illumination was provided through an array of infrared LEDs, positioned below the camera and set at an angle such that reflections were restricted to the pupil. Further, an infrared pass filter was used in order to cut out the daylight and other environmental light reflections on the irises region.

The above described framework increased the images quality, while turned it less appropriate for the terms of our work. Images from the BATH database contain almost exclusively noise factors related with iris obstructions (due to eyelids and eyelashes), as exemplified by figure 3.1. Furthermore, the main characteristics of its images are quite homogeneous, clearly resultant from a cooperative imaging setting.

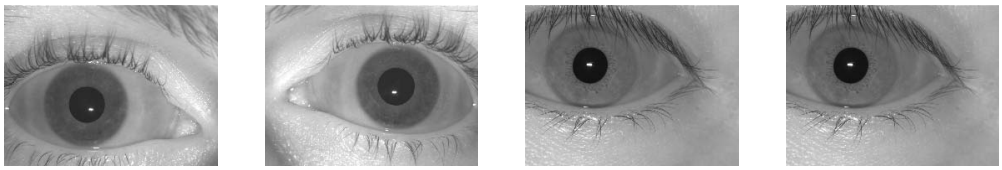

Figure 3.1: Examples of iris images from the $BATH$ database.

3.1.2 CASIA Database

Iris recognition has been an active research topic of the Institute of Automation from the Chinese Academy of Sciences [2]. Having concluded about a lack of iris data for algorithm testing, they developed the $CASIA$ image database. Apart from being the oldest, this database is clearly the most known and widely used by the majority of the researchers.

[1] http://www.bath.ac.uk/

[2] http://www.cas.cn/

$CASIA$ iris image database [44] (version 1.0, the only one that we had access to) includes 756 iris images from 108 eyes, hence 108 classes. For each eye, 7 images are captured in two sessions, where three samples are collected in the first and four in the second session. Similarly to the above described database, its images were captured within an highly constrained capturing environment, which conditioned the characteristics of the resultant images. They present very close and homogeneous characteristics and their noise factors are exclusively related with iris obstructions by eyelids and eyelashes. Moreover, the postprocess of the images filled the pupil regions with black pixels, which some authors used to facilitate the segmentation task. From our viewpoint, this significantly decreased the utility of the database in the evaluation of robust iris recognition methods.

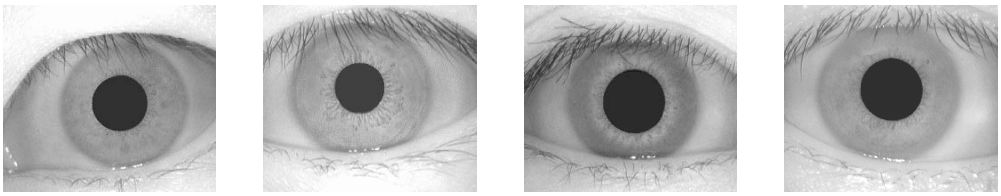

Figure 3.2: Examples of iris images from the $CASIA$ database.

3.1.3 ICE Database

The Iris Challenge Evaluation (ICE) is a contest designed to measure the accuracy of the underlying technology that makes iris recognition possible. Its goals are to promote the development and advancement of iris recognition and assess the technology's current level of performance. It is divided into two stages: first, it was asked to researchers and developers to participate in "iris recognition challenge problems" that might improve their recognition algorithms. Later, an opportunity to participate in a large-scale and independent evaluation will be given, through a new iris data set and a proper evaluation framework.

Regarding the first stage of ICE, to facilitate the evaluation of different iris recognition proposals, an iris image database has been released for the researchers and entities that manifest the desire to participate in this competition.

The ICE [82] database is comprised of 2954 images, with a variable number of images per subject. Similarly to the remaining public iris databases, its images were captured having quality as the main concern and clearly simulate the users' cooperation in the image capturing. Therefore, the noise factors that the ICE database contains are almost exclu-

sively related with iris obstructions and poor focused images. Interestingly, there are some images that were deliberately rotated, as exemplified by figure 3.3. Also, some iris were partially captured.

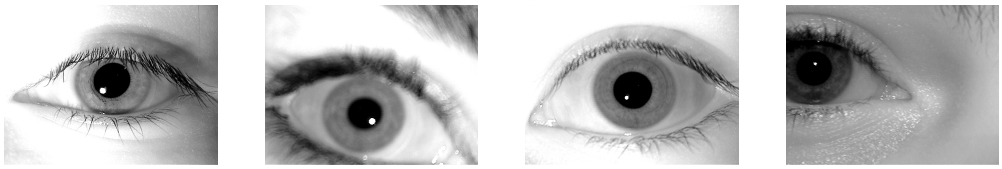

Figure 3.3: Examples of iris images from the ICE database.

3.1.4 MMU Database

The Multimedia University[3] has developed a small data set of 450 iris images (MMU) [75]. They were captured through one of the most common iris recognition cameras presently functioning (*LG IrisAccess®2200*). This is a semi-automated camera that operates at the range of 7-25 cm. Further, a new data set ($MMU2$) comprised of 995 iris images has been released and another common iris recognition camera (*Panasonic BM-ET100US Authenticam*) was used. The iris images are from 100 volunteers with different ages and nationalities. They come from Asia, Middle East, Africa and Europe and each of them contributed with five iris images from each eye. Obviously, the images are highly homogeneous and their noise factors are exclusively related with small iris obstructions by eyelids and eyelashes.

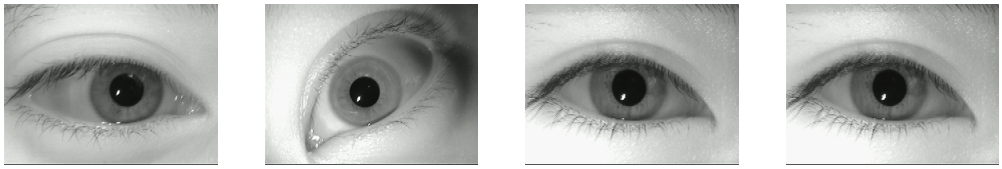

Figure 3.4: Examples of iris images from the MMU database.

[3] http://www.mmu.edu.my

3.1.5 UPOL Database

The $UPOL$ [26] iris image database was built within the University of Palackého and Olomouc [4]. Its images have the singularity of being captured through an optometric framework (*TOPCON TRC50IA*) and, due to this, are of extremely high quality and suitable for the evaluation of iris recognition in completely noise-free environments.

The database contains 384 images extracted from both eyes of 64 subjects (three images per eye). As can be seen in figure 3.5, its images have maximum homogeneity and inclusively the iris segmentation is facilitated by the dark circle that surrounds the region corresponding to the iris. Obviously, these characteristics make this database the less appropriate for the non-cooperative iris recognition research.

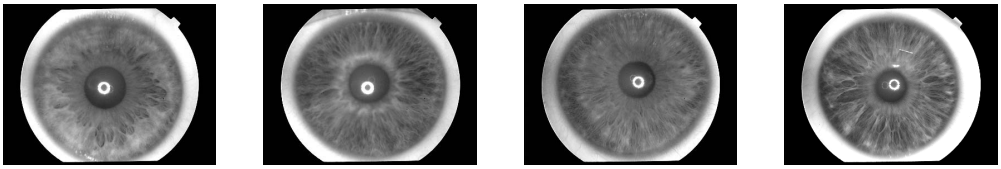

Figure 3.5: Examples of iris images from the $UPOL$ database.

3.1.6 WVU Database

The West Virginia University [5] developed an iris image database (WVU) [101] comprised of 1852 images from 380 different eyes. The number of acquisitions from each eye ranges between three and six and an OKI IrisPass-H hand-held device was used. Images of the WVU database were captured with less constraining imaging conditions and, due to this, incorporate several types of noise, such as iris obstructions, poor focused and off-angle iris images. However, there are few iris images with significant regions affected by specular and lighting reflections, which we believe to be the most common type of noise resultant of natural light imaging environments. We stress that this was one of the major motivations that led us to decide about the need of a new and noisier iris image database, that later originated the $UBIRIS$ database.

[4] http://www.upol.cz

[5] http://www.wvu.edu

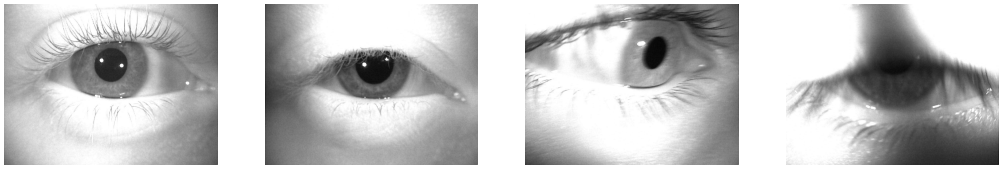

Figure 3.6: Examples of iris images from the WVU database.

3.2 UBIRIS Database

After studying the above described iris databases, we concluded that none of them was suitable for the evaluation of robust iris recognition methods, those where noise identification and handling assumes higher relevance. Apart from the WVU database, that contains some noise factors but significantly lacks iris specular and lighting reflections, all the remaining databases were constructed within cooperative environments. This makes them more suitable for the preliminary evaluation of iris segmentation, feature extraction or comparison strategies, when the noise factors constitute an a priori obstacle to conclude about their merits.

Based on this, we decided to build a new public and freely available iris images database - $UBIRIS$ [89] - with a fundamental characteristic that distinguished it from the remaining ones: it is a "noisy iris image database" and the noise factors are not only avoided but rather induced, in order to simulate the non-cooperative image capturing.

UBIRIS database is comprised of 1877 images collected from 241 subjects within the University of Beira Interior [6] in two distinct sessions and constituted, at its release date, the world's largest public and free iris database for biometric purposes.

3.2.1 Image Capturing

We used a Nikon E5700 camera with software version E5700v1.0, 71mm focal length, 4.2 F-Number, 1/30 sec. exposure time, RGB color representation and ISO-200 ISO speed. Images dimensions were 2560×1704 pixels (width $\times$ height) with 300 dpi horizontal and vertical resolution and 24 bit depth. They were saved in TIFF format. For the first image capture session, where the enrollment was simulated, we tried to minimize all possible noise factors, specially those related with reflections, obstructions, focus, motion, luminosity and

[6] http://www.ubi.pt

contrast. The used image capturing framework is given in figure 3.7a and was installed inside a dark room.

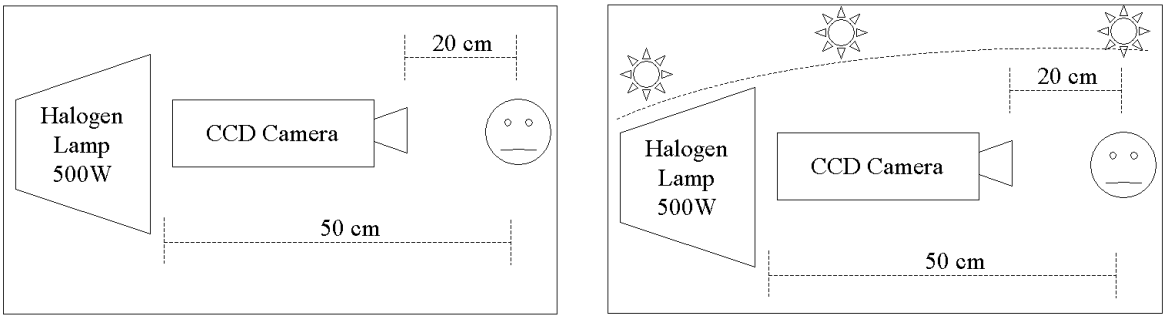

(a) *Image capturing framework of the first session.*

(b) *Image capturing framework of the second session.*

Figure 3.7: Image capturing frameworks of the two sessions of the $UBIRIS$ database.

Further, two weeks later, we make the second session and changed the location and setup of the image capturing framework, as given in figure 3.7b. The introduction of natural luminosity significantly increased the dynamics of the imaging conditions and enabled the appearance of highly heterogeneous images regarding iris reflections and obstructions, poor focused, and with highly heterogeneous characteristics (e.g. in terms of contrast or brightness). At this stage, our aim was to simulate the image capturing without or with minimal subjects' cooperation.

Figure 3.8 illustrates some of the noise factors that images of the $UBIRIS$ database contain. Within non-cooperative image capturing environments, it is highly expectable to capture poor focused images (figure 3.8b), iris obstructed by eyelids and eyelashes (figures 3.8c and 3.8d), specular (figure 3.8f) and lighting (figure 3.8e) reflections in the iris regions, motion blurred images (figure 3.8h) or even images without any visible portion of the iris (figure 3.8g).

3.2.2 Preprocessing

In the setup of the optic devices used in the capturing of $UBIRIS$ images, we maximized the amount of collectable information, saving images in the TIFF format with average size of 15 MBytes. Therefore, due to constraints in the information diffusion over internet, preprocessing became a requirement. We made three different versions of the database: 800×600 pixels (width $\times$ height) with 24 bit color images and 200×150 pixels (width

(a) *Good quality iris image.*

(b) *Poor focused iris image.*

(c) *Iris with eyelids and eyelashes obstruction.*

(d) *Iris with extreme eyelids obstruction.*

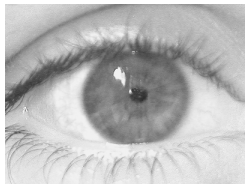

(e) *Iris with lighting reflections correspondent to light sources (natural light) next to the user.*

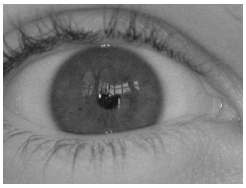

(f) *Iris with specular reflections correspondent to information of the environment that surrounds the user.*

(g) *Out-of-iris image.*

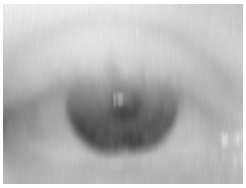

(h) *Motion blurred iris.*

Figure 3.8: Examples of images from the $UBIRIS$ database.

$\times$ height) with 24 bit color and grayscale images. This process allowed us to compress the $UBIRIS$ data respectively to 436, 96 and 65 MBytes, and made acceptable its diffusion over internet.

3.2.3 Image Classification

Figure 3.9 contains two histograms with the gender (figure 3.9b) and age (figure 3.9a) of the people from where the images were collected. The fact of the capturing sessions were made inside the computer science department of University of Beira Interior explains the majority of young males (below 30 years).

All the images from both sessions were manually classified with respect to three parameters (‘Focus’, ‘Reflections’ and ‘Visible Iris’) in a three values scale (‘Good’, ‘Average’ and ‘Bad’). This classification is given in table 3.1 and confirms without doubt the variability of the images quality according to the capturing session.

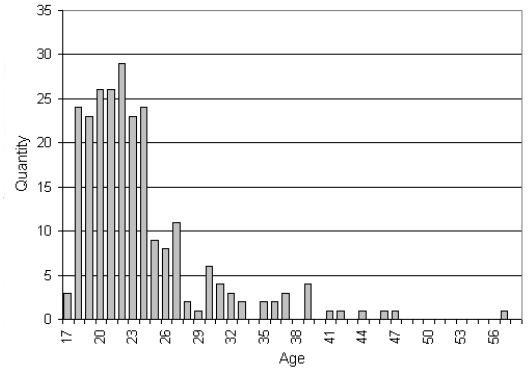

(a) Histogram of the age of the $UBIRIS$ participants.

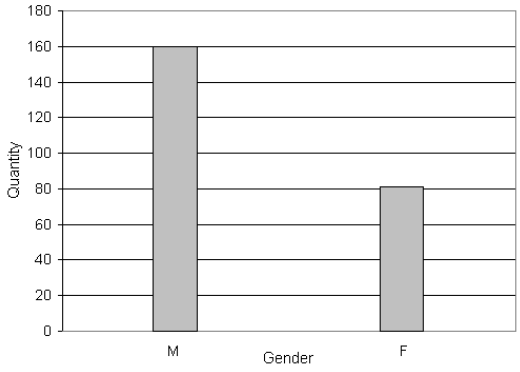

(b) Histogram of the gender of the $UBIRIS$ participants.

Figure 3.9: Age and gender histograms of the volunteers that participated in the construction of $UBIRIS$ database.

Parameter	Good, %	Average, %	Bad, %
First Session			
Focus	76.10	16.51	7.39
Reflections	78.52	19.09	1.99
Visible Iris	43.65	52.86	3.49
Second Session			
Focus	69.70	19.39	10.91
Reflections	22.27	69.09	8.64
Visible Iris	24.09	38.64	37.27

Table 3.1: Classification of $UBIRIS$ images quality, regarding focus, reflections and proportion of visible iris, according to the image capturing session.

3.2.4 Web Site

After the capturing, preprocessing and classification of $UBIRIS$ images, we built a web site[7] to enable the worldwide data diffusion. For each above described version of the database, we compacted the data inside a password protected file. Any person who desires a copy of the database has to email one of the authors ({hugomcp,lfbaa}@di.ubi.pt) with "UBIRIS password" as subject of the message and with the body containing the name, institution and country of the user. Thus, we had feedback about the acceptability of this database by the academic and research institutions.

[7] http://iris.di.ubi.pt

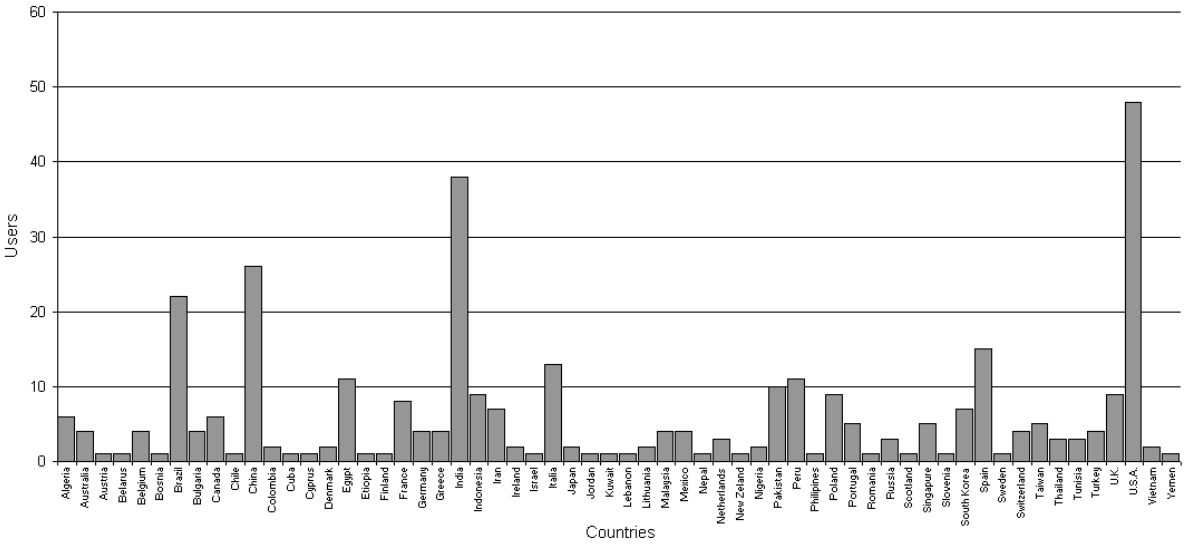

Figure 3.10: Histogram of the countries from where the users of UBIRIS database were registered (5^{th} August, 2006).

As figure 3.10 illustrates, at August 2006, 340 users from 60 countries, essentially integrated within universities, forensic schools and research laboratories, required the access to the $UBIRIS$ database. Moreover, at this date we had knowledge of at least one MSc. thesis and one BEng. final project whose experiments were exclusively made with $UBIRIS$ images, essentially due to the reasons that motivated its construction: the research and development of robust iris recognition methods able to deal with noisy and highly heterogeneous iris images. Obviously, this can be considered an achievement.

3.3 Analysis of Databases' Noise Factors

3.3.1 Types of Noise

In order to provide an overview of the main characteristics of each iris image database, table 3.2 summarizes the noise factors that images from the above described databases contain. Each column identifies a noise factor, which meaning is described in section 2.2.4.4. "X" denotes that the database contains images with the correspondent noise factor and "-" denotes the opposite.

The analysis of this table allowed us to conclude that the noisiest database is the $UBIRIS$ database, which confirms our purposes' success. In fact, apart from not containing off-angle

iris images, all the remaining noise factors that are expectable in the non-cooperative capturing setting are present in images of the $UBIRIS$ database. Oppositely, all the remaining databases contain less number of noisy images and its images have more homogeneous characteristics.

Iris Database	NEO	NLO	NLR	NMB	NOA	NOI	NPF	NPI	NSR
BATH	X	X	-	-	X	-	-	-	-
CASIA	X	X	-	-	-	-	-	-	-
ICE	X	X	-	-	-	-	X	X	-
MMU	X	X	-	-	-	-	-	-	-
UPOL	-	-	-	-	-	-	-	-	-
UBIRIS	X	X	X	X	-	X	X	X	X
WVU	X	X	-	X	X	-	X	X	-

Table 3.2: Overview of the noise factors that public and free iris image databases contain.

3.3.2 Noise Measurements

After the identification of the types of noise that each available database contains, it constituted our goal to have an objective measure about the average quantity of noisy pixels per iris image on each database. In the following experiments, we considered as *noise* those pixels inside the segmented iris region that correspond to any other type of information, as described in section 2.2.4.4.

Iris Database	Image Size, pix.	Iris Radius, pix.	Pupil radius, pix	Noise, %
BATH	1280×960	232	101	6.29
CASIA	320×280	102	37	12.72
ICE	640×480	119	54	6.70
MMU	320×240	57	21	7.83
UPOL	768×576	286	74	1.03
UBIRIS	800×600	206	45	27.62
WVU	800×600	204	54	16.10

Table 3.3: Average quantity of noise pixels within the iris regions of the public and free iris image databases.

We randomly selected 100 images from each of the above described iris databases, hoping that they were representative of the respective database images. Further we manually classified each iris pixel as *noisy* or *noise-free* and obtained a binary map correspondent to the noisy iris regions. The relation between the noisy and noise-free data is given in table 3.3. The first column identifies the database, the second gives the dimensions of the images (width $\times$ height), the third and forth contain the average radius of the iris and pupil radius. All of these values are expressed in pixels. Finally, the column *noise* identifies the proportion between the number of noise pixels and the number of pixels belonging to the iris region. This value is expressed in percentage.

3.3.3 Conclusion

As expected, through the analysis of both tables 3.2 and 3.3, we obtained a more objective idea about the degree and type of noise characteristics of each image database. We concluded that the majority of these databases were build having the images' quality as main concern, inducing its use in the cooperative setting. Apart from $UBIRIS$, WVU iris image database is the one that contains a relatively larger number of noisy pixels within the captured iris regions. However, as stated before, the lack of pixels corrupted by reflections (specular and lighting) is from our viewpoint regarded as a weak point, and made $UBIRIS$ the main database for our experiments.

3.4 Summary

In this chapter we identified, through description and illustration, the types of noise that the public and free iris image databases for biometrics purposes contain. Furthermore, we justified the requirements for the construction of a new public and free iris database image - $UBIRIS$ - that simulates the non-cooperative image capturing. We described the noise factors that its images contain and distinguish the database from the remaining ones. We stress that $UBIRIS$ database has been well accepted by researchers of the academic and commercial domains, having at August, 2006 more than 340 registered users originated from 60 different countries.

Chapter 4

Iris Segmentation

This chapter concerns to the iris segmentation stage, which, as in any other image processing task, plays a crucial role in the overall recognition success. Moreover, the noise regions resultant of the non-cooperative image capturing increase the demands of segmentation robustness and adaptability. After describing the most common iris segmentation proposals, in section 4.3.4 we show that their accuracy significantly decreases when dealing with noisy iris images, such as those of the $UBIRIS$ database. To overcome of this lack of robustness was the main motivation behind our iris segmentation proposal, which is based on feature extraction and clustering stages that produce an intermediate image, more homogeneous than the captured one. Later, in section 4.4 we analyze the influence that small segmentation inaccuracies have in the recognition accuracy. We experimentally found that small errors in the segmentation of the pupillary border have strong impact in the error rates and describe a method that is able to identify this type of inaccuracies.

4.1 Image and Iris Segmentation

Image segmentation can be defined as the *partitioning of an image into several components*. It is an important stage of any automated image processing system, essentially because it is the basis for any further operations, such as description or recognition. In the pattern recognition domain, segmentation is the assignment of each pixel to an image region, which can be regarded as a typical classification problem.

Regarding the iris biometrics compass, the segmentation stage receives a close-up eye image and localizes the pupillary and scleric iris borders in the image. We stress the

assumption about the existence of image capturing frameworks, supported by face and eye detection algorithms, which must be able to capture images similar to the illustrated by figure 4.1. This is an image of the $UBIRIS$ database that contains the eye's region and represents those that typically are processed by the segmentation algorithm.

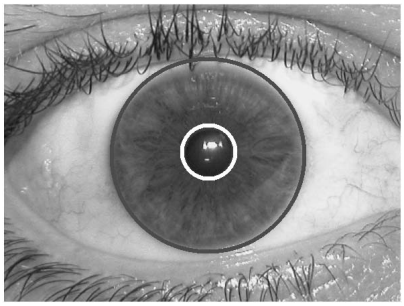

Figure 4.1: Segmented iris image with the inner (pupillary) and outer (scleric) borders respectively signalled by the brighter and darker circles.

Segmentation is usually accepted as one of the most challenging stages of iris recognition and the one where robustness plays a more important role. Apart from the iris small dimensions, the natural eye and human body movements increase the segmentation's difficulty. The non-cooperative image capturing setting makes it more probable that the captured irises contain several other types of information (section 2.2.4.4) that increase the segmentation complexity. In the following section we overview the typical iris segmentation methods and detail four of these, that we believe to represent the majority of the proposals. These proposals were later tested against noisy iris images, in order to show their small robustness.

4.2 Most Common Iris Segmentation Methods

The analysis of the iris segmentation literature allowed us to identify two major strategies to perform the iris segmentation: use a rigid or deformable iris template or use its boundary. In most cases, the boundary approach is very similar to that of Wildes [120]: it begins by the construction of an edge-map followed by the application of some geometric form fitting algorithm. The template-based strategies are in general more specific, although sharing the maximization of some equation that identifies the iris borders. Here, we emphasize four of these methods: the classical boundary-based Wildes' approach and three of the template-based approaches (Daugman [18], Camus and Wildes [11] and Martin-Roche *et al.* [70]). These were chosen due to their relevance in the literature, the presented results and by our

belief that they are representative of the majority of iris segmentation proposals, which were summarized in section 2.2.2.1.

4.2.1 Daugman's Method

This is by far the most cited method [18] in the iris recognition literature. It is licensed to *Iridian Technologies*[1] who turned it into the basis of 99.5% of the commercial iris recognition systems. It was proposed in 1993 and was the first method effectively implemented in a working biometric system. The author assumes both pupil and iris with circular form and applies the following integro-differential operator:

$$max_{r,x_0,y_0} \left| G_\sigma(r) * \frac{\delta}{\delta r} \oint_{r,x_0,y_0} \frac{I(x,y)}{2\pi r} ds \right| \tag{4.1}$$

This operator searches over the image domain (x, y) for the maximum in the blurred (by a Gaussian Kernel $G_\sigma(r)$) partial derivative with respect to increasing radius r, of the normalized contour integral of $I(x, y)$ along a circular arc ds of radius r and center coordinates (x_0, y_0). In another words, this method searches in the $\mathbb{N}^3$ *space* for the circumference center and radius with highest derivative values comparing to circumferences of neighbor radius. As showed in section 4.3.4.2, this process proved to be very effective on images with enough separability between iris, pupil and sclera intensity values.

However, we observed that it frequently fails when the images do not have sufficient intensity separability, specially between the iris and the sclera regions. We implemented two preprocess operations with the purpose of image contrast enhancement, hoping that they could contribute to the improvement of the results:

- Histogram Equalization. This operation improves the contrast between each eye's region, which potentially will facilitate the segmentation task. It is described in section 4.3.3.3.

- Binarization. The image binarization - based on a threshold - is a very common operation that maximizes the separability between the iris regions and the remaining ones. This process has, however, one major disadvantage: it is highly dependent of the chosen threshold, and as image characteristics change, the results may seriously deteriorate. Moreover, the binarization compromises one of the Daugman's method

[1] http://www.iridiantech.com

biggest advantages: the non-requirement of user-defined parameters for the achievement of segmentation.

4.2.2 Camus and Wildes' Method

These authors described an algorithm [11] for finding the subjects' iris in close-up images. Similarly to Daugman's method, their algorithm searches in the $\mathbb{N}^3$ space for the three circumference parameters (center (x, y) and radius r) that maximize the following function:

$$C = \sum_{\theta=1}^{n} \Big((n-1)||g_{\theta,r}|| - \sum_{\phi=\theta+1}^{n} (||g_{\theta,r} - g_{\phi,r}||) - \frac{I_{\theta,r}}{n} \Big) \tag{4.2}$$

where n is the total number of directions and $I_{\theta,r}$ and $g_{\theta,r}$ are, respectively, the image intensity and derivatives with respect to the radius in the polar coordinate system. As shown in section 4.3.4.2, this method is highly accurate with images whose pupil and iris intensities are well separated from the sclera ones and with images that contain no significant noise regions, such as reflections. Otherwise, when dealing with noisy data, the algorithm's accuracy significantly deteriorates.

4.2.3 Roche and Avilla's method

According to the template-based strategy, this method [70] operates similarly to Daugman's. It receives a grayscale image, applies the histogram stretch and maximizes the average intensity differences of five circumferences with consecutive radius values:

$$D = \sum_{m} \Big(\sum_{k=1}^{5} (I_{n,m} - I_{n-k,m}) \Big) \tag{4.3}$$

where $I_{i,j} = I(x_0 + i\Delta_r cos(j\Delta_\Theta), y_0 + i\Delta_r sin(j\Delta_\Theta))$. Δ_r and Δ_Θ are the increments of radius and angle and $I(x, y)$ is the image intensity.

In practice, this method searches in the $\mathbb{N}^3$ space for three circumference parameters (center (x, y) and radius r) where the difference between the average intensity of five successive circumferences is maximal.

4.2.4 ' Method

Proposed in 1997, this method [120] performs its contour fitting in two steps. First, the image intensity information is converted into a binary edge-map. Second, the edge points vote to instantiate particular contour parameter values.

The edge-map is constructed through the gradient-based Canny edge detector. In order to incorporate directional tuning, the image intensity derivatives are weighted to favor ranges of orientation. For example, in the localization of the scleric iris border, the image derivatives are weighted to be selective for vertical edges, due to common obstructions in the iris upper and lower extremes, which are the ones with highest horizontal derivatives. Further, the form fitting is made through the well known circular Hough transform, where each edge point votes for particular contour parameter values.

This is clearly the most common method in the iris segmentation literature, having as main disadvantage its dependence of thresholds in the edge-map construction. This constitutes one weak point regarding robustness, required by the non-cooperative image capturing setting. In the experiments we observed that the used edge detector algorithm and their required parameters are critical factors for accuracy. As possible optimizations, we tested two distinct edge detectors: Shen and Castan [104] and Zero-Crossing [69]. The obtained results are described in section 4.3.4.2.

4.3 Proposed Iris Segmentation Method

As above described, common iris segmentation methods either apply an edge detector operator to construct the edge-map or analyze some derivatives of the image intensities, usually with respect to the radius of consecutive circumferences. Both situations are highly sensitive to the specific characteristics of each image, its brightness and contrast, as well as of the existence of noisy iris regions. This high sensitivity was the main motivation behind our purpose of develop of a more robust iris segmentation method.

First, the extraction of information less susceptible to such noise regions and heterogeneous images characteristics is a requirement. The extracted feature set should contain enough information to discriminate between the pixels belonging to the iris and the remaining ones, maintaining small sensitivity to noise.

Moment functions are widely used in various realms of computer vision and image processing. Numerous algorithms and techniques have been developed using image mo-

ments in the pattern recognition area. Tuceryan [113] found that the image moments could capture important textural properties. In addition, we observed that some of the tested images were very similar in terms of the texture to those that we have to deal with. For these reasons, we started by the experimental evaluation of this method on images of the $UBIRIS$ database and later used it as basis for the development of a more robust iris image segmentation method.

4.3.1 Tuceryan's Segmentation

Tuceryan proposed a moment-based texture segmentation algorithm [113], using the moments computed in small image windows as texture features, and further applyed a clustering algorithm to segment the image. The second order regular geometric moments for each image pixel are defined as:

$$M_{pq} = \sum_{-W/2}^{W/2} (\sum_{-W/2}^{W/2} (I(m,n) x_m^p y_n^q)) \tag{4.4}$$

where M_{pq} is the regular geometric moment of order pq, $I(m,n)$ is the pixel image intensity, x, y and W are respectively the neighborhood window coordinates and width.

After finding that these regular moments do not have sufficient discriminant capacity, the author proposed the application of the hyperbolic tangent as nonlinear transducer, followed by an averaging step:

$$F_{pq}(i,j) = \frac{1}{L^2} \sum_{(a,b) \in W_{ij}} (tanh(\sigma(M_{pq}(a,b) - \bar{M})) \tag{4.5}$$

where F_{pq} is the feature image of the M_{pq} moments with mean $\bar{M}$ and W_{ij} is an $W \times W$ average window centered at location (i,j). σ is a parameter that controls the shape of the logistic function and was determined, by trial and error, as 0.01 for most cases.

The classification stage was accomplished through the well known clustering k-means algorithm, producing as output the n-clusters labeled image.

4.3.2 Our Method

The proposed segmentation algorithm is given in the block diagram of figure 4.2. Its rationale consists in make the edge-map less susceptible to the specific image characteristics. We

achieve this by producing a normalized (clustered) intermediate image, that is later used by the edge detector. As this image is more homogeneous and has smaller number of intensities than the original, it facilitates the tuning of the required edge detector parameters, allowing the construction of more accurate edge-maps. Obviously, this facilitates the task of the form fitting algorithm and potentiates the accuracy of the segmentation task.

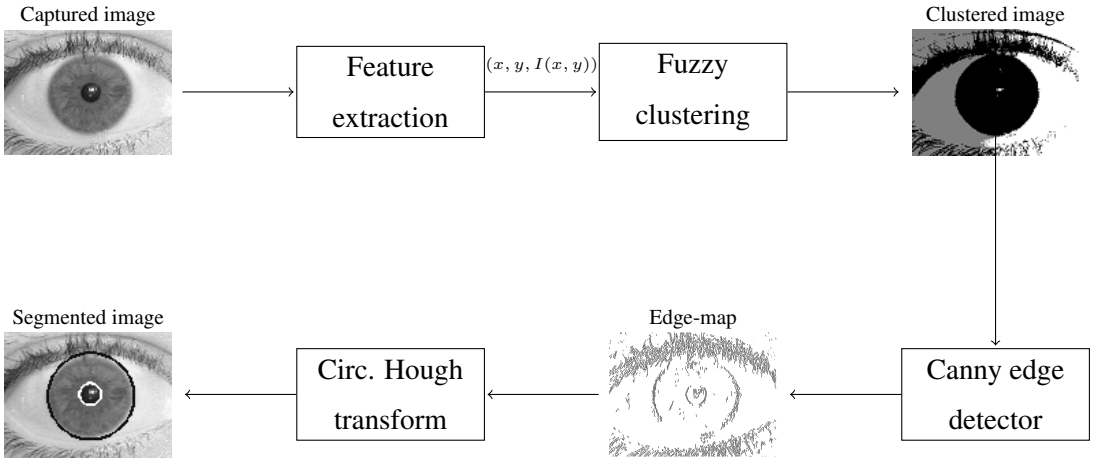

Figure 4.2: Block diagram of the proposed iris segmentation method.

The process begins by the image feature extraction, where three discrete values (column, row and intensity) are extracted from each pixel. Further, the clustering algorithm labels (classifies) each pixel, producing the intermediate image. This image is used by the edge detector to produce edge-maps less susceptible to noise image factors. More accurate edge-maps propitiate higher accuracy of the circular Hough transform and, as the experiments described in section 4.3.4 report, significantly improves the robustness of the segmentation process, even on highly heterogeneous images and with large noisy iris regions.

4.3.2.1 Feature Extraction

We performed several tests (figure 4.3) to select the best feature set by evaluating the capacity of simultaneously localize the iris regions and minimize the noise, related essentially with obstructions (due to eyelids and eyelashes) and reflections (specular and lighting).

We concluded that three discrete components $\{x, y, I(x, y)\}$, where (x, y) are the coordinates of the pixel position and $I(x, y)$ the correspondent pixel intensity, can characterize each pixel and propitiate a correct segmentation. This feature set, hereinafter named "Pixel

position + intensity", preserves information about the spacial relations in the image (pixel position), as well as about the individual properties of each pixel (intensity).

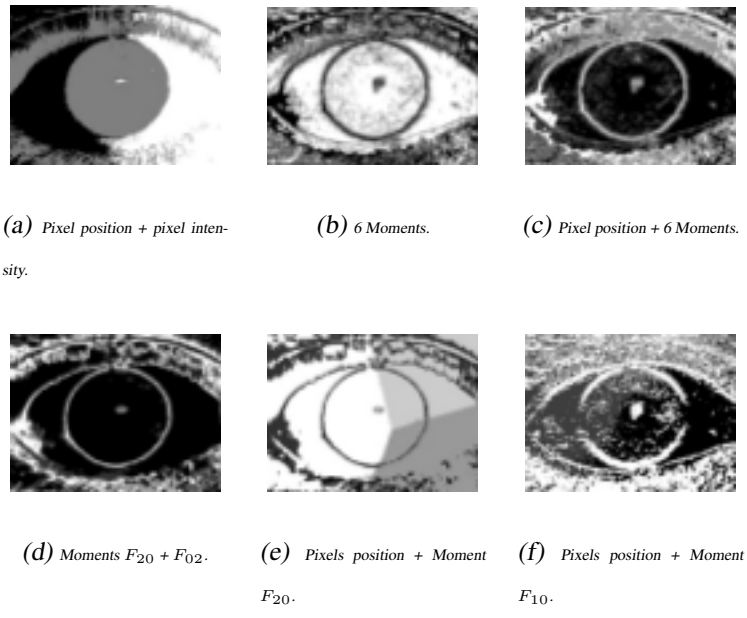

(a) Pixel position + pixel intensity. (b) 6 Moments. (c) Pixel position + 6 Moments.

(d) Moments F_{20} + F_{02}. (e) Pixels position + Moment F_{20}. (f) Pixels position + Moment F_{10}.

Figure 4.3: Clustered images produced using different feature sets.

The moments F_{20} and F_{02} proved to correctly identify the iris borders but also tend to produce considerable noise in the eyelid regions. We found that this can be a relevant obstacle to the posterior circumference fitting stage.

4.3.2.2 Clustering Algorithm

Regarding the clustering (classification) algorithm, the most important thing is its capacity to discriminate, based on the available information, between the pixels that belong to the iris and the remaining ones. With this purpose in mind, we evaluated the following four unsupervised clustering and classification algorithms:

Kohonen's Self Organizing Maps Also called topological ordered maps, the goal in this algorithm is to represent all points in the source space by points in the target space, such that distance and proximity relationships are preserved as much as possible. The task is this: having an input space ϕ and a sequence of input points, to create a mapping from ϕ to the target space y such that points neighboring in the source space are mapped to points that are neighboring in y. The map is usually learned by a feed

forward neural network, where each cell represents a point in the target space. When a pattern from ϕ is presented, each cell in the target space computes its net activation and one of them is activated. Further, all weights from this cell and its neighbors are adjusted regarding the input pattern.

K-Means With a predefined number of k clusters and n data points, each one with dimension d, the algorithm begins by randomly initializing each coordinate of the k clusters. The distance between data points and clusters is computed and one cluster is activated for each input point. The weights of the clusters are adjusted regarding the inputs, so that, at the end of each iteration, the distance between data points and clusters is minimal. This process iterates until the cluster weights are not adjusted or have minimal adjustments. At this point, the k clusters are returned as the algorithm output.

Fuzzy K-Means In every iteration of the classical k-means procedure, each data point is assumed to belong exactly and completely to one cluster. Relaxing this condition, we can think that each sample has a fuzzy membership to each of the k clusters. These memberships are equivalent to the probabilities $\hat{P}(w_i|x_j, \hat{\theta})$, where $\hat{\theta}$ is the parameter vector for the membership functions, x_j is the input vector and w_i are the cluster weights. The fuzzy k-means clustering algorithm seeks a minimum of a heuristic global cost function J_{fuz} [5]:

$$J_{fuz} = \sum_{i=1}^{c} \Big(\sum_{j=1}^{n} (\hat{P}(w_i|x_j, \hat{\theta})^b ||x_j - \mu_i||^2) \Big) \tag{4.6}$$

where b is a free parameter chosen to adjust the blending of different clusters and μ_i are the clusters values. In practical terms, for each input presented, all the clusters will have to adjust their weights, regarding the distance between the input and the cluster weights, which are the probabilities that the input belongs to each cluster.

Expectation-Maximization The basic idea of this algorithm is to iteratively estimate the likelihood given the data that is present. Suppose x_i is the i^{th} observation of the random variable X. Let $f_j(x|\theta_j), 1 \leq j \leq L$ be a set of L density functions, each having its parameter set θ_j. The density function of the random variable X can be modeled as a weighted sum of the L density functions as:

Algorithm	Feature Set	Session 1, %	Session 2, %	Degr., %
K-means	Pixel position + intensity	97.69	96.83	0.86
K-means	Moments $F_{20} + F_{02}$	92.33	89.14	3.19
SOM	Pixel position + intensity	97.69	96.68	1.01
SOM	Moments $F_{20} + F_{02}$	95.14	90.95	4.19
Fuzzy k-means	Pixel position + intensity	98.02	97.88	0.14
Fuzzy k-means	Moments $F_{20} + F_{02}$	93.90	90.04	3.86
Expectation-maximization	Pixel position + intensity	96.86	95.17	1.69
Expectation-maximization	Moments $F_{20} + F_{02}$	92.17	89.14	3.03

Table 4.1: Accuracy of the experimented variants of the proposed iris segmentation method.

$$f(x|\theta) = \sum_{j=1}^{L}(w_j f_j(x|\theta_j)) \tag{4.7}$$

where $w_j, 1 \leq j \leq L$ are the weights. The aim of the maximum likelihood (ML) estimation is to find the set of θ and w that maximizes the likelihood function $P(x)$ with respect to the given data x_i.

$$P(x) = \prod_{i=1}^{N}\Big(\sum_{j=1}^{L}(w_j f_j(x|\theta_j))\Big) \tag{4.8}$$

The observed data is supposed to be a subset of the complete data y. The Expectation Maximization algorithm starts by using an initial estimate $\hat{\theta}^0$ before performing the following two steps at each iteration: expectation step: $Q(\theta, \hat{\theta}|\theta^p) = E(log f(y|\theta)|x, \hat{\theta}^p)$; and maximization step : $\hat{\theta}^{p+1} = \arg\max_\theta Q(\theta|\hat{\theta}^p)$.

Table 4.1 contains the obtained results by the combination between feature sets and clustering (classification) algorithms. The information about the used iris images data set and the way the results were obtained is detailed in section 4.3.4. These results led us to select the fuzzy k-means algorithm and a feature set with three discrete features: (x, y) that correspond to the pixel position and $I(x, y)$ to its intensity. As can be seen, considering all the evaluated algorithms, this configuration obtained the smallest degradation between the first and the second capture-session images, thus presenting a more robust behavior when dealing with noisy data.

4.3.3 Optimizations to the Segmentation Method

After the decision about the feature set and classification algorithm of our proposal, we tested several algorithm optimizations: the application of morphological, blur and histogram operations in the preprocessing stage and several variants of the edge detector. These optimizations are described in the following subsections and were respectively applied before the feature extraction stage illustrated in figure 4.2 (morphologic and blur operations) and in replacement of the Canny edge detector.

4.3.3.1 Morphologic Operations

The term morphological processing refers to certain operations where an object hits a structuring element and is reduced to a more revealing shape [48]. The aim is to transform the signal into a simpler one by removing irrelevant information and can be applied to binary and gray level signals. Similarly, in the iris segmentation compass the aim is to eliminate eventual noisy data and smooth the information with the purpose of facilitating the segmentation.

Most morphological operations can be defined in terms of two basic operations: erosion and dilation. The eroded image of an image I with respect to a structuring element S, is the set of all reference points x for which S is completely contained in I:

$$I \ominus S := \bigcup \{x : S + x \subset I\} \tag{4.9}$$

In short, starting from images with darker foreground than background, this operation is achieved trough the replacing of every pixel in the original image by the maximum intensity within a window centered at the analyzed pixel.

The dilated image of an object I with respect to a structuring element S, is the set of all reference points for which I and S have at least one common point:

$$I \oplus S := \bigcup \{x : S + x \in I\} \tag{4.10}$$

Similarly to the above operation, this is achieved through the replacing of every pixel of the original image by the minimum intensity value of those located within a window centered at the analyzed pixel.

Based on the dilation and erosion operations, we implemented the image opening and closing and evaluated the improvements in the segmentation accuracy. Opening and closing

are dual: the first corresponds to the image erosion followed by image dilation and the latter to the opposite (image dilation followed by image erosion).

4.3.3.2 Blur Operations

It is expectable that the iris images captured within non-cooperative environments contain high frequency information correspondent to noise and irrelevant information, such as some of the factors presented in section 2.2.4.4. Blur operations, that basically consist of low-pass filters that remove the higher frequency components of the images, are a very common technique typically applied in the preprocessing stage to facilitate the segmentation task. In this context, we implemented and tested the following blur operators: Gaussian [48], Median [48] and ISEF [104] low-pass filters.

4.3.3.3 Histogram Operations

Histogram Equalization

This operation is widely used in image processing, in order to get some normalization of the images characteristics. It reassigns the intensity value of the pixels based on the image histogram. Individual pixels retain their intensity order, that is, they remain brighter or darker than other pixels, but the values are shifted, so that an equal number of pixels have each possible brightness value. Let j be the intensity value of a pixel in the original image. The new value k is given by:

$$k = \sum_{i=0}^{j} \frac{N_i}{T} \tag{4.11}$$

where N_i is the number of pixels with intensity value i and T is the number of pixels that the image contains.

Histogram Stretch

This is a contrast enhancement technique that spreads the pixels' intensity to the upper and lower limits of the scale (usually 0 and 255 in grayscale images). It attempts to improve the contrast of an image by spreading the range of intensity values to span a desired range of values - e.g. the the full range of pixel values that the image type allows. Let m and M be respectively the minimum and maximum intensity values of the original image and j be the intensity value of a pixel in the original image. The new intensity value k is given by:

$$k = S * \frac{(j-m)}{(M-m)} \tag{4.12}$$

where S is the maximum allowable value according to the image representation, usually 255 in grayscale images as the ones that we have to deal with.

4.3.3.4 Edge Detection Algorithms

Canny Edge Detector

The Canny [12] edge detector is commonly considered the optimal edge detector operator. It receives a grayscale image and outputs a binary map correspondent to the identified edges. It starts by a blur operation followed by the construction of a gradient map for each image pixel. A non-maximal suppression stage sets the value of 0 to all the pixels of the gradient map that have neighbors with higher gradient values. Further, the hysteresis process uses two predefined values to classify some pixels as *edge* or *non-edge*. Finally, edges are recursively extended to those pixels that are neighbors of other edges and with gradient amplitude higher than a lower threshold.

In the iris segmentation literature it is common to weight differentially some edge directions. This operation is accomplished through the multiplication of the horizontal and vertical derivatives by values in the [0,1] interval. As an example, in the detection of the scleric iris border, which usually is obstructed by eyelids and eyelashes in the regions with higher horizontal gradient values, the vertical directions are usually privileged with weight values close to 1.

In the experiments, the implemented algorithm receives the following arguments:

Upper threshold This parameter is used in the hysteresis operation. Sets the higher values of the gradient map to be considered as *edge* points.

Lower threshold In the hysteresis operation pixels with gradient values lower than this are immediately considered as *non-edge* points.

Gaussian kernel dimension As above referred, in order to remove high frequency information, the algorithm starts with a blur operation in the image. The power of this operation is determined by the width of the Gaussian kernel used in the bi-dimensional image convolution. The higher is the kernel dimension, the lower will be the resultant frequency components in the blurred image. This parameter has strong influence in

the overall computation time, since higher values significantly increase the computation time.

Sigma of the Gaussian kernel This parameter defines the standard deviation of the bi-dimensional Gaussian kernel. Higher values increase the power of the blur operator and result in less number of detected edges.

Vertical edges weight This is used to weight the vertical derivatives in the gradient map construction. It is usually in the [0, 1] interval and is multiplied by the vertical derivative value.

Horizontal edges weight Similarly to the above parameter, it is the correspondent regarding the horizontal derivatives. It must be noted that, usually, the sum of the vertical and horizontal weight values must be equal to 1.

Shen-Castan Edge Detector

This operator [104] receives a grayscale image and outputs a binary map correspondent to the identified edges. It starts by the removal of the higher frequency information, usually correspondent to noise, followed by the edge detection through a Laplacian-based kernel. The resultant intensity values are compared and edges are detected according to the a priori user defined proportion of edges in the image. The implemented algorithm receives the following arguments:

Width of the gradient kernel This is used to smooth the image by the Laplacian kernel. It has strong impact in the final computation time, which is directly proportional to the width of the kernel.

Smoothing factor This value is applied in the ISEF [104] blur operation and determines the amount of information correspondent to the higher frequencies that are removed in the preprocessing stage.

Edge ratio This parameter is used after the application of the Laplacian kernel. It is closed in the [0,1] interval and dictates the proportion of pixels that are classified as edges.

Zero-Crossing Detector

This is a well known and widely used edge detector [69] used in common image processing. It starts by the bi-dimensional convolution of the image with a Gaussian kernel,

followed by an approximation to the gradient through a Laplacian filter. Edges are identified as the points with changes in the gradient signal. We implemented an optimized version that uses an hysteresis-like process to expand the edge-map and to constrain the minimum number of connected pixels that are considered as part of the edges. It receives the following parameters:

Filter dimension This value determines the width of the Gaussian and of the Laplacian kernels, respectively used as low-pass filter and gradient estimator.

Gaussian kernel sigma Higher values of this parameter reduce the number of identified edges. As in the above described Canny edge detector, the Gaussian kernel is used to remove the higher frequency components, that are commonly correspondent to noise.

Minimum of connected pixels This parameter defines the minimum number of pixels that must be connected, either using 4 or 8 neighboring, to be considered as part of an edge.

Upper threshold This parameter is used in the hysteresis process to a priori classify as *edge* the pixels with higher gradient amplitude.

Lower threshold Similarly to the above parameter, it classifies the pixels with lower gradient amplitude as *non-edge*.

4.3.4 Experiments and Discussion

In the experiments we evaluated the accuracy of the above described segmentation processes in the chosen data set. For every image, we started by the detection of the scleric border followed by the pupillary border. We assumed that both have circular form, thus, each one is completely defined by its center (x, y) and radius r values. Further, we overlapped the detected circumferences and the respective iris image and evaluated the segmentation accuracy by visual inspection.

We considered the segmentation as accurate exclusively when both circumferences, correspondent to the pupillary and scleric borders, fall exactly into the respective iris borders, as illustrated by figures 4.4a and 4.4b. Oppositely, figures 4.4c and 4.4d exemplify failed segmentation processes, respectively due to iris extreme eyelids obstructions and large reflection areas in the iris and pupil regions.

(a) Accurate iris segmentation.

(b) Accurate iris segmentation.

(c) Failed iris segmentation induced by eyelid obstructions.

(d) Failed pupil segmentation induced by specular and lighting reflections.

Figure 4.4: Examples of segmented iris images from the $UBIRIS$ database.

4.3.4.1 Data Sets

As stated above, segmentation plays a crucial role in the overall success of the recognition system. Being the first stage of the recognition process, it must directly deal with the noise factors and heterogeneous characteristics of the images, thus attaching higher relevance to robustness. After the analysis of the available iris image databases, that are described in chapter 3, we chosen the 1877 images from the $UBIRIS$ database. Thus, the data set used in the segmentation experiments - $UBIRIS_{seg}$ - is comprised by all the 1877 images of the database. The statistical information about the quality of the images and the main characteristics of the data set are, respectively, described in chapter 3 and appendix B.

4.3.4.2 Results

The obtained results are given in table 4.2. The first column identifies the method, the second specifies eventual parameter modifications, where ”HEP”, ”MOP” and ”TP” respectively stand for ”histogram equalization preprocess”, ”morphological opening preprocess” and ”threshold preprocess”, operations that were described in section 4.3.3. The third and forth columns contain the results obtained in images of the first and second image capture sessions. These values are expressed in percentage and correspond to a 95% confidence interval. The fifth column denotes the accuracy deterioration between the images of the first and of the second session and, finally, the last column shows the average computation time of each method (in seconds).

Method	Parameters	Session 1, %	Session 2, %	Degr., %	Tm., s
Daugman	-	95.22 ± 0.02	88.23 ± 0.03	6.99	2.73
Daugman	HEP	95.79 ± 0.01	91.10 ± 0.02	4.69	3.01
Daugman	MOP	93.18 ± 0.01	90.91 ± 0.02	2.27	3.27
Daugman	TP (128)	96.54 ± 0.01	95.32 ± 0.02	1.22	2.92
Wildes	-	98.68 ± 0.00	96.68 ± 0.01	2.00	1.95
Wildes	HEP	98.74 ± 0.00	95.62 ± 0.01	3.12	2.23
Wildes	MOP	98.68 ± 0.00	96.68 ± 0.01	2.00	2.48
Wildes	Shen and Castan edge detector	96.29 ± 0.01	95.47 ± 0.02	0.82	2.49
Wildes	Zero-crossing edge detector	94.64 ± 0.01	92.76 ± 0.02	1.88	2.51
Camus and Wildes	Number of directions=8	96.78 ± 0.01	89.29 ± 0.03	7.49	3.12
Camus and Wildes	HEP, number of directions=8	95.81 ± 0.01	88.31 ± 0.03	7.50	3.42
Camus and Wildes	MOP, number of directions=8	95.60 ± 0.01	88.05 ± 0.03	7.55	3.71
Martin-Roche *et al.*	-	77.18 ± 0.03	71.19 ± 0.04	5.99	2.91
Martin-Roche *et al.*	HEP	78.21 ± 0.03	72.45 ± 0.04	5.76	3.20
Martin-Roche *et al.*	MOP	78.10 ± 0.03	72.28 ± 0.04	5.82	3.38
Tuceryan	Total clusters=5	90.28 ± 0.02	86.72 ± 0.03	3.56	4.81
Proposed Method	-	98.02 ± 0.01	97.88 ± 0.01	0.14	2.30
Proposed Method	HEP	98.28 ± 0.01	98.91 ± 0.01	0.37	2.60
Proposed Method	MOP	97.90 ± 0.01	97.18 ± 0.01	0.72	2.81

Table 4.2: Comparison between the accuracy of the tested segmentation algorithms and our proposal in images of the $UBIRIS$ database.

In the context of non-cooperative recognition, the most relevant value is the accuracy degradation as function of the images' quality. We observed that our method is clearly less dependent of the image characteristics, since it presented the smallest accuracy degradation between both sessions - just about 0.14%. This is in contrast with all the remaining methods, specially those proposed by Martin-Roche *et al.* [70], Daugman [18] and Camus and Wildes [11]. It must be stressed that our method is the one that presented the highest accuracy on images from the second session, indicating that it is well adapted to deal with noisy images.

Wildes' [120] method achieved the best results in absolute terms, having 98.74% accuracy on the first session images. However, as the image quality decreases, its accuracy degraded more than 2%. This fact may indicate that, if we incorporate other noise factors, its accuracy will be strongly affected, which discourages its use in the non-cooperative setting. The implemented variants of this method, both the preprocessing methods and the

alternative edge detection algorithms, didn't get significant improvements when compared to the original method.

Daugman's [18] method has one important advantage: it is not dependent of any parameter value. This fact may, in theory, potentiate its robustness, but the results showed that its accuracy is influenced by the images quality, namely the requirements of a sufficient separability between the intensities of the iris and sclera regions. Specially in the iris images with higher intensity values (blue or green irises), where the intensity difference between the iris and sclera regions is not as large, the method's seek strategy for the maximal difference between consecutive circumferences tends to identify regions tangent to the pupil region, which have considerable high contrast.

The approaches similar to Daugman's, such as Camus and Wildes [11] and Martin-Roche *et al.* [70], presented similar problems. These methods proved to be effective on good quality images, but significantly deteriorated their accuracy when the iris contains large reflection areas or significant eyelids and eyelashes obstructions.

Regarding the Tuceryan method [113], the fact that it was not specifically thought for iris recognition can probably explain that its average accuracy was about 7% worst than the specific iris segmentation proposals. Apart from this, the accuracy degradation (around 4%) was in both cases higher when compared with other approaches. Moreover, as figure 4.3 illustrates, we concluded that the geometric moments do not have sufficiently discriminant capacity to distinguish between the iris regions, inducing frequently the failure in the segmentation.

Finally, regarding the tested optimizations to the proposed methods, we observed that, apart from small and circumstantial improvements in some of the methods, none of them proved to consistently contribute for the improvement of segmentation's accuracy and robustness.

Computation Time

All the algorithms were implemented in C++, following an object-oriented paradigm, running in an image processing framework developed by the authors and described in appendix A. This framework is clearly not optimized for execution speed, as the algorithm's implementation was made without these concerns, but instead with a user-friendly objective.

The "Time" column of table 4.2 contains the average execution time from each of the tested segmentation processes. These values were obtained by averaging 100 segmentation processes on 100 random chosen $UBIRIS$ images. Regarding these values, we observed

that the classical edge detection followed by circumference fitting algorithm (Wildes) is more efficient than all the remaining ones.

Our proposal's computation time is about 17% higher than that of Wildes' algorithm, These 17% are used in the feature extraction and clustering process. We consider that with proper algorithm optimization this computation time gap (about 0.3 seconds) will become irrelevant.

4.3.5 Conclusion

In the latter sections we described the challenging task of iris segmentation, which gains higher relevance in the context of the non-cooperative image capturing. We presented some of the most cited methods in the iris segmentation literature and used $UBIRIS$ [89] database to show that they are strongly dependent of the specific image characteristics and noise factors, yielding a low robustness level.

On the basis of this fact, we proposed a new iris segmentation method that consists on the selection of three discrete features followed by the application of the well known fuzzy-clustering algorithm. This produces an intermediate image that tends to be more homogeneous, even on images captured within highly dynamic environments. Our experiments showed that, for these non-optimal images, the creation of an intermediate labeled image improves the segmentation robustness and is, therefore, adequate for the application on the non-cooperative iris recognition setting.

4.4 Segmentation Inaccuracies

The dynamics of the image capturing environments can easily contribute to the existence of segmentation inaccuracies. Moreover, we experimentally found that a significant number of the recognition errors were due to inaccurate iris segmentation. Based on these facts, we analyzed the relationship between the accuracy of the iris segmentation and the error rates of typical recognition proposals. In order to achieve this, we implemented the following process:

1. Selection of 2000 images from the $UBIRIS$ [89] and $CASIA$ [44] databases. Verification, by visual inspection, that the used segmentation algorithm is able to accurately segment all the images.

2. Feature extraction 1. Extraction of the iris signatures, according to three distinct feature extraction methods that represent the most common iris recognition proposals.

3. Feature comparison 1. Comparison, through the Hamming distance, between the iris signatures extracted from the same data set.

4. Introduction of segmentation inaccuracies. Change in the implementation of the segmentation algorithm, in order to less accurately detect the iris borders.

5. Feature extraction + comparison 2: extraction and comparison of the resulting signatures, as described in steps 2 and 3.

We stress that this analysis is independent of the choice of the segmentation algorithm, as we manually verified that the one used was able to accurately identify both the iris borders of all data set images. On the other hand, it is dependent of the three tested feature extraction strategies ([18], [1] and [67]), that have as common points the utilization of normalized and dimensionless iris images and the extraction and comparison of binary iris signatures.

4.4.1 Types of Segmentation Inaccuracies

The used iris segmentation method approximates both the scleric and pupillary borders as circumferences. Therefore, each border can be defined by its center coordinates (x, y) and radius r. Let (x_d, y_d) and r_d be respectively the center coordinates and radius of the circumference detected by the segmentation algorithm. Also let (x_t, y_t) and r_t be similar circumference parameters of the real iris border.

Through software changes in the implementation of the segmentation algorithm, we introduced two types of errors:

Translation Errors: we defined a translation error with amplitude of p pixels when $|x_d - x_t| + |y_d - y_t| = p$. It occurs when the center of the detected circumference is deviated p pixels from the center of the true circumference. Figures 4.5a and 4.5b exemplify translation errors, respectively on the pupillary and scleric borders.

Scale Errors: as illustrated by figures 4.5c and 4.5d, scale errors occur when the detected and the real circumferences have different radius values. If $|r_d - r_t| = p$ then we defined it as a scale error with amplitude of p pixels.

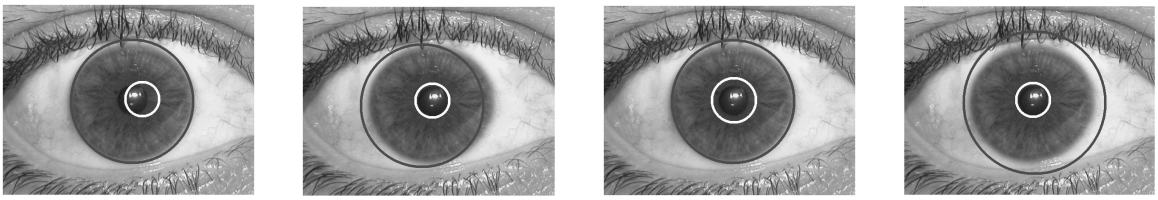

(a) Translation error on the segmented pupillary border.

(b) Translation error on the segmented scleric border.

(c) Scale error on the segmented pupillary border.

(d) Scale error on the segmented scelric border.

Figure 4.5: Examples of inaccurately segmented iris images.

As figure 4.5 illustrates, these two types of errors on each iris border enable the appearance of four distinct segmentation errors: translation errors on the scleric border, translation errors on the pupillary border, scale errors on the scleric border and scale errors on the pupillary border. Other types of errors, such as those that can be expressed as a combination of the previously defined, were not the subject of this analysis.

4.4.2 Experiments and Discussion

The segmentation stage was accomplished through the method proposed by Wildes [120]. In order to enable the experiments, we manually verified that this algorithm accurately detected the pupillary and scleric iris borders of all images of the data sets. The cartesian to polar transformation was made through the Daugman rubber sheet [18], that produces a dimensionless polar representation of the iris with fixed dimensions of (512 $\times$ 64) pixels (width $\times$ height).

Three distinct feature extraction methods were implemented. They are described respectively in [18], [67] and [1] and have as common point the production of binary iris signatures, which enabled the comparison through the Hamming distance, as described in [18].

4.4.2.1 Data Sets

In order to analyze the impact of segmentation inaccuracies both in highly and less noisy iris images, we constructed two data sets ($UBIRIS_{ina}$ and $CASIA_{ina}$) composed respectively by 1000 images of the $UBIRIS$ and 1000 images of the $CASIA$ databases. We selected 10 images from 100 subjects, enabling respectively 4500 and 495000 intra- and inter-class

comparisons. Images of the $UBIRIS$ database have fixed dimensions of 400 $\times$ 300 pixels (width $\times$ height) and horizontal and vertical resolution of 300 dpi. The irises have radius values between 80 and 100 pixels and the pupils between 15 and 35 pixels. Images of the $CASIA$ database have 320×280 pixels (width $\times$ height) and horizontal and vertical resolution of 96 dpi. The iris radius have values respectively between 87 and 110 and the pupils between 20 and 45 pixels. Other characteristics of the $UBIRIS_{ina}$ and $CASIA_{ina}$ data sets are given in appendix B.

4.4.2.2 Results

When comparing two iris signatures through the Hamming distance, a dissimilarity measure comprised in the [0,1] interval is produced, which is directly proportional to the compared irises dissimilarity. At each iteration of our experiments, we made all possible intra- and inter-class comparisons between iris signatures, while varying the accuracy of the segmentation algorithm.

Table 4.3 contains the average values obtained in the intra- and inter-class comparisons between images of $UBIRIS_{ina}$ and $CASIA_{ina}$ data sets. "Avg. Intra-Class" and "Avg. Inter-Class" correspond respectively to the average dissimilarity between signatures extracted from the same and from different irises. "Std. Intra-Class" and "Std. Inter-Class" indicate the respective standard deviations. "FRR, FAR=0" corresponds to the false rejection rates when the false acceptances were minimized and, finally, "EER" corresponds to the approximated equal error rate.

Not surprisingly, the highest separability between the intra- and inter-class comparisons was observed with accurate iris segmentation. Interestingly, we found that translation errors in the pupillary border have the strongest impact in the recognition's accuracy. In this case, the existence of minor translation errors - just above 1 pixel - significantly increased the false rejection rates and deteriorated the overall accuracy of the recognition system.

Regarding the scleric iris border, we observed a much more tolerant behavior of the recognition processes to segmentation inaccuracies in this border, which can be explained by two reasons: first, the interior part of the iris contains the majority of the information used in the recognition and, second, the process that makes the transformation from the cartesian to the polar and dimensionless coordinates system takes the pupil center as basis for its operations.

Segmentation Error	Avg. Intra-Class		Std. Intra-Class		Avg. Inter-Class		Std. Inter-Class		FRR, FAR=0, %		EER, %	
	CASIA	UBIRIS	CASIA	UBIRIS	CASIA	UBIRIS	CASIA	UBIRIS	CASIA	UBIRIS	CASIA	UBIRIS
No error	0.158	0.180	0.002	0.005	0.412	0.392	0.001	0.001	0	0	0	0
Translation error on the pupillary border												
1 pixel	0.173	0.233	0.003	0.005	0.414	0.394	0.002	0.002	2.086	16.831	1.530	8.300
2 pixels	0.190	0.284	0.004	0.006	0.415	0.403	0.002	0.003	2.277	22.081	3.306	8.599
3 pixels	0.220	0.318	0.003	0.007	0.414	0.413	0.003	0.002	6.207	40.922	4.891	11.171
4 pixels	0.247	0.350	0.004	0.005	0.423	0.417	0.002	0.003	9.003	56.183	5.977	18.787
5 pixels	0.267	0.372	0.001	0.004	0.427	0.423	0.003	0.001	13.199	80.019	6.318	21.834
Translation error on the scleric border												
1 pixel	0.173	0.189	0.003	0.000	0.414	0.392	0.002	0.001	0	0	0	0
2 pixels	0.190	0.202	0.004	0.001	0.415	0.397	0.002	0.000	0	0	0	0
3 pixels	0.220	0.208	0.003	0.001	0.414	0.397	0.003	0.001	0	0	0	0
4 pixels	0.247	0.208	0.004	0.001	0.423	0.397	0.002	0.001	0	0	0	0
5 pixels	0.267	0.221	0.001	0.001	0.427	0.401	0.003	0.001	0	0	0	0
10 pixels	0.290	0.256	0.001	0.002	0.427	0.401	0.003	0.001	2.093	10.119	1.318	3.494
Scale error on the pupillary border												
1 pixel	0.170	0.183	0.001	0.000	0.419	0.392	0.002	0.001	0	0	0	0
2 pixels	0.181	0.200	0.002	0.001	0.417	0.394	0.002	0.001	0	0	0	0
3 pixels	0.187	0.211	0.001	0.001	0.421	0.402	0.003	0.000	0	0	0	0
4 pixels	0.209	0.233	0.001	0.003	0.421	0.404	0.002	0.002	0	4.380	0	1.992
5 pixels	0.211	0.245	0.001	0.004	0.424	0.412	0.003	0.000	1.133	20.173	0.372	6.295
Scale error on the scleric border												
1 pixel	0.181	0.191	0.002	0.002	0.411	0.394	0.002	0.000	0	0	0	0
2 pixels	0.184	0.202	0.002	0.003	0.414	0.398	0.001	0.001	0	0	0	0
3 pixels	0.192	0.214	0.002	0.002	0.423	0.402	0.002	0.001	0	0	0	0
4 pixels	0.201	0.224	0.001	0.004	0.428	0.402	0.001	0.001	0	0	0	0
5 pixels	0.217	0.245	0.003	0.003	0.434	0.412	0.003	0.000	1.133	4.821	0	1.733

Table 4.3: Iris recognition results regarding the existence of segmentation inaccuracies.

Figure 4.6 illustrates a significant degradation in the recognition's accuracy when we introduced translation errors on the pupil segmentation, using the $UBIRIS_{ina}$ and $CASIA_{ina}$ data sets. The left histograms (figures 4.6a and 4.6c) correspond to accurate iris segmentation and the right ones (figures 4.6b and 4.6d) to translation errors with amplitude of 3 pixels on the pupil segmentation. The darker and brighter bars correspond respectively to the intra- and inter-class comparisons. It can be seen that the separability between both types of comparisons was considerable reduced, which significantly increased the error rates. Moreover, we concluded about an increase in the error rates directly proportional

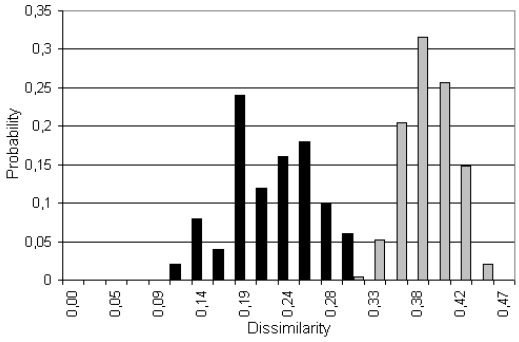

(a) *Accurate segmentation in the $UBIRIS_{ina}$ data set.*

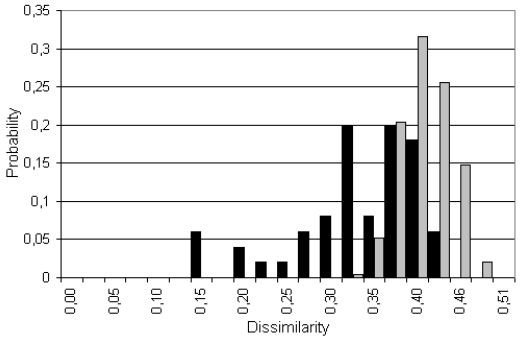

(b) *Translation errors of 3 pixels in the pupillary border segmentation ($UBIRIS_{ina}$ data set).*

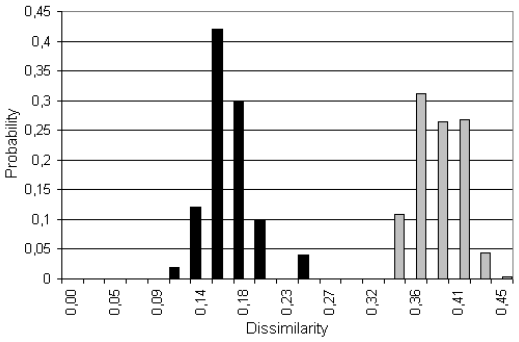

(c) *Accurate segmentation in the $CASIA_{ina}$ data set.*

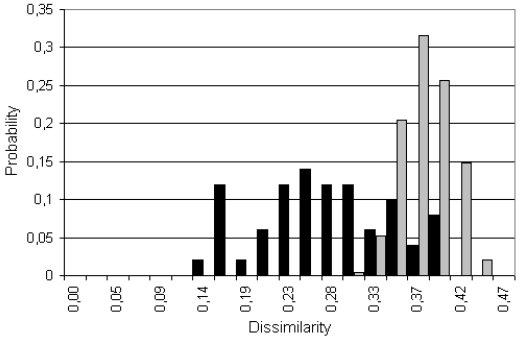

(d) *Translation errors of 3 pixels in the pupillary border segmentation ($CASIA_{ina}$ data set).*

Figure 4.6: Comparison between the histograms of the signatures dissimilarities when varying the accuracy of the iris segmentation.

to the amplitude of this type of segmentation inaccuracies. This can be confirmed by figure 4.7, which contains a comparison between the receiver operating curves obtained with translation errors on the pupillary border with amplitude of respectively 1 (continuous line) and 3 pixels (dashed line).

4.4.3 Detection of Translation Errors in The Pupillary Border

Based on the above described observations, in this section we describe a method that identifies translation errors in the segmentation of the pupillary border. This method can be helpful to avoid the continuation of the recognition process to further stages and, perhaps,

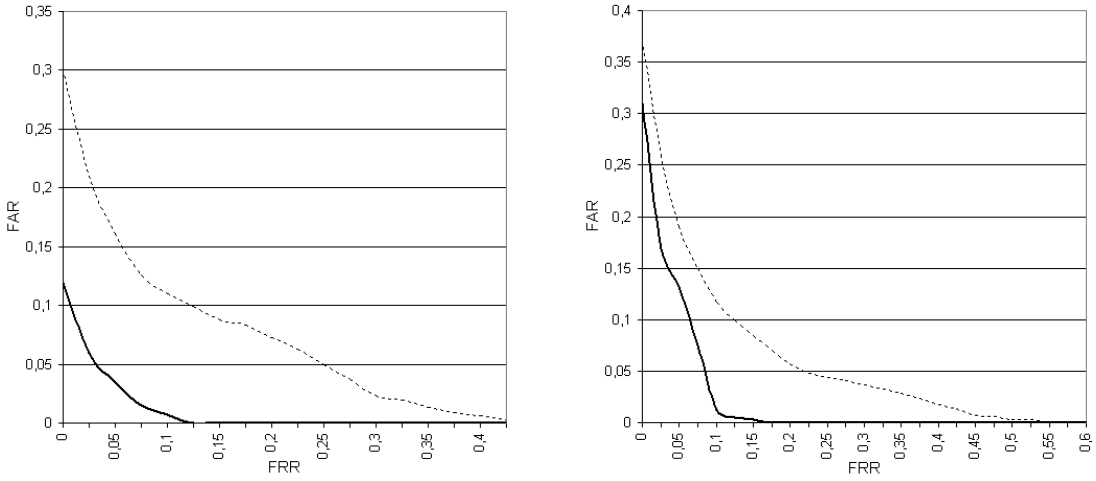

(a) Receiver operating curves obtained in the $CASIA_{ina}$ data set.

(b) Receiver operating curves obtained in the $UBIRIS_{ina}$ data set.

Figure 4.7: Comparison between the ROCs obtained when varying the amplitude of the segmentation inaccuracies in the pupillary border (continuous and dashed lines respectively represent errors with amplitude of 1 and 3 pixels).

to redirect the iris images to alternative segmentation algorithms, specialized in such tasks and, possibly, with higher computational requirements.

4.4.3.1 Proposed Method

When a translation error on the pupil segmentation occurs, a portion of the pupil will be considered as belonging to the iris (figure 4.5a). Independently of the subjects' age, gender or ethnic group, the pupil is always darker than the iris and we used this as the rationale basis of our method. Moreover, in the normalized and dimensionless iris image, the wrongly identified portion of the pupil is located on the upper band of the image, as exemplified by figure 4.8.

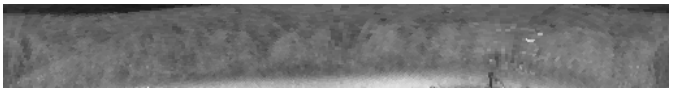

Figure 4.8: Normalized iris image with a translation error on the pupil segmentation.

Therefore, on the upper part of the normalized iris image we computed the average intensity of the pixels located within windows of size $w \times w$ and noticed distinct dis-

tributions of these values. On the accurately segmented irises, values were clearly more homogeneous and an experimentally chosen threshold (T) and window width (w) allowed the discrimination between the accurately and inaccurately segmented pupils.

Formally, let $I(i, j)$ be the intensity value of the pixel located at row i and column j of the normalized iris image. Also, let $A = \{a_0, a_1, \ldots, a_{n-1}\}$, be a set of average values, where each a_k is given by the following equation:

$$a_k = \frac{1}{w * w} \sum_{i=0}^{w-1} \Big(\sum_{j=k*w}^{(k+1)*w-1} I(i, j) \Big). \tag{4.13}$$

Let Avg be the average value of the elements of A: $Avg = \frac{1}{n} \sum a_k$ and T a threshold. If there is an a_k such that:

$$|a_k - Avg| > (T * Avg) \tag{4.14}$$

then the image is classified as containing a translation error in the pupil segmentation. As stated above, the rationale for this method is straightforward: the large separability between the iris and pupil intensities makes it more probable that some a_k computed within a window where the majority of the pixels corresponds to the pupil is highly deviated from the Avg value.

4.4.3.2 Results

The above described method was tested using the same data sets described in section 4.4.2.1. Similarly to the previous experiments, we introduced translation errors on the pupil segmentation and evaluated the method accuracy in the detection of these errors. Table 4.4 gives the obtained results. The first column specifies the amplitude of the translation error (number of pixels). The second and third columns contain the information respectively about the method's false positives (FP, wrong classification of "inaccurate segmentation") and negatives (FN, wrong classification of "accurate segmentation") and are expressed in percentage.

The experiments led us to choose the values 0.3 for the threshold parameter T and 3 for the window width w. In this case, just about 0.38% of the reported bad segmentations were wrongly classified. Even when the translation error is minimal (1 pixel), the proposed method presented low error rates. For translation errors with amplitude higher than 1 pixel,

the error was equal to zero (all the translation errors were detected and none of the accurately segmented was classified as inaccurate).

Translation error in the pupillary border, pix	FP, %	FN, %
0	0.38	0
1	0	2.19
2, 3, 4 and 5	0	0

Table 4.4: Results of the proposed method on the identification of inaccuracies in the pupil segmentation

4.4.4 Conclusion

In the latter sections we analyzed the important role of the iris segmentation accuracy in the overall recognition success. We used two different iris data sets that allowed us to observe a significant increase of the error rates when the segmentation is inaccurate, either in highly or less noisy images.

Moreover, having defined four types of segmentation inaccuracies, we observed the highest increment of the error rates when the pupillary border is inaccurately segmented (translation errors). In this situation, minimal errors with amplitude just above one pixel, have strong impact in the false rejection rates, which essentially can be essentially explained by the fact that common iris normalization methods take the pupil center as the reference point for their task.

Based on this, we proposed a method for the detection of translation errors on the pupil segmentation. This method can avoid that the recognition process continues and that the system wrongly outputs a *non-match*, which is the typical answer when the iris segmentation is not accurately performed. Simultaneously, the information about the rough iris localization can be provided to alternative segmentation algorithms, perhaps with higher computational requirements, in order to accurately perform segmentation.

4.5 Summary

In this chapter we overviewed the most common iris segmentation methods and showed a significant degradation in their effectiveness when dealing with noisy iris images, such as those contained in the $UBIRIS$ database. With the purpose of overcoming this lack of robustness, we described our iris segmentation proposal and, through a comparison between the results obtained in images of the $UBIRIS$ database, concluded about its higher robustness to noise factors, making it propitious for the application in the non-cooperative setting. Further, in section 4.4 we analyzed the variability of the recognition errors regarding the accuracy of the segmentation algorithm. Having observed a significant impact on these when the pupillary border is not accurately segmented, we proposed a method that is able to detect this kind of inaccuracies.

Chapter 5

Noise Detection

As stated above, it is highly probable that the captured irises resultant of non-cooperative imaging environments contain several other types of information. This chapter is concerned with the detection (localization) of these regions, which for our purposes are considered as *noisy*. Having stressed the difference regarding the common meaning of *noise* in the general image processing domain, we overview and establish a classification of the most common noise detection methods in the iris biometrics compass. Further, we describe our proposal, which is based in the extraction of eight well known features for each image pixel, followed by the classification through a feed-forward neural network. As the experiments report, this method proved its effectiveness and accuracy in images of the $UBIRIS$ database. Later, in section 5.5 we describe our first and intuitive approach to deal with noisy iris regions: their replacing by new information obtained through interpolation of the noise-free ones. However, we experimentally concluded that this procedure, commonly designated as *image inpainting*, does not present relevant benefits to the recognition of noisy iris images.

5.1 Noise

Image noise can be defined as the degree of variation of pixel values caused by the statistical nature of the detection process. Commonly, it refers to stochastic variations in the pixels' intensities, rather than deterministic distortions such as shading or lack of focus. In the digital image capturing, there are three common types of noise [72]:

- Random noise. This type of noise results of short exposure times or high ISO speed. It is characterized by intensity fluctuations above and below the real image intensity

and its pattern present highly variations, even with similar exposure settings.

- Fixed pattern. Includes the often called *hot pixels*, which intensities far surpass those resultant of random noise and are usually due to long exposure times or low ISO speed. The pattern associated with this type of noise is quite predictable, since it will show similar distribution of the hot pixels in images captured in similar conditions.

- Banding noise. It is highly dependent of the digital capturing devices and appears when the camera reads data from the digital sensor. It is most visible at high ISO speeds, in shadows or when the image is excessively brightened.

However, as detailed in section 2.2.4.4, for the terms of our work and of this thesis the meaning of noise is quite distinct: we considered as *noisy* the image regions that correspond to any other types of information apart from the iris and are localized within the region delimited by the pupillary and scleric iris borders. As they obstruct portions of the iris texture, ideally they should not be captured because they significantly increase the challenges of the biometric recognition itself. Moreover, in the iris recognition literature it is common the reference to the term *noise* for all the information that obstructs portions of the iris.

5.2 Noise Factors in Normalized Iris Images

In section 2.2.4.4 we detailed the most common types of information that obstruct the iris texture captured within non-cooperative imaging settings. This section analyzes the localization of these noise regions within the segmented and normalized iris image, which, as described below, is the one used as basis for our noise detection proposal.

Figure 5.1 illustrates the most common noise regions that result of non-cooperative imaging processes, either in the captured (figure 5.1a) and in the segmented and normalized iris image (figure 5.1b). Eyelids and eyelashes obstructions are usual in the lower part of the normalized images (numbers 1 and 2), corresponding to the upper and lower iris extremes that are naturally obstructed by eyelid movement. Oppositely, since these are determined by heterogeneous lighting conditions, both specular and lighting reflections are highly disseminated across the irises and are in this example signalled with numbers 3 and 4. Finally, the noise region signalled with number 5 is due to the inaccurate pupil segmentation, that resulted in the wrong classification of a portion of the pupil as belonging to the iris.

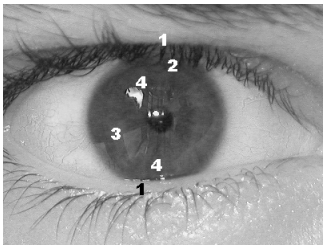

(a) Captured iris image.

(b) Segmented and normalized iris image.

Figure 5.1: Common types of noise in the captured and normalized iris images.

In the following section, we overview the most common proposals for the detection of noise regions, either through the overall classification of the noise level of the iris images or through the localization of each noise region within the irises.

5.3 Noise Detection Proposals

In order to avoid the problems originated by noise, some authors (e.g., Daugman [18]) propose to recognize individuals using exclusively portions of the iris, those where noise factors are less probable.

Zhu *et al.* [127] and Kim *et al.* [54] proposed the equalization of the histogram of the segmented and normalized iris image to reduce the effect of non-uniform illumination. The latter proposed the utilization of morphological operators to detect isolated eyelashes.

Ma *et al.* [66] proposed a global iris image enhancement by means of local histogram equalization and the removal of the high-frequency noise through Gaussian low-pass filtering.

Motivated by the observed difference between the standard deviation of the intensity values within small windows from noisy and noise-free regions, Nam *et al.* [79] and Du *et al.* [29] proposed the computation of the standard deviations within small (3×3 and 5×5 pixels) windows. If the value is higher than a threshold, the central pixel of the window is considered noise, providing the exact localization of each noise region within the image.

Wildes [120] proposed the equalization of the histogram of the whole image and the localization of the inferior and superior eyelids by means of an edge detector, followed by the linear Hough transform. As other similar approaches, this implies a search in the $\mathbb{N}^5$ space for the ellipses fitting task, which contributes to its poor performance and its dependency of the threshold parameters used by the edge detector.

In [63] a global measure of the quality of the captured images is described by Ma *et al.*, based on the analysis of its frequency distributions. Authors claim that noise-free irises have relatively uniform distribution, as opposed to those with eyelid or eyelash obstructions. In a posterior paper [64], they started by the image enhancement, through the subtraction of the average intensity computed within small image windows, followed by the local equalization of the histogram. They did not identify eyelashes or eyelids, having however concluded that a substantial part of the observed false rejections were due to the eyelid and eyelash obstruction (57.7%) and inaccurate iris segmentation (21.1%).

Kond and Zhang proposed [56] the classification of noisy iris regions directly in the captured image. They identified the separable (isolated) eyelashes through the energy of the convolution of the image with a bank of Gabor filters. The values that are lower than a threshold correspond to the noise regions. Multiple eyelashes were identified through the computation of the standard deviation within small regions of the image. Reflections were classified as *strong* (identified with a simple threshold) and *weak*. The latter simply correspond to transitions between the strong reflections and the noise-free areas and are identified through an iterative algorithm that expands the strong reflections areas.

Motivated by the problem of the high false rejection rates, Vatsa *et al.* [116] proposed the use of an edge detector followed by the linear Hough transform to detect eyelids and eyelashes. This approach was also proposed with minor variants by Ives *et al.* [47] and Huang *et al.* [38].

Based on the analysis of the energy resultant of the convolution between the image and a group of Mexican-Hat wavelets at three different scales, Chen *et al.* [14] proposed both local and global image quality measures. From our viewpoint, the database used was not adequate for the effective test of the method, since it contains almost no reflections.

The purpose of Huang *et al.* [37] was the identification of four distinct types of noise: eyelashes, eyelids, reflections and pupil. The basic idea is that there's always some type of edge between the noisy and the noise-free areas. All these edges were identified through an illumination invariant measure (phase congruency).

After analyzing each of the above mentioned proposals, we classified each one according to the following parameters:

- *Global* versus *local* methods. Global methods seek for the classification of the whole image, as *poor focused* or *obstructed iris*. Oppositely, local methods operate at the pixel level and individually classify each one, additionally providing the localization of each noise region within the iris images.

- Utilization of the *captured* versus the *normalized* iris image. Some authors propose the noise identification (usually eyelids and eyelashes) before the normalization of the segmented image. Oppositely, other authors perform first the iris segmentation and, afterwards, analyze the noisy factors in the segmented and normalized iris image.

Noise Detection Method	**Global**	**Local**	**Captured**	**Normalized**
Daugman [18]	X	-	X	-
Zhu *et al.* [127]	X	X	-	-
Kim *et al.* [54]	-	X	X	-
Ma *et al.* [66]	X	-	-	X
Nam *et al.* [79]		X	-	-
Du *et al.* [29]	-	X	X	X
Wildes [120]	-	X	X	-
Ma *et al.* [63]	X	-	-	-
Ma *et al.* [64]	X	-	-	X
Kong and Zhang [56]	-	X	X	-
Vatsa *et al.* [116]	-	X	X	-
Ives *et al.* [47]	-	X	X	-
Huang *et al.* [38]	-	X	X	-
Chen *et al.* [14]	X	X	X	-
Huang *et al.* [37]	-	X	-	X

Table 5.1: Overview of the noise detection and classification methods.

Table 5.1 establishes a classification of the studied noise detection proposals, according to the above described parameters: the utilization of the captured or the normalized iris image and the global or local noise classification, respectively at the image or at the pixel level. The ”X” sign means that the proposal has the respective characteristic, and ”-” to denotes the opposite.

It must be stressed that, from our viewpoint, few efforts have been made in the development and proposal of robust and effective methods to localize and handle noisy iris regions. In fact, we observed that most of the proposals with the exclusive purpose of noise localization are quite recent and we claim that this area deserves a lot of more attention from the researchers community, as an answer to the robustness demands.

Based on the above described analysis and conclusions, we decided to focus our efforts in the development of a noise detection proposal at the pixel level (local) using the normalized iris image. First, the attempt to recognize noisy iris images demands the localization of each noise region instead of the global image classification and, second, the utilization of the captured image, which contains more information apart from the iris, will obviously tend to decrease the method's accuracy and increase its computational complexity.

5.4 Proposed Noise Detection Method

In the following sub-sections we describe the proposed method for the detection of noise regions in normalized iris images, which, at the coarsest level, means the detection of any other types of information apart from the iris in the segmented and normalized iris image. As stated above, our method starts with the extraction of eight well known features for each image pixel, followed by the classification through a fully connected feed-forward neural network.

5.4.1 Feature Extraction

Centered at each pixel, we started by the computation of five commonly used statistical measures in small image windows, as described by Randem and Husøy [98]: angular second moment (ASM), entropy, contrast, energy and inertia. Further, we assigned the respective measure to the pixel centered at each image window and constructed the respective statistical images. Interestingly, we noticed that each of these images emphasize different types of noise, as illustrated by figures 5.2b and 5.2c. In this situation, the inertia and entropy images enhance distinct noise regions, respectively corresponding to eyelids obstructions (figure 5.2c) and to lighting reflections (figure 5.2b), as can be observed in the original iris image 5.2a.

With purposes similar to the authors of [37], we confirmed that the phase congruency accurately identifies the relevant transitions between pixels' intensities, while maintaining

(a) Normalized and noisy iris image.

(b) Inertia image.

(c) Entropy image.

Figure 5.2: Example of the enhancement of noisy iris regions through different measures.

high independence from illumination changes. Later, in order to achieve spatial relationship between image regions, we considered the position of each pixel in the normalized image as a feature. Thus, for each pixel, we computed an eight-dimensional feature vector, with the following components: (row, $column$, $entropy$, ASM, $energy$, $contrast$, $inertia$, $phase\ congruency$).

5.4.2 Classification

The classification was accomplished through a fully connected feed-forward neural network with one hidden layer. We selected 10 iris images from the data set and manually builded binary maps, similar to the illustrated by figure 5.3, that were used as learning data (training set). In this maps, the black pixels correspond to the detected noise regions and the white ones to the noise-free regions of figure 5.1.

Figure 5.3: Noise regions of figure 5.1b.

5.4.3 Experiments and Discussion

In the experiments, we compared our noise detection proposal with those proposed by Huang *et al.* [37] and Chen *et al.* [14]. They were chosen due to the fact that they provide local noise measures, the claimed invariance to illumination changes and the results presented by the authors.

5.4.3.1 Data Sets

The type of experiments described in this chapter demand the highest levels of noise in the iris images, both of several types and of large dimensions. Due to these requirements, we exclusively used images of the $UBIRIS$ database and builded a data set - $UBIRIS_{noi}$ - composed of 100 segmented and normalized iris images, together with the correspondent binary maps that provide the localization of the noise regions. These noisy maps were manually made through an image processing software and have similar appearance to the one illustrated by figure 5.6a. The normalized iris images have fixed dimensions of 512×64 (width $\times$ height) pixels and their main characteristics are detailed in appendix B.

5.4.3.2 Results

First, regarding the optimization of our method, we experimentally chosen 7×7 windows for the computation of the statistical measures described in section 5.4.1. Further, using the same data set described in section 5.4.3.1, we randomly selected 20000 noisy and 20000 noise-free pixels, which represent just 0.12% of the whole data set. We proceed to the feature extraction and used this data as the neural network training set. In order to optimize the classification, we evaluated the neural network accuracy in the test data, when varying each of the following parameters:

Number of neurons in the hidden layer Prior studies demonstrated that this number has a strong influence on the neural network ability to optimally separate the data. According to this, we varied the number of neurons in the hidden layer and repeated the learning process.

Maximum allowable error to stop the learning stage This value defines the desirable average error of the neural network when classifying the training data set. It is important to overcome the possibility of the excessive specialization of the network on the training data.

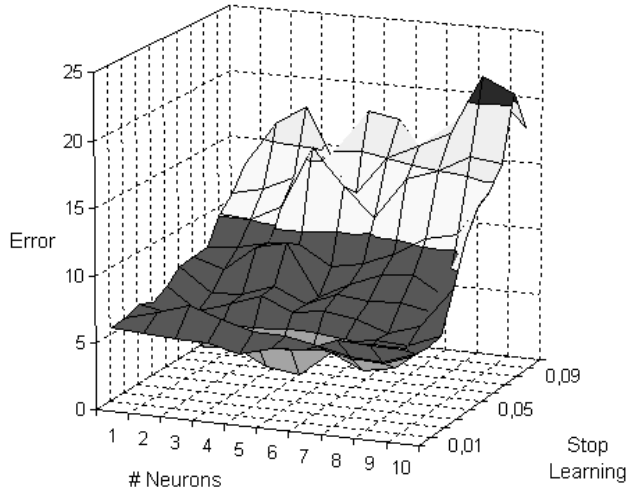

Figure 5.4: Error rates of the neural network in the training data.

Figure 5.4 illustrates the obtained error rates in the training data set. The presented values correspond to the average errors obtained after 10 repetitions of the learning process for each configuration. The "# Neurons" and "Stop Learning" axis correspond respectively to the number of neurons in the hidden layer and the minimum error value to stop the learning process. The "Error" axis contains the obtained error rates in the learning stage. This allowed us to choose a neural network with five neurons in the hidden layer and stop the leaning stage with error values below 0.03 (3%).

We tested our method in the detection of the noise regions of the data set images and compared the results with the above described processes of Huang *et al.* [37] and Chen *et al.* [14]. The evaluation of the results was made through the comparison with the correspondent binary map of each image of the data set, which are described in section 5.4.3.1.

Table 5.2 contains a comparison between the accuracy of our method and those proposed respectively by Huang *et al.* [37] and Chen *et al.* [14]. The first column identifies the method and the second contains the obtained error rate in confidence intervals of 99% and is expressed in percentage.

As can be observed, our proposal achieved a significant higher accuracy than the others used in the comparison. However, its higher computational requirements must be stressed and the fact that the other proposals were not thought to deal with the quantity of some of

Noise Detection Method	Error, %
Huang *et al.* [37]	14.61 ± 0.0501
Chen *et al.* [14]	20.83 ± 0.0570
Proposed method	2.74 ± 0.0232

Table 5.2: Comparison of the results obtained by the tested noise detection methods.

the noise factors that images of the data set contain. In fact, the images of the used data set were much more noisy than those where the other proposals were tested by their authors.

5.4.4 Conclusion

In the latter sections, we proposed a method for the localization of noise regions in normalized iris images. It is based on the extraction of six well known statistical image features together the pixel position. In the classification stage we used a fully connected feed-forward neural network with one hidden layer. Experiments led us to conclude that our method has a much better performance (only 2.74% error) than the other methods used in the comparison in highly noisy images of the $UBIRIS$ database. However, this increase in accuracy and effectiveness is obtained at the cost of an increase in the computational effort.

5.5 Image Inpainting

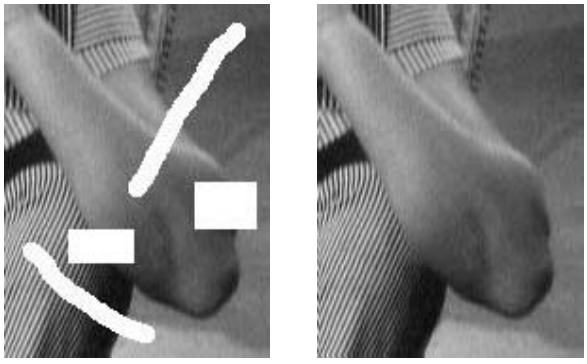

(a) *Original image.* (b) *New image, resultant of the inpainting technique.*

Figure 5.5: Example of the results of one inpainting technique [4].

Inpainting is a short term for what researchers in image processing call ”image interpolation” [105]. Digital inpainting uses spatial or frequency information to restore partially removed or damaged data from images in a visually plausible way. It can be used in photo restoration, zooming, image coding, data recovery and special effects (e.g. removal of objects) [106]. A number of algorithms specially address the image filling issue for the task of restoration, removing speckles, scratches and overlaid text from images.

Several approaches considered texture synthesis as the most suitable way to fill regions with textures. Other types of algorithms are exemplar-based techniques, which generate new textures by sampling and copying color or intensity values from the source image.

As figure 5.5 illustrates, the use of image inpainting techniques allows the substitution of corrupted or missing data in the original by new data, which ideally should preserve the most important structural or textural properties. This makes this technique the most obvious and intuitive in order to fill (replace) the noisy data, according to the textural properties of the noise-free iris regions, as exemplified by figures 5.5a and 5.5b. Here, the regions to be replaced by interpolated information are signalled by the white regions (figure 5.5a) and, as can be observed in the resultant image (figure 5.5b), were filled by noise-free information in a visually plausible way.

5.5.1 Experiments and Discussion

After studying some of the most common approaches for inpainting purposes, we selected two of them and tested their effectiveness in the painting of noisy iris images. Our aim consisted in evaluating the possibility that the localized noisy iris regions could be acceptably replaced by information from the noise-free regions. If this technique proved to be valid, then the iris recognition algorithm could deal with the resultant images as if they were absolutely noise-free.

Due to its extreme simplicity and low computational requirements, we implemented the method proposed by Oliveira *et al.* [85]. In this paper, the authors proposed the simplest and fastest inpaint algorithm, which consists of an iterative approach based on low-pass filtering through Gaussian kernels.

Oppositely, having accuracy as the main concern, we selected the proposal of Criminisi *et al.* [15]. Here, an algorithm for the removal of large objects from images is proposed, through the construction a priority value for each pixel located in the border of the region to be filled. This value is the key to define the inpaint order and, together with a block-based

sampling process, achieves results that can be favorably compared with similar techniques. However, it must be stressed the extreme computational requirements of this technique. In fact, the processing of normalized iris images with 512×64 pixels lasted in average more than six minutes, which obviously is not acceptable in the biometrics compass, but allowed us to conclude about the maximum benefits that could arise from the inpainting technique.

In the experiments, we compared the separability between the intra- and inter-class comparisons of the signatures extracted from each image of the data set, according to the recognition process described in section 2.2.3.1. First, we extracted the biometric signatures from the images as if they were completely noise-free. Further, before the feature extraction stage, we used our noise detection proposal to localize the noise regions that are further filled by the inpainting algorithms.

(a) *Result of our noise detection proposal in image 5.2a.*

(b) *Result of the inpainting algorithm [85]applied to image 5.2a.*

(c) *Resultant of the inpainting algorithm [15] applied to image 5.2a.*

Figure 5.6: Examples of the utilization of two inpainting techniques in a normalized and noisy iris image.

As figure 5.6 illustrates, both of the inpainting processes replace the information correspondent to noisy iris regions - signalled by the black regions - with interpolated information from the noise-free areas. However, the filling plausibility of both algorithms is quite different: the one of Oliveira *et al.* [85] has roughly filled the noise regions and the one of Criminisi *et al.* [15] was much more visually plausible.

5.5.1.1 Data Sets

In the experiments we used a data set - $UBIRIS_{inp}$ - which is a subset of the $UBIRIS$ database, once again due to the high noise level of its images. We selected 400 images from 40 subjects, which enabled, respectively, 1800 intra- and 78000 inter-class comparisons, and manually verified that the segmentation algorithm was able to accurately localize both iris borders, preventing that segmentation errors contribute to the increase of the error rates. The main characteristics of the data set are detailed in appendix B.

5.5.1.2 Results

The obtained results are illustrated by figure 5.7. Both sub-figures contain histograms of the dissimilarities respectively between the intra- (dark bars) and inter-class (bright bars) comparisons. Figure 5.7a contains the obtained results without the use of the inpainting algorithm, when extracting the biometric signature from the noisy iris images as if they were noise-free. Oppositely, figure 5.7b contains the obtained separability when the images were previously processed by the algorithm proposed by Criminisi *et al.*, before the feature extraction and comparison stages. As the proposal of Oliveira *et al.* was essentially tested due to its lower computational requirements and its results are worst than the other inpaint method, we do not present the respective results. The horizontal axis represents the dissimilarity values and the vertical axis the probability for the feature comparison with such dissimilarity value.

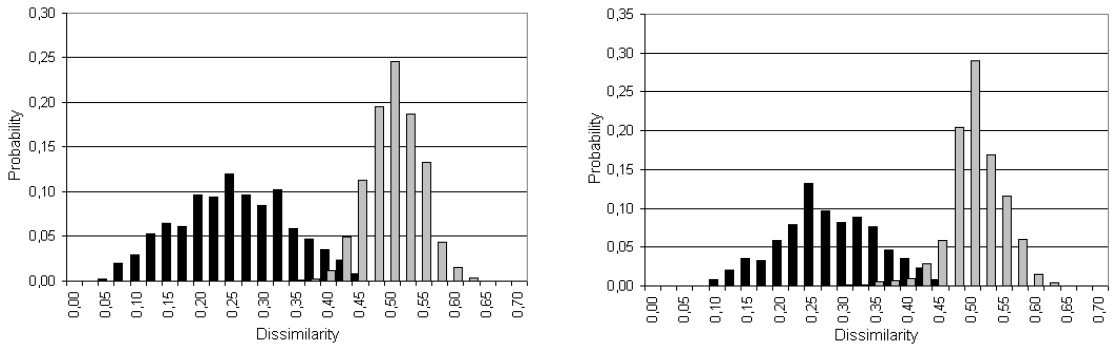

(a) *Without inpainting.* *(b)* *Using the inpainting algorithm proposed in [15].*

Figure 5.7: Histograms of the dissimilarities between the intra- and inter-class comparisons with and without the use of image inpainting techniques.

These results showed strong evidence that no significant benefits arise of the inpainting technique for the iris recognition purposes. Apart from this visual analysis, the recognition measures given in table 5.3 confirm our conclusion. The first column identifies the inpainting technique, the second contains the values of a t-test given by:

$$\tau = \frac{\mu^E - \mu^I}{\sqrt{\frac{\sigma^{I\,2}}{N^I} + \frac{\sigma^{E\,2}}{N^E}}} \tag{5.1}$$

where μ^I and μ^E respectively indicate the mean of the intra- and inter-class dissimilarities. σ^I and σ^E indicate the respective standard deviations and N^I and N^E are, respectively, the number of intra- and inter-class comparisons. The third column contains the approximated equal error rates and the forth contains the false rejections rates when the false acceptances were minimized. The last two columns are in percentages.

Inpainting algorithm	τ	**EER, %**	**FRR, FAR=0, %**
None	64.880	2.090	15.556
Oliveira *et al.* [85]	57.221	4.859	25.556
Criminisi *et al.* [15]	61.904	3.559	12.220

Table 5.3: Comparison of the results obtained with and without the use of inpainting algorithms.

Finally, figure 5.8 contains a comparison of the ROCs obtained without the use of any inpainting technique (continuous line) and with the use of the proposal of Criminisi *et al.* [15] (dashed line). Once again, the analysis of both curves confirms the conclusion about the useless of inpainting techniques in the filling of noisy iris information when trying to recognize noisy iris images.

After the analysis of these results, we observed that the filling of the noisy iris information through inpainting techniques is not advantageous to the iris recognition process. Almost all parameters confirmed this assumption, specially the values of the t-test, which reflect the average separability between the intra- and inter-class comparisons and tend to be less sensitive to circumstantial features of the experiments' data set. However, the less common shape of the obtained ROCs, specially the significant reduction of the space between the two curves as the values for the false acceptances decrease, should be analyzed in the future.

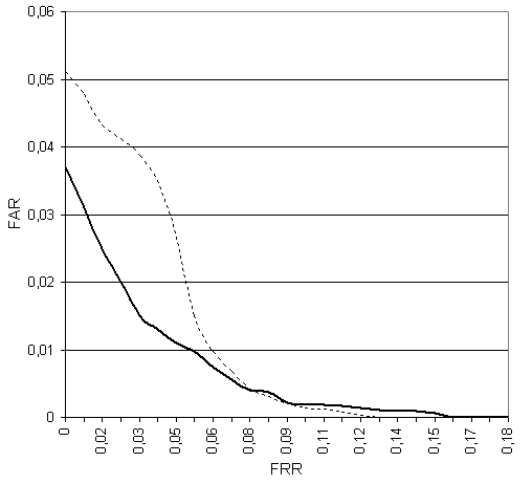

Figure 5.8: Comparison between the ROCs obtained with and without the use of the inpainting technique [15].

5.5.2 Conclusion

The results presented in the latter section allowed us to conclude that the complexity of the iris texture obstructed by noise regions can hardly be replaced through interpolation, as no significant increment in the separability between the intra- and inter-class comparisons was observed when replacing the noisy data by the interpolated (inpainted) one.

This conclusion was extremely important in the development of our work. After concludeing that the noise or missing iris information can hardly be replaced through interpolation of the noise-free data, we focused our efforts in the development of methods that deal with noise in the feature extraction and comparison stages in the attempt to achieve noisy iris recognition.

5.6 Summary

In this chapter we summarized the most common approaches for the detection and localization of noise regions within iris images. After establishing a classification for those proposals, we described a method for the local detection of noise regions in segmented and normalized iris images. This is based on the extraction of six well known statistical image features and the pixel position. We made the classification through a feed-forward neural network with one hidden layer. Experiments led us to conclude that this method has a

much better performance than the other methods for similar purposes, in spite of its higher computational requirements.

Regarding the inpainting techniques, which were tested with the goal of replacing the noisy iris data and enabling the feature extraction as if the iris data was completely noise-free, they did not proved its effectiveness, allowing us to conclude that, for this purpose, the noisy data can hardly be replaced through interpolation. This conclusion motivated the proposals described in the next chapter, which focus on the recognition of iris images where the noise regions are detected and localized.

Chapter 6

Noisy Iris Recognition

In the previous chapters we described our proposals to perform the segmentation of noisy iris images and to localize each noise region within the normalized images. The conclusion about the difficulty in replacing the noisy data through inpainting techniques, brings us to the main subject of this chapter: the biometric recognition of iris images highly affected by noise.

First, the probability of aliasing in the iris normalization stage is studied, which essentially results from highly varying image capturing distances that determine the sampling rates of the normalization process. Further, we describe our proposal for the measurement of the quality of features, used to constraint the number of features that are taken into account in the feature comparison stage. We also detail a feature selection method, that operates after the physical installation of the imaging system and, through a learning stage where typical images resultant of the imaging setting are processed, selects the higher discriminating features, according to the environment specificities. Finally, our iris classification strategy is described. It is based on the division of the normalized iris image into six regions and in the independent feature extraction and comparison for each region, avoiding that localized noisy iris regions corrupt the whole biometric signature. The classification is achieved through a fusion rule applied to the results of the dissimilarity measures.

We should stress the independence between all of the proposals described in this chapter and the feature extraction and comparison methods used for biometric recognition, which constitutes a strong point regarding their applicability to multiple iris recognition strategies.

6.1 The Aliasing Problem in the Iris Normalization Stage

The non-cooperative recognition setting is characterized by the highly dynamic and heterogeneous imaging conditions. Due to variations in the image capturing distances and in the lighting conditions that influence the pupils' size, the area of the regions correspondent to the iris will have high variance. In order to compensate this variation, common iris recognition proposals translate the segmented iris image into a double dimensionless pseudo-polar coordinate system, in a process known as the iris normalization stage. As described in section 2.2.2.2, this stage can be regarded as a sampling of the original data, with the inherent possibility of aliasing. This section is devoted to the analysis of the relation between the size of the captured iris images and the overall recognition accuracy. Our experiments allowed us to determine the value of the iris normalization sampling rate above which the recognition error rates significantly increase.

6.1.1 Iris Normalization Methods

Robust representations for pattern recognition must be invariant to changes in the size, position and patterns orientation. In the biometric compass, an iris representation invariant to changes in the distance between the eye and the capturing device, in the camera optical magnification factor and in the iris orientation, caused by torsional eye rotation and camera angles, must be accomplished. As described by Daugman [18], the invariance to all of these factors can be achieved through the translation of the captured data into a double dimensionless pseudo-polar coordinate system, which is by far the most common iris normalization method in the literature and is detailed in section 2.2.2.2.

Yuan and Shi [124] proposed a slightly different iris normalization model, which combines linear and non-linear methods to unwrap the iris region. They started by performing a non-linear transformation of all iris patterns to a reference annular zone with a predefined ratio of the radii of inner and outer boundaries of the iris. Further, this reference annular zone is linearly unwrapped to a fixed-size rectangle block for subsequence processing.

In short, both normalization processes can be regarded as point sampling operators $s(.)$ of the original image I, defined by:

$$s(I) = (I(t_1), I(t_2), \ldots, I(t_n)),\ t_i = \frac{i}{n},\ i = 1, \ldots, n \tag{6.1}$$

However, for bi-dimensional sampling of the original data, there is a probability of

aliasing and the correspondent data corruption and increase of the error rates.

6.1.2 Aliasing

Let I_1 and I_2 be two iris images similar to the *Captured Image* of figure 2.6. Also, let $A(I)$ denote the area correspondent to the iris ring in image I (*Segmented Image* of figure 2.6). In the normalization stage $s(.)$, as in any other point sampling operation, aliasing can occur in two distinct forms:

- I_1 and I_2 are very dissimilar and $s(I_1)$ and $s(I_2)$ are highly similar. In the iris biometric compass, this will increase the false acceptance rate, which is obviously the most concerning type of error regarding security.

- I_1 and I_2 are very similar and $s(I_1)$ and $s(I_2)$ are are highly dissimilar, increasing the false rejection rate, with the correspondent decrease in the users' comfort.

Commonly, the normalized iris images have fixed dimensions of 512×64 pixels (width $\times$ height), respectively in the angular and radial directions, thus $A(s(I)) = 32768$ pixels. The sampling rate r of the normalization process $s(.)$ can be given by the proportion between both of the areas:

$$r = \frac{A(s(I))}{A(I)} = \frac{32768}{A(I)} \tag{6.2}$$

where I is the captured iris image. In the following experiments, we varied the size of the captured iris image $(A(I))$ and analyzed its influence in the accuracy of a common iris recognition proposal. It will be shown that when $r > 4$, a strong increase of the recognition error rates is observed, as a result of the aliasing occurred in the iris normalization stage.

Figure 6.1 illustrates the problem that we analyze in the following experiments. Here, the capturing of an iris image with different dimensions and the correspondent normalization to fixed dimensions of 512×64 pixels is simulated. As can be seen, although the situation is magnified for the purpose of illustration, the differences in the normalized images are notorious, which increases the false rejections in the recognition task.

6.1.3 Experiments and Discussion

In the experiments we implemented the method described by Daugman [18], which is composed by the four main stages detailed in section 2.2.3.1: iris segmentation, normal-

Figure 6.1: Example of the potential problems associated with the iris normalization, starting from varying sizes of the captured iris images.

ization, feature extraction and comparison. According to the author, the segmentation was accomplished through the integro-differential operator that searches for both iris borders. Feature extraction was performed through the use of two dimensional Gabor filters, followed by a binarization process. Finally, feature comparison was made through the Hamming distance.

6.1.3.1 Data Sets

The experiments described in this section are slightly different from others in this thesis. More important than the noise factors that each database contains was the evaluation of the recognition accuracy as function of the iris dimensions in the captured images. Due to this, we chosen two data sets from the databases with most opposite characteristics: $UBIRIS$ and $UPOL$, respectively the noisiest and the completely noise-free ones. This enabled the main purpose of the experiments, as well as the analysis of the recognition's accuracy, when simulating the image capturing with ($UPOL$) and without ($UBIRIS$) the users' cooperation.

The used data sets - $UBIRIS_{ali}$ and $UPOL_{ali}$ - have respectively 130 and 132 images of the $UBIRIS$ and $UPOL$ databases belonging to 13 and 44 subjects, for a total of respectively 585 and 7800 and 132 and 8514 intra- and inter-class comparisons.

Table 6.1 contains statistics of the data sets. The first column identifies the data set, the second specifies the initial dimensions of the images. The third and forth column contain, respectively, the average pupil and iris radius. Finally, the fifth and sixth columns correspond to the average area of the iris ring and the average sampling rate (6.2) of the

Data set	Image size, pix	Pupil radius, pix	Iris radius, pix	Iris area, pix	Sampling rate
$UBIRIS_{ali}$	800×600	51	185	99347	0.3298
$UPOL_{ali}$	768×576	69	271	215758	0.1518

Table 6.1: Average areas of the regions correspondent to the iris ring in the data sets images and average sampling rates of the iris normalization processes.

normalization processes, through the *Daugman rubber sheet* model. Although smaller than the initial images of $UBIRIS_{ali}$, the regions corresponding to the iris in the $UPOL_{ali}$ data set images are much larger, corresponding to larger iris areas and smaller sampling rates.

In order to avoid that segmentation errors corrupt the results, we manually verified that the iris segmentation algorithm performed accurately in all images of both data sets. The simulation of the varying dimensions of the captured iris images was accomplished through bi-cubic resizing. Each image was resized from 100% to 10% of its original dimensions, described in table 6.1.

6.1.3.2 Results

According to (6.2), figure 6.2 contains the relation between the average sampling rates of the normalization processes and the dimensions of the captured iris images, respectively in the $UBIRIS_{ali}$ (figure 6.2a) and $UPOL_{ali}$ (figure 6.2) data sets. The horizontal axis specify the size of the captured iris images in proportion with the images' dimensions described in table 6.1 (values are percent). The vertical axis contain the average sampling rate (6.2) of the normalization processes of these images. A shape similar to an exponential function can be observed, which means that a small decrease in the images dimensions imply an high grow in the sampling rates of the normalization process. The vertical lines identify the value for the dimensions of the images above which the error rates observed in the following experiments significantly increased.

Figure 6.3 contains four measures of the recognition's accuracy. The solid lines illustrate the results obtained in the $UBIRIS_{ali}$ data set and the dashed lines those obtained in the $UPOL_{ali}$ data set. Again, the horizontal axis denote the dimension of the used images, in proportion (percentage) with the ones described in table 6.1. The vertical lines correspond to the identified threshold of 30%, from which the error rates significantly increase. Figure 6.3a contains the values for a t-test given by (5.1), figure 6.3b the approximated equal error rates, figure 6.3c the percent values of the areas under the ROCs and, finally, figure 6.3d

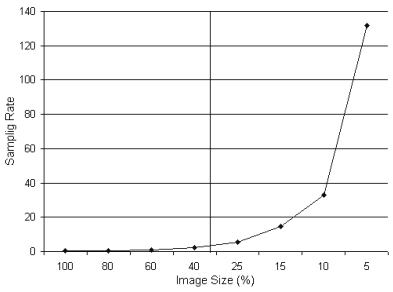

(a) Average sampling rate (r) from the images of $UBIRIS$ data set.

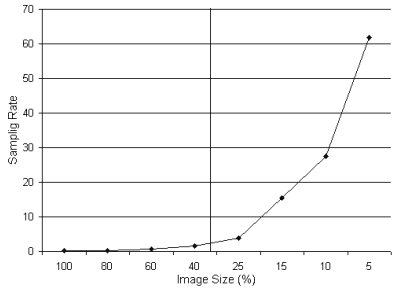

(b) Average sampling rate (r) from the images of $UPOL$ data set.

Figure 6.2: Average sampling rate (r) of the normalization process.

contains the values of the false rejections when the false acceptances were minimized.

It can be observed in figure 6.3a that the separability between the intra- and inter-class comparisons, given by (5.1), remained with similar values until the area correspondent to the iris in the captured image is below 50% of the dimensions described in table 6.1, either in the $UBIRIS_{ali}$ and in the $UPOL_{ali}$ data sets. However, when the area of the captured image is below 30% of the initial dimensions, there is a significant decrease in the separability between the intra- and inter-class comparisons, corresponding to sampling rates (6.2) higher than 5. Above this value, we observed a significant increment of the error rates, specially the false rejections (figure 6.3d), which led us to assume the occurrence of aliasing in the iris normalization stage. Moreover, this degradation in the results was observed either in the noisy and in the noise-free data sets, indicating that this problem has similar impact in both cooperative and non-cooperative image capturing settings.

6.1.4 Conclusion

We analyzed the influence that the sampling rate used in the iris normalization stage has in the overall accuracy of a common iris recognition proposal.

We observed no significant degradation in the accuracy when the sampling rates are lower than 5. For higher sampling rates (correspondent to original images with iris area less than 30% of the normalized one), the error rates significantly increased, which indicates a strong probability of the occurrence of aliasing. This increase of the error rates, specially the false rejections, requires the development of alternate sampling/normalization processes, more tolerant to variations in the dimension of the original data. Moreover, we stress that the

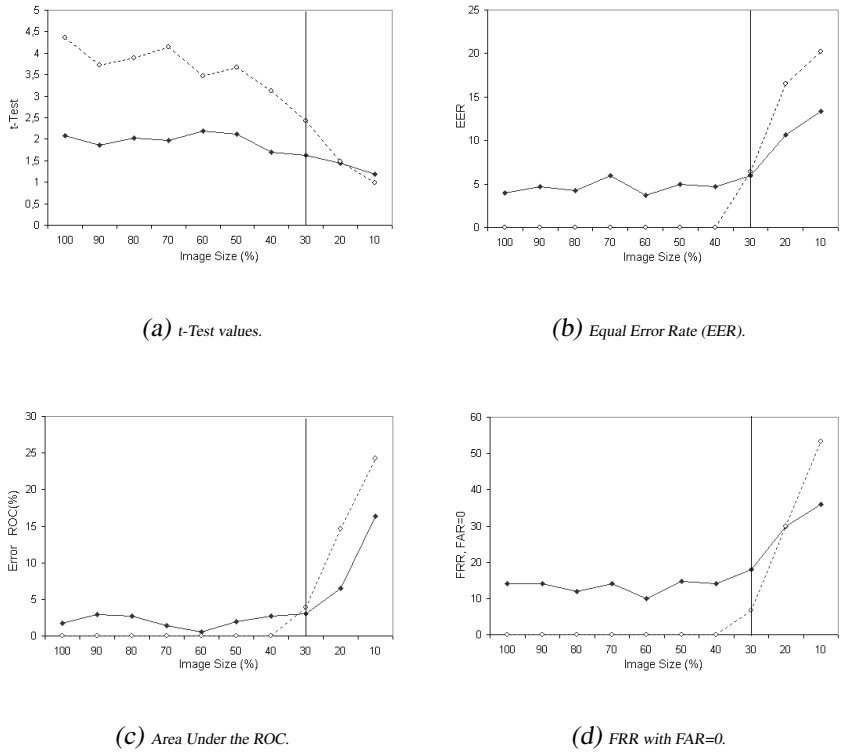

(a) *t-Test values.*

(b) *Equal Error Rate (EER).*

(c) *Area Under the ROC.*

(d) *FRR with FAR=0.*

Figure 6.3: Recognition's accuracy regarding the size of the images used in the segmentation algorithm.

observed deterioration in the recognition's accuracy is independent of the amount of noise that the iris regions contain, since the values obtained for the minimum acceptable sampling rates in the $UBIRIS_{ali}$ (noisy images) and in the $UPOL_{ali}$ (noise-free images) data sets were approximately equal.

6.2 Proposed Feature Quality Measure and Comparison Method

As mentioned above, several proposals were made to access iris images quality and to localize noise regions within the captured irises. In this section we propose a method that measures the quality of each feature of the biometric signature and takes into account this information to limit the comparable features in the computation of the similarity between iris signatures. This measure is based on the proportion of noise pixels used in the extraction of each feature and its main purpose is to avoid that features predominantly extracted from

noise regions corrupt the biometric signatures. Experiments led us to conclude that this method significantly decreases the error rates in the recognition of noisy iris images, which makes it adequate for the non-cooperative setting.

6.2.1 Feature Quality

Our noise detection proposal, similarly to other local methods described in section 5.3, produces binary maps correspondent to the segmented and normalized iris images. Here, the noise regions are represented through the black areas and the noise-free regions through white ones, as exemplified by figure 6.4. As can be seen, there is a discrimination between the unobstructed iris areas and the regions correspondent to types of information other than the iris.

(a) *Segmented and normalized iris image, with significant noise regions correspondent to eyelids (1) and eyelashes (2) obstructions and reflections (3).*

(b) *Detection of the noise regions of the image 6.4a.*

Figure 6.4: Normalized noisy iris image and its correspondent binary noise map.

Our purpose is to produce a quality value - in the [0,1] interval - for each of the extracted features. This value should reflect the proportion of noise pixels used in the computation of the respective feature and will be helpful in the feature comparison, in order to avoid the comparison of the noisiest features or assigning them a small comparison weight. As described in the next section, this proposal is independent of the feature extraction method used.

Its rationale is straightforward: at a coarse level, every extracted feature can be regarded as a function of k image pixels (the original data). Thus, the proportion between the noise and noise-free pixels used in the extraction of each feature provides a value between 0 and 1 that can be computed together with any feature extraction strategy.

Let I be the segmented and normalized iris image and $(x, y) \in \mathbb{N}^2$ be the coordinates of an image pixel. Let $n((x, y)) : \mathbb{N}^2 \rightarrow \{0, 1\}$ be the function that performs the binary classification (noise or noise-free) for every pixel (x, y) of the image I:

$$n((x,y)) = \begin{cases} 0 & , I(x,y) \text{ is noise} \\ 1 & , \text{otherwise} \end{cases} \tag{6.3}$$

Let $\mathbb{F} = \{f_1, \ldots, f_k\}$ be the set of features extracted from the image I. Independently of the feature extraction strategy, every f_i is obtained having as basis N_i pixels of I. Let $\mathbb{P}_i = \{(x_{i_j}, y_{i_j})\}\ j = 1, \ldots, N_i$ be the set of pixels' coordinates used in the extraction of the feature f_i. We define the function $q(\mathbb{P}_i) : (\mathbb{N}_1^2 \times \ldots \times \mathbb{N}_N^2) \rightarrow [0, 1]$ that gives the quality of the feature f_i:

$$q(\mathbb{P}_i) = \frac{1}{N_i} \sum_{i=1}^{N_i} n(I(x_i, y_i)) \tag{6.4}$$

This function $q(.)$ gives the proportion of noisy data considered in the extraction of f_i. Through it, every extracted feature has a correspondent quality value, which is inverse to the proportion of noisy pixels evolved in the creation of f_i. Thus, for completely *noisy* (poorest quality) and *noise-free* (optimal quality) features, the quality value will be respectively equal to 0 and 1.

6.2.2 Feature Comparison

In the following discussion we will use a superscript to distinguish between two different feature sets, such as, $\mathbb{F}^1$ and $\mathbb{F}^2$, and a subscript to distinguish between different features of a feature set, such as, f_1^1 and f_2^1.

The purpose of the feature comparison stage is to obtain a similarity value between two feature sets (biometric signatures) - $\mathbb{F}^i$ and $\mathbb{F}^j$ - and enable a conclusion about the identity of the subjects from which the features were extracted. Next, we describe the two tested variants for the feature comparison stage: *hard* and *fuzzy*.

Regarding the *hard* feature comparison, features are considered for comparison only if their quality value is higher than a threshold. Oppositely, in the *fuzzy* variant the comparison is allowed for all features independently of their quality value and the result is weighted by the average quality of the operands features.

Formally, let $\mathbb{Q}^0$ and $\mathbb{Q}^1$ be two features sets with the respective quality values for each feature: $\mathbb{Q}^j = \{(f_1^j, q(f_1^j)), \ldots, (f_n^j, q(f_n^j))\}$. The feature comparison function is given by:

$$fc(\mathbb{Q}^0, \mathbb{Q}^1) = \frac{\sum_{i=1}^{n} dist(f_i^0, q(f_i^0), f_i^1, q(f_i^1))}{\sum_{i=1}^{n} cnt(f_i^0, q(f_i^0), f_i^1, q(f_i^0))} \tag{6.5}$$

In the *hard* comparison variant, $dist(.)$ and $cnt(.)$ are functions that give respectively the similarity between two features and the information about the features' comparability. They are defined as:

$$dist_{hard}(f_i^0, q(f_i^0), f_i^1, q(f_i^1)) = \begin{cases} d(f_i^0, f_i^1) & , \ q(f_i^0) \geq T \ \wedge \ q(f_i^1) \geq T \\ 0 & , \text{ otherwise} \end{cases} \tag{6.6}$$

$$cnt_{hard}(f_i^0, q(f_i^0), f_i^1, q(f_i^1)) = \begin{cases} 1 & , \ q(f_i^0) \geq T \ \wedge \ q(f_i^1) \geq T \\ 0 & , \text{ otherwise} \end{cases} \tag{6.7}$$

where $d(.)$ is the function that gives the distance between features (e.g., Hamming or Euclidean distance) and T is a threshold value closed in the [0,1] interval that represents the minimum quality value.

Regarding the *fuzzy* comparison variant, all the features are considered for comparison and weighted according to their respective quality value. In this context, $dist(.)$ and $cnt(.)$ are given by:

$$dist_{fuzzy}(f_i^0, q(f_i^0), f_i^1, q(f_i^1)) = d(f_i^0, f_i^1) \frac{q(f_i^0) + q(f_i^1)}{2} \tag{6.8}$$

$$cnt_{fuzzy}(f_i^0, q(f_i^0), f_i^1, q(f_i^1)) = \frac{q(f_i^0) + q(f_i^1)}{2} \tag{6.9}$$

where, as above, $d(.)$ is the function that gives the distance between features.

6.2.3 Experiments and Discussion

Due to its relevance in the iris recognition literature, in the experiments we implemented the method proposed by Daugman [18], described in section 2.2.3.1. However, we stress that the proposed method is independent of the feature extraction and comparison strategies.

We compared the results obtained when following the method exactly as described by the author (using all the features in the feature comparison stage) and our proposed feature

quality measure to constraint the comparable features in the computation of the similarity between biometric signatures (feature comparison).

6.2.3.1 Data Sets

Since this type of experiment requires the highest quantities of noise in the iris images, we selected 260 images from the $UBIRIS$ database, belonging to 26 different subjects, enabling respectively a total of 1170 and 32500 intra- and inter-class comparisons. Further, we divided the selected images into two sub sets, according to the respective quantity of noise. The 130 less noisy images were included in the $UBIRIS_{qua1}$ data set and the 130 noisier ones in the $UBIRIS_{qua2}$ data set. This enabled us to conclude about the variations in the recognition accuracy as the amount of image noise varies. As in the other experiments described in this thesis, the characteristics of the data sets are detailed in appendix B.

6.2.3.2 Results

As stated above, we compared the accuracy of the classical Daugman iris recognition method as described by the author and with our proposals, in the $UBIRIS_{qua1}$ and $UBIRIS_{qua2}$ data sets. We made the feature extraction on every image and compared the resultant biometric signature with the remaining ones of the same data set.

Figure 6.5 contains four measures that reflect the advantages of using our proposal together with the classical Daugman feature extraction and comparison methods. The horizontal axis represents the threshold T (minimum feature quality value), using the *hard* comparison variant. The traditional approach of comparing all the features is equivalent to our proposal with minimum quality value equal to 0. The continuous line is relative to the $UBIRIS_{qua2}$ data set and the dashed line to the less noisier $UBIRIS_{qua1}$ one. Figure 6.5a contains the obtained values for a t-test given by (5.1) and figure 6.5b contains the equal error rates, obtained when the false accepts and rejects were approximately equal. Figure 6.5c contains the percent values of the area under the ROCs and, finally, figure 6.5d the obtained false rejections, when the false acceptances were minimized.

The best results were observed when the comparison between features is constrained to those that have quality value higher than 0.5. In this situation, while maintaining a large number of comparable features, features with very poor quality, extracted from a majority of noisy pixels, are not taken into account in the comparison and, thus, do not corrupt the final results. Our experiments clearly showed an improvement in the recognition accuracy,

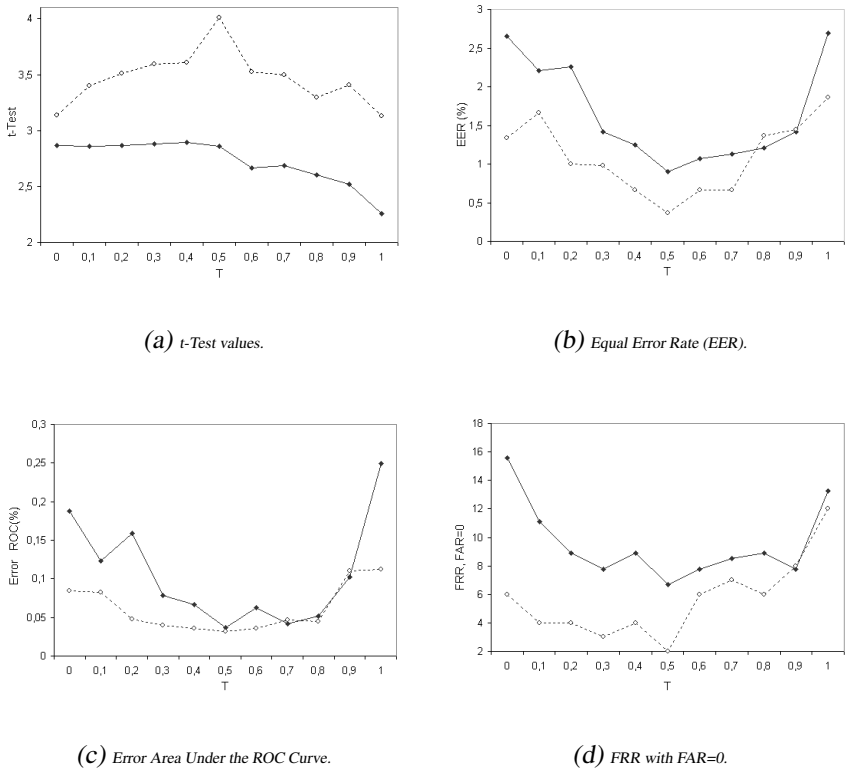

(a) *t-Test values.*

(b) *Equal Error Rate (EER).*

(c) *Error Area Under the ROC Curve.*

(d) *FRR with FAR=0.*

Figure 6.5: Results obtained from our feature quality measuring and comparison proposals in the $UBIRIS_{qua2}$ (continuous line) and $UBIRIS_{qua1}$ (dashed line).

simultaneously reducing the error rates and the area under the ROCs and increasing the separability between the intra- and inter-class comparisons.

Table 6.2 contains the obtained results, when varying the feature comparison strategy. The first column identifies the classification method. The second (τ) contains the values for the t-test given by (5.1), the third contains the approximated equal error rates, the forth contains the percentage of the area under the ROC and, lastly, the fifth column corresponds to the false rejection rates when the false acceptances were minimized. All the error values are expressed for a confidence interval of 95%. The analysis of these results clearly shows an increment of system's overall accuracy using our *hard* variant proposal, specially in the noisier $UBIRIS_{qua2}$ data set. Regarding the less-noisy $UBIRIS_{qua1}$ data set, the advantages resultant of the use of our proposal were also clearly visible. This means that even in images with insignificant portions of noise our proposal can slightly improve the recognition's accuracy.

Surprisingly, the *fuzzy* feature comparison variant achieved worst results than the *hard*

Method	τ	EER, %	Error ROC, %	FRR, FAR=0, %
UBIRIS$_{\mathbf{qua1}}$ data set				
Original	3.130	2.690 ± 0.004	0.112	12.778 ± 0.009
Proposed (hard), T=0.5	4.012	0.366 ± 0.001	0.032	2.667 ± 0.004
Proposed (fuzzy)	3.813	0.900 ± 0.002	0.058	6.166 ± 0.006
UBIRIS$_{\mathbf{qua2}}$ data set				
Original	2.258	2.090 ± 0.004	0.449	15.556 ± 0.010
Proposed (hard), T=0.5	2.892	0.904 ± 0.002	0.036	6.667 ± 0.007
Proposed (fuzzy)	2.699	1.130 ± 0.002	0.057	11.639 ± 0.009

Table 6.2: Comparison between the results obtained by the Daugman recognition method exactly as described by the author and together with our feature quality measure and comparison constraint proposals.

one. Although it is intuitively more advantageous, we observed that the comparison between all the features, even if it is weighted by the respective quality value, did not represent a valid alternative. However, it is our purpose to validate this conclusion in the near future through experiments with different data sets.

6.2.4 Conclusion

In the previous sections we described and experimentally tested a method for the measurement of each feature quality. Once again, the main motivation was the significant increment of the error rates observed when the recognition systems deals with noisy images.

The quality value is used to constraint the number of features that are taken into account in the feature comparison stage. Experiments led us to conclude that our proposal significantly decreases the error rates in the recognition of noisy iris images, thus being appropriate for the application in a non-cooperative setting, where the ability to deal with noisy images is required.

Even in images with small portions of noise, the results showed that our proposal contributes for the increase of the separability between the intra- and inter-class comparisons, with the correspondent improvements in the recognition's accuracy. Moreover, the independency between our proposal and the chosen feature extraction and comparison methods is stressed and regarded as a strong point, enabling its use together with multiple iris recogni-

tion strategies.

6.3 Proposed Feature Selection Method

The non-cooperative image capturing setting, either under natural luminosity or varying lighting conditions leads to the appearance of images whose typical characteristics are determined by the used optic device and the environment itself. For instance, it is expectable that some imaging conditions propitiate the existence of reflections (specular or lighting) in specific iris regions, while others propitiate the iris occlusion by eyelids and eyelashes.

Current iris matching proposals (feature extraction and comparison) are independent of the imaging environments and do not take into account this information in the recognition task. In this section we propose a feature selection method that operates after the physical installation of the image capturing framework. First, a training set of iris images is captured, which should reflect the typical characteristics of the images captured in such environment, namely their predominantly noisy iris regions. Further, the candidate features are extracted from each image and their values used in the computation of the merit of each candidate feature. This allows the selection of the higher discriminating features, according to each environment and its lighting conditions. Experiments show a substantial increase in the separability between the intra- and inter-class comparisons when the 30% highest discriminating features are selected, leading to a substantial decrease of the error rates in the recognition of noisy iris images.

6.3.1 Feature Selection

The problem of feature selection is to take a set of candidate features and select a subset that best performs under some classification system [129]. This procedure can reduce the cost associated with classification, by reducing the number of features that must be collected, and in some cases it also provides better results due to the finite sample size effects: as the number of features is reduced, and the number of points is maintained, the feature space becomes more densely populated.

Formally, let T and S be respectively the candidate and selected feature sets, $S \subseteq T$. Also, let $\|.\|$ denote the cardinality of the set, such that $\|T\| = t$ and $\|S\| = s$. The feature selection criterium function for the set X is represented by $J(X)$. Considering that higher values of J indicate better feature sets, the problem of feature selection is to find a subset

$S \subseteq T$ such that $|S| = s$ and:

$$J(S) = max_{X \subseteq T, |X|=s} J(X) \tag{6.10}$$

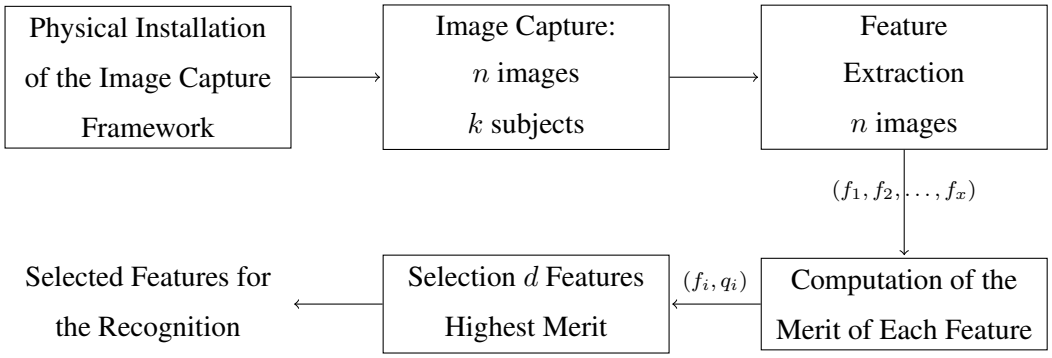

Figure 6.6: Block diagram of the proposed feature selection method.

According to this definition, the block diagram of the proposed feature selection method is given in figure 6.6. After the physical installation of the image capturing framework, n images from the irises of k subjects are collected, which should represent the typical characteristics and noise regions of the images captured within the environment. Further, the candidate features are extracted for all these images and their values used in the computation of the features' merit (6.11). Finally, the s features with highest merit are selected.

The motivation behind this proposal is the valorization of the features which respectively maximize and minimize the signatures dissimilarity in the inter- and intra-class comparisons. As can be seen in (6.11), the dissimilarity between two feature values contributes to an increase of the respective merit if they were extracted from different irises and, inversely, contributes to its decrease if the features were extracted from images of the same iris.

In the following discussion we will use F_i^p to denote the i^{th} feature set extracted from the iris p and $f_{i,j}^p$ to denote the j^{th} feature of the i^{th} feature set extracted from the iris p. Thus, $F_i^p = \{f_{i,1}^p, \ldots, f_{i,t}^p\}$. Let $\mathbb{A} = \{F_1^{p_1}, \ldots, F_n^{p_k}\}$ be the set of training feature sets extracted from n images of k subjects. The merit value $m(.)$ of each candidate feature i is given by: $m(i) : \{1, \ldots, t\} \rightarrow \mathbb{R}$:

$$m(i) = \sum_{j=1}^{n-1} \sum_{k=j+1}^{n} \frac{d(f_{j,i}^p, f_{k,i}^r)}{(t_I - t_E)\, \delta_{p,r} + t_E} \, (1 - 2\, \delta_{p,r}) \tag{6.11}$$

where $d(.)$ is the function that gives the features dissimilarity (e.g., Hamming or Euclidean distance), $\delta_{p,r}$ is the Kronecker delta and t_I and t_E are, respectively, the number of intra- and inter-class comparisons between elements of $\mathbb{A}$. This definition implies that the highest values occur when the features dissimilarity is respectively smaller in the intra- and higher in the inter-class comparisons, obtaining a value that is directly correspondent to the feature discriminant capacity within the respective imaging environment.

According to (6.10), the function $J(.)$ that performs the feature selection will give us the feature set S, which contains the s features with highest values of $q(.)$.

However, if the features are selected as above described, it is not possible to achieve invariance to iris rotation through signature shifting, and this is a very common technique used in the feature comparison. We compensate this by making the normalization process into the dimensionless polar coordinate system starting from 5 different deviation angles of the segmented iris image (-10º, -5º, 0º, +5º, +10º) and obtaining 5 normalized iris images. The subsequent processing is further made separately for each of these images and the dissimilarity between iris signatures is given by the lowest dissimilarity between the enrolled signature and those extracted from each of these images.

6.3.2 Algorithm

Algorithm 1 contains the pseudo-code of the above described feature selection method. Its computational complexity of $O(n^3)$ is not a concern, as it will be executed before the functioning stage of the recognition system and, due to this fact, without critical time constraints. In this algorithm $f(i, j)$ represents the i^{th} feature extracted from the image j and $id(f)$ the identity of the subject from where the feature f was extracted.

6.3.3 Experiments and Discussion

In these experiments we implemented a recognition method based in the proposal of Daugman [18], with exception of the feature extraction stage, that was accomplished through the Haar dyadic wavelet decomposition instead through a bank of 2D Gabor wavelets. We found that, apart of obtain similar results, the purpose of illustration of the results through the association between each feature and a correspondent image region justified this option. However, we stress that we experimentally observed that the advantages resultant of the application of our proposal together with the Daugman's recognition method were similar

Algorithm 1 Feature Selection Algorithm

```
t ← Number of feature sets in the training set
n ← Number of candidate features
d ← Number of features to be selected
t_I ← Number of intra-class comparisons between elements of T
t_E ← Number of inter-class comparisons between elements of T
for i = 1 to n do
   merit(i) ← 0
end for
for i = 1 to t − 1 do
   for j = i + 1 to t do
      for k = 1 to n do
         x ← dist(f(k,i), f(k,j))
         if id(f(k,i)) == id(f(k,j)) then
            merit(k) ← merit(k) - x / t_I
         else
            merit(k) ← merit(k) + x / t_E
         end if
      end for
   end for
end for
S=Select_s_Features_Highest_Merit(n,s,merit)
return(S)
```

to the ones reflected in the experiments that we describe in the following.

We compared the results when following the classical approach of computing the dissimilarity between biometric signatures through the comparison between the 2048 extracted features and the proposed feature selection method, when selecting different feature sub sets, according to the specific characteristics of the training set images and their predominant noise regions.

6.3.3.1 Data Sets

In order to conclude about the benefits of our proposal either in the cooperative and non-cooperative image capturing settings, we chose $UBIRIS$, $CASIA$ and $UPOL$ databases

for the experiments, enabling the analysis both in highly ($UBIRIS$), less noisy ($CASIA$) and noise-free environments ($UPOL$). We selected 400 images from $UBIRIS$ and $CASIA$ databases, belonging to 40 different subjects, enabling respectively 1800 and 87000 intra- and inter-class comparisons. Due to constrains on the number of available images per subject, from the $UPOL$ database 132 images belonging to 44 subjects were selected, for a total of 132 intra- and 8514 inter-class comparisons. Further, we divided each of the data sets into two sub sets. The first ones - $UBIRIS_{fs1}$, $CASIA_{fs1}$ and $UPOL_{fs1}$ - were used as training sets in the computation of features quality and in the feature selection The latter - $UBIRIS_{fs2}$, $CASIA_{fs2}$ and $UPOL_{fs2}$ - in the evaluation of the recognition accuracy. Additional image characteristics can be found in appendix B.

As illustrated by figure 6.7, the selected images from the $UBIRIS$ database contain severe iris obstructions by eyelids and eyelashes in the lower and upper regions of the iris (regions 1) and specular and lighting reflections predominantly in the left and right regions (regions 2). Images from the $CASIA$ database typically contain iris obstructions by eyelids and eyelashes in the vertical iris extremes (regions 1) and those from the UPOL database are completely noise free.

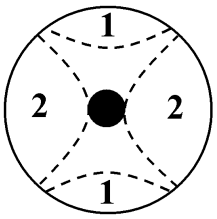

(a) *Typical noise regions in the tested iris images.*

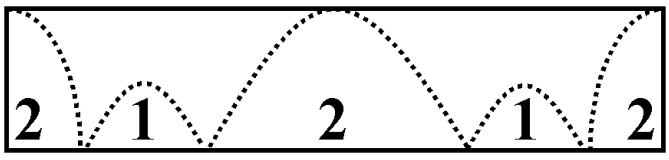

(b) *Correspondent noise regions in the segmented and normalized iris images.*

Figure 6.7: Predominant noise regions of the used data sets in the captured (figure 6.7a) and normalized (figure 6.7b) iris images.

6.3.3.2 Results

According to the process described in section 6.3.1, we performed the feature extraction in the training set images and obtained 2048 features for each image. Further, through (6.11), we computed the merit $m(.)$ of each candidate feature. With the purpose of illustration, figure 6.8 contains a representation of the quality of the candidate features extracted from the 3^{rd} octaves dyadic wavelet decomposition, when used respectively the $UPOL_{fs1}$ (figure 6.8a), $CASIA_{fs1}$ (figure 6.8b) and $UBIRIS_{fs1}$ (figure 6.8c) as training data sets. The chosen feature extraction strategy, similarly to other common approaches, allows a simultaneous scale-space data representation and, thus, feature values have direct correspondence with a spacial image region. In all of the sub-figures, each pixel's intensity $I(p)$ is given by:

$$I(p) = \frac{m(p) - min_q}{max_q - min_q} * 255 \tag{6.12}$$

where $m(p)$ is the feature merit correspondent to the pixel p and min_q and max_q are respectively the minimum and maximum values of the features quality.

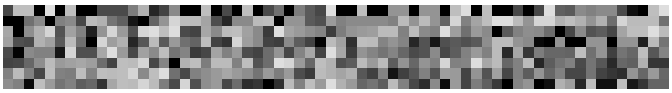

(a) Merit value of the candidate features from the $UPOL_{fs1}$ data set.

(b) Merit value of the candidate features from the $CASIA_{fs1}$ data set.

(c) Merit value of the candidate features from the $UBIRIS_{fs1}$ data set.

Figure 6.8: Merit value (6.11) of the 3^{rd} octave dyadic wavelet decomposition candidate features extracted from the training data sets.

It is evident that figure 6.8a is brighter and its intensity values are more homogeneous. Since it corresponds to features that were extracted from the noise-free database, it indicates that within noise-free environments all the candidate features have similar discriminating capacity. Oppositely, the pixels intensity of figures 6.8b and 6.8c are more heterogeneous. Moreover, several dark regions can be observed, corresponding to features that were extracted from the typically noise regions of the training set images (figure 6.7).

To obtain an objective measure of the features' merit and homogeneity, we computed the mean (μ) and standard deviation (σ) of the pixels intensity in each of the figures. The obtained values were $(\mu, \sigma) =$ (111.5, 64.3), (75.25, 70.8) and (61.9, 77.1) respectively in figures 6.8a, 6.8b and 6.8c. As expected, features from the noisiest data sets have lowest quality and higher heterogeneity, confirming the hypothesis that motivated this proposal: the feature selection assumes higher relevance in the recognition of noisy iris images, resultant from the capturing in less constrained imaging environments.

Hereinafter, the goal was to obtain an approximation of the optimal number of features that must be selected for comparison. With this purpose, we started from the original feature set - composed by 2048 components - and reduced the number of selected features between 90% and 10% of the initial cardinality. Again, $UPOL_{fs1}$, $CASIA_{fs1}$ and $UBIRIS_{fs1}$ were used to perform the feature selection and $UPOL_{fs2}$, $CASIA_{fs2}$ and $UBIRIS_{fs2}$ to evaluate the error rates. Figure 6.9 contains the results. The horizontal axis values represent the number of selected features, in proportion with the original set of 2048 candidate features. Thus, the classical feature comparison approach is equivalent to the results obtained with 100% of selected features. Figure 6.9a contains the values for the t-test given by (5.1). Figures 6.9b and 6.9c contain the approximated equal error rates and the area of the regions under the ROCs. Finally, figure 6.9d contains the false rejection rates when the false acceptances were minimized. The continuous, dashed and doted lines represent the results obtained respectively in the $UBIRIS_{fs2}$, $CASIA_{fs2}$ and $UPOL_{fs2}$ data sets.

It is evident that, for all the data sets, the best results were obtained when a smaller number were selected to comparison. Even in the noise-free $UPOL_{fs2}$ data set, the highest accuracy was observed when 20 to 60% of the candidate features were selected. Within this interval, the recognition algorithm presented error rates equal to 0.

Regarding the $UBIRIS_{fs2}$ data set, the best values were observed when 30% of the candidate features were selected, which gives a total of 614 features. In this case the EER value was about 6%, although in highly noisy images. We remark that the original method, comparing the 2048 features, obtained an EER above 12%, which is a very significant

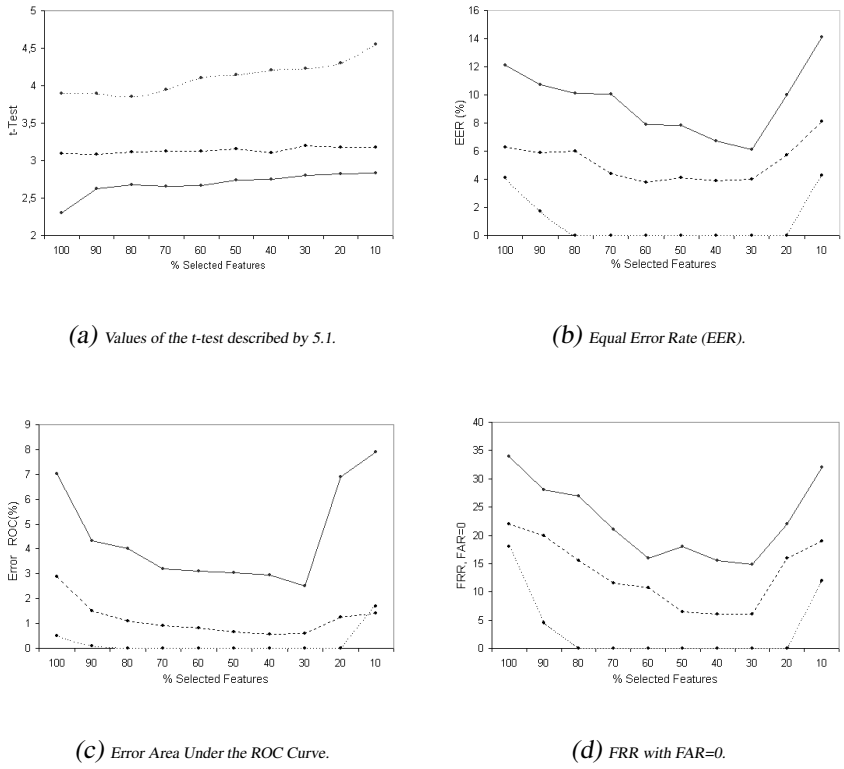

(a) Values of the t-test described by 5.1.

(b) Equal Error Rate (EER).

(c) Error Area Under the ROC Curve.

(d) FRR with FAR=0.

Figure 6.9: Results obtained by our feature selection proposal.

decrement (around 50%) of the error rates.

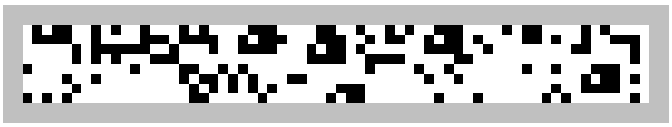

(a) Best features according to the $CASIA_{fs1}$ data set.

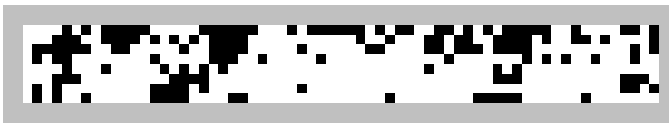

(b) Best features according to the $UBIRIS_{fs1}$ data set.

Figure 6.10: Features with highest merit $m(.)$ (signalled by the dark pixels), computed in the $UBIRIS_{fs1}$ and $CASIA_{fs1}$ data sets.

Figure 6.10 illustrates the 30% features with highest quality values $q(.)$ that were for

this reason selected for the feature comparison. The black pixels of figures 6.10a and 6.10b correspond respectively to the best features obtained from the $CASIA_{fs1}$ and $UBIRIS_{fs1}$ data sets. Not surprisingly, it is curious to observe the small number of features selected from the typical noisy iris regions of both data sets (figure 6.7).

In order to validate the advantages resultant of our proposal, we compared the ROCs obtained by the classical feature comparison strategy and our proposal, when selecting for comparison exclusively 30% of the candidate features with highest merit. Figure 6.11 contains the results. The continuous and dashed lines respectively represent the results obtained by our proposal and the classical strategy and are relative to the $CASIA_{fs2}$ (figure 6.11a) and $UBIRIS_{fs2}$ (figure 6.11b) data sets, which best enhance our proposal's advantages for the purposes of illustration.

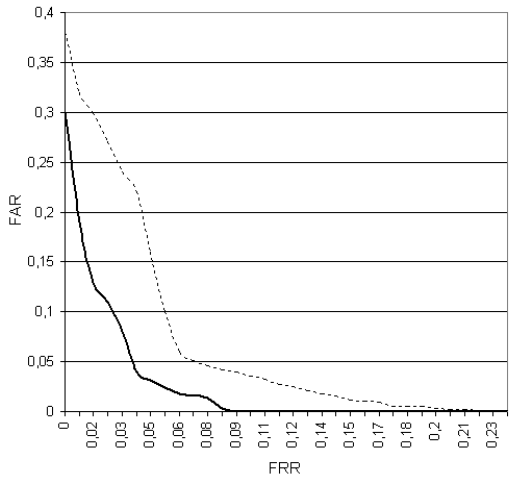

(a) Receiver operating curves obtained in the $CASIA_{fs2}$ data set.

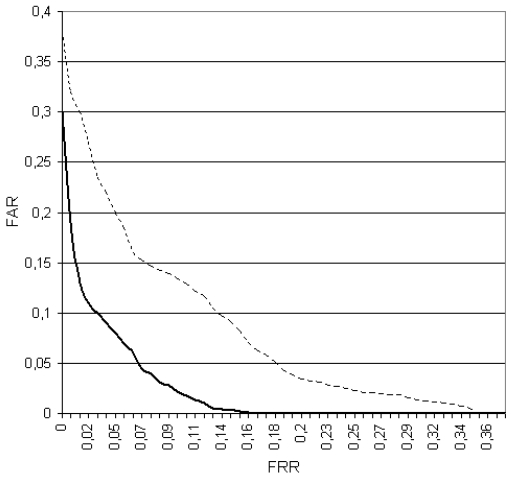

(b) Receiver operating curves obtained in the $UBIRIS_{fs2}$ data set.

Figure 6.11: Comparison between the receiver operating curves (ROC) obtained by the classical Daugman recognition method (dashed lines) and our feature selection proposal (continuous lines) when selecting 30% of the features with highest merit values (6.11).

This can be explained by the selection of features that were extracted from typically noise-free regions and have, for this reason, higher discriminating capacity. As the images of the test data set have similar characteristics to the training set ones, these features tend to increase the classes separability and significantly improve the recognition accuracy. Of course, part of the improvement is certainly related to the fact that a reduction in the dimensionality of the feature space occurred with the feature selection process.

All these experiments led us to conclude that the proposed procedure increases the adaptability of the recognition system to the typical noise regions of the captured images, through the selection of the best features, according to the typical image characteristics.

6.3.4 Conclusion

The typical noise regions and characteristics of the images captured within non-cooperative environments are highly influenced by the used optic device and the specific lighting conditions of each environment. This leads to a significant increment of the error rates, which was the main motivation for this section proposal.

We described a method for the feature selection that takes into account the typical characteristics of the images, namely their predominant noise regions determined by the imaging environment. Using a training set composed of images captured after the physical installation of the imaging system, we computed the merit value for each candidate feature and selected those with highest values.

Since the training set images are representative of the ones that the recognition system will have to deal with, this process contributes for the adaptability of the recognition system to the specific environment.

We stress that this approach is compatible with different imaging environments, since each recognition system will select a proper sub set of features that are further taken into account in the recognition process, through the comparison with the correspondent enrolled features.

Experiments led us to conclude about an improvement in the system's accuracy when the cardinality of the selected feature set is between 30 and 50% of the number of candidate features. In this situation, the error rates significantly decreased (about 50%) in the recognition of noisy iris images, which must be considered an achievement.

However, one concern may be the way we dealt with rotational invariance, since the common signature shifting does not work with the proposed feature selection method. The iris normalization started from 5 deviation angles and replication of the process for each of the resultant images significantly incremented the computational cost.

6.4 Proposed Iris Classification Strategy

Assuming that, in spite of being noisy, the iris image has been accurately segmented, in this section our aim consists in the proposal of a classification strategy more robust to noise factors. We observed that, in most cases, the noise is localized in some subpart of the iris. Our method is based on the division of the segmented iris into six regions, followed by the independent feature extraction on each one. Further, through the feature comparison between signatures extracted from correspondent regions, six dissimilarities are obtained and fused according to a classification rule. The hope is that most of the iris regions are noise-free and that accurate recognition can be achieved, even in highly noisy images. As our experiments confirm, the proposed classification method decreases the false rejection rates more than 40%, which is obviously an achievement towards the non-cooperative iris recognition.

Based on this, in the following sub-sections we describe the proposed iris partition, feature extraction and classification strategies.

6.4.1 Iris Division and Feature Extraction

As illustrated by figure 6.12, our method is based on the division of the segmented and normalized iris image into 6 regions, followed by the independent feature extraction and comparison for each of these regions. Thus, the noisy information that usually is localized in some of the iris subparts will not corrupt the whole biometric signature. Making the normalization process as described in [18] and starting from an angle of -45^{o}, regions 1 to 4 correspond to successive quadrants of the iris image. Regions 5 and 6 correspond respectively to the outer and inner parts of the iris. The main motivation for this division was the observation that the most usual types of noise (iris obstructions and reflections) are predominantly localized respectively in the upper/lower and left/right portions of the iris. Also, reflections resultant of natural and artificial lighting environments are respectively usual in the outer and inner iris regions. The proposed division schema minimizes the number of regions simultaneously affected by each type of noise.

According to the chosen feature extraction method, the process consists in the creation of six independent biometric signatures, each one correspondent to a specific iris region. The details of the tested feature extraction method are described in section 6.4.3. However, we stress that this process is independent of the feature extraction strategy. Oppositely, as

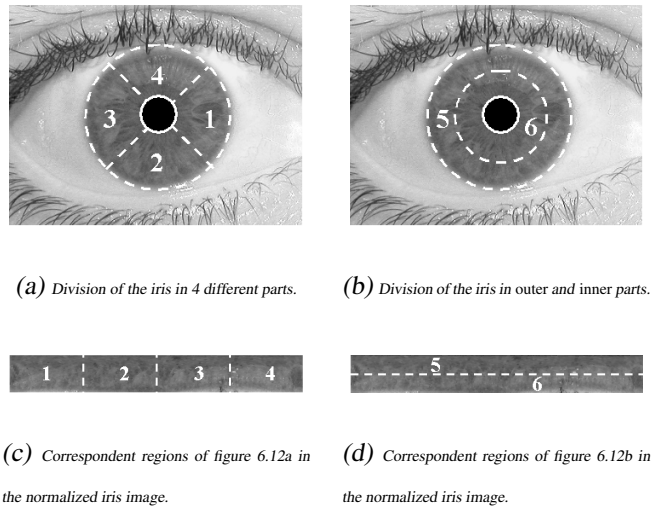

(a) Division of the iris in 4 different parts.

(b) Division of the iris in outer and inner parts.

(c) Correspondent regions of figure 6.12a in the normalized iris image.

(d) Correspondent regions of figure 6.12b in the normalized iris image.

Figure 6.12: Division of the iris in 6 regions.

the process starts from the normalized iris image, it is dependent of the previous accurate iris segmentation, which is obviously a challenge, regarding the dynamics of the non-cooperative image capturing environments.

6.4.2 Feature Comparison and Classification

In the following discussion we will use a superscript to distinguish between two different iris images, such as I^1 and I^2, and a subscript to distinguish between different regions of an iris image, such as I_1^1 and I_2^1.

Let I_j be a region of an iris image, such as the ones identified in figure 6.12. We define the function $b(I_j) : I_j \rightarrow \mathbb{R}^k$, as the biometric signature of I_j. Next, we define the dissimilarity between two signatures as $d(b(I_j^1), b(I_j^2)) : \mathbb{R}^k \times \mathbb{R}^k \rightarrow \mathbb{R}$, noting that these values are found for two signatures obtained from correspondent iris regions.

If we choose to define N regions in an iris image $I_i, i = 1, \ldots, N$, we obtain N signatures $b(I_i)$, one for each region. Consider I^1 and I^2 respectively as the template and sample images. For I^1 we have the N signatures $\{b(I_1^1), \ldots, b(I_N^1)\}$ and for I^2 the correspondent $\{b(I_1^2), \ldots, b(I_N^2)\}$.

Let D be the set that contains the dissimilarities between the correspondent regions of I^1 and I^2: $D = \{D_1, \ldots, D_N\}$ where $D_i = d(b(I_i^1), b(I_i^2)), i = 1, \ldots, N$.

Let $T = \{T_1, \ldots, T_N\}$, $T_i \in \mathbb{R}^+$, be a set of N threshold values, such that $T_i \leq T_j$, $\forall i <$

j.

We define the function $C(D, T_i) : \mathbb{R}^k \times \mathbb{R}^+ \rightarrow \mathbb{N}$, that counts the number of $D_j \in D$ that are smaller or equal to T_i, as:

$$C(D, T_i) = \sum_{j=1}^{N} \mathbb{I}_{\{D_j \leq T_i\}} \tag{6.13}$$

Images I^1 and I^2 correspond to the same iris if:

$$\exists_i : C(D, T_i) \geq i, i = 1, \ldots, N \tag{6.14}$$

The rationale behind this classification strategy consists in the inverse correspondence between the number of comparisons that must be smaller or equal to T_i and the *constraining level* of T_i.

Figure 6.13 illustrates 3 examples of the application of the proposed classification strategy. It contains the dissimilarities between the template and the sample biometric signatures of 3 subjects, represented in the horizontal axis (A, B and C). The similarity threshold set (T) is represented by the horizontal dashed lines. The application of (6.14) confirms the identity of subjects A and B and denies the identity of subject C. Subject A has one dissimilarity value below the lower threshold (T_1) and subject B has two dissimilarities below the second lower threshold (T_2). The dissimilarities that determined the identity acceptance are represented by filled circles, oppositely to the remaining ones.

As our experiments report, this method significantly decreases the false rejection rates in the recognition within noisy environments, since it isolates the noisy information in the correspondent biometric signature extracted from the iris region that contains it. This decreases the probability that noisy iris regions corrupt the whole biometric signature when extracting the lower components of the signal.

However, if the iris is divided as above described, it is not possible to achieve invariance to iris rotation through signature shifting, and this is a very common technique used in the feature comparison. We compensate this by making the normalization process into the dimensionless polar coordinate system starting from 5 different deviation angles of the segmented iris image (-10º, -5º, 0º, +5º, +10º) and obtaining 5 normalized iris images. The subsequent processing is further made separately for each of these images and the final similarity is given by the highest similarity between the enrolled signatures and those computed from each of these images.

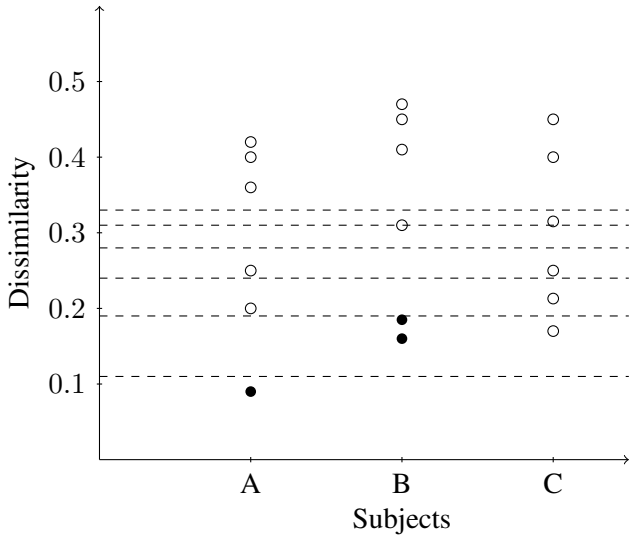

Figure 6.13: Examples of the proposed classification strategy.

6.4.3 Experiments and Discussion

In the experiments we implemented the recognition method proposed by Daugman [18] and described in section 2.2.3.1. We compared the results when following the method as described by the author and using the proposed iris division and classification strategy. To achieve independency between our experiments and the accuracy of the segmentation algorithm, we manually verified that all images from the used data sets were accurately segmented. This means that no iris segmentation errors increased the error rates rates. Initially, we made the feature extraction and comparison using the whole segmented iris, extracting a total of 2048 bits. Further, according to figure 6.12, we divided the iris into 6 regions and, through feature extraction, obtained 512 and 1024 bits respectively for the signatures extracted from the iris regions 1 to 4 and 5 to 6. The iris classification was made through the fusion rule given by (6.14). We stress that we did not implemented any noise detection technique, which increased the obtained error rates, but enabled clear conclusions about the robustness to noise of each classification strategy.

6.4.3.1 Data Sets

Similarly to the majority of the experiments described in this thesis, our purpose was the evaluation of our proposal both in highly and less noisy images, which led us to choose $UBIRIS$ and $CASIA$ and enabled the analysis of the recognition accuracy when simulat-

ing the cooperative and non-cooperative environments. Moreover, this type of dual analysis avoids the hypothesis that the method could be advantageous in the non-cooperative setting and disadvantageous within cooperative environments. We selected 400 images from each of the databases, belonging to 40 different subjects. Further, we divided each of them into 2 distinct data sets, each one containing 200 images from 20 subjects. The first data sets - $UBIRIS_{id1}$ and $CASIA_{id1}$ - were used as training, to obtain the threshold sets (T) and the latter - $UBIRIS_{id2}$ and $CASIA_{id2}$ - to evaluate the recognition accuracy. Each of the data sets enabled respectively 900 and 19000 intra- and inter-class comparisons. The selected images of the $UBIRIS$ data sets contain iris obstructions by eyelids and eyelashes, poor focused and motion blurred irises and irises with specular and lighting reflections, while those from the $CASIA$ data sets contain almost exclusively iris obstructions by eyelids and eyelashes. As in the remaining experiments of this thesis, all data sets are detailed in appendix B.

6.4.3.2 Results

The proposed classification strategy demands the computation of the dissimilarity threshold set (T) that minimizes the error rates. In order to obtain it, we started by the feature extraction and comparison using the whole iris and each of the proposed regions in both the $UBIRIS_{id1}$ and $CASIA_{id1}$ data sets.

Figure 6.14 contains the histograms of the dissimilarities between the signatures extracted from the $UBIRIS_{id1}$ data set, using the whole iris (figure 6.14a) and each of the regions individually (figures 6.14b to 6.14g). The line series correspond to the approximated normal distributions obtained through curve fitting, with a 95% confidence interval. τ_i represents the value for a t-test given by (5.1).

Through this process, we obtained the parameters of the normal distributions for each of the iris regions and type of comparisons (intra- and inter-class). Let the subscript denote the image regions (1 to 6) identified in figure 6.12 and the superscript denote respectively the intra- (I) and inter-class (E) comparisons, such as N_1^I (the normal distribution of the intra-class comparisons between the irises region 1).

The goal is to find the values for the ordered threshold set $T = \{T_1, \ldots, T_6\}$ that minimize the error rates. Let $D^E = \{D_1, \ldots, D_6\}$ be the set of random variables following the respective N_i^E, $i = 1, \ldots, 6$ distributions. According to (6.13), $C(D^E, T_k)$ is the function that counts the number of $D_j \in D^E$ that are smaller or equal to T_k. The FAR

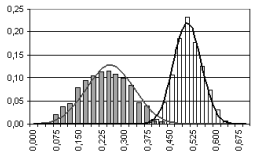

(a) Whole iris distribution. $\tau_W = 81.2$

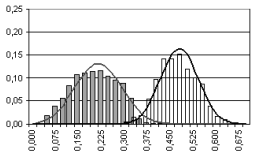

(b) Region "1" distribution. $\tau_1 = 79.9$

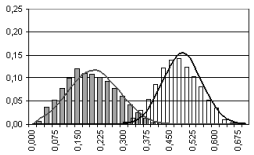

(c) Region "2" distribution. $\tau_2 = 75.7$

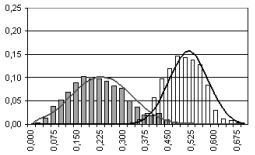

(d) Region "3" distribution. $\tau_3 = 65.3$

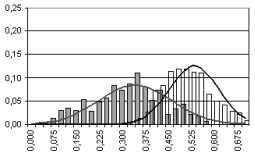

(e) Region "4" distribution. $\tau_4 = 36,6$

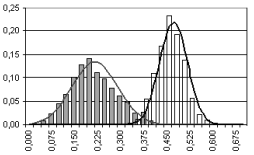

(f) Region "5" distribution. $\tau_5 = 68,2$

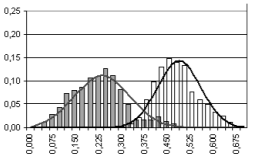

(g) Region "6" distribution. $\tau_6 = 63,0$

Figure 6.14: Histograms of the dissimilarities between the signatures extracted from the whole iris (figure 6.14a) and each of the regions identified in figure 6.12.

is given by:

$$FAR = \sum_{i=1}^{6} P\Big(C(D^E, T_i) \geq i \mid \bigcap_{j=1}^{i-1} C(D^E, T_j) < j\Big) \tag{6.15}$$

where $P(A|B)$ denotes the probability of A conditioned by the occurrence of B. Using the same notation, let $D^I = \{D_1, \ldots, D_6\}$ be the set of random variables following the respective N_i^I, $i = 1, \ldots, 6$ distributions. The FRR is given by:

$$FRR = \prod_{i=1}^{6} P\Big(C(D^I, T_i) < i\Big) \tag{6.16}$$

Using (6.15) and (6.16), we made an exhaustive search in the $[0, 1]$ interval, having tested all the possible combinations for the 6 thresholds values with 10^{-3} precision.

Figure 6.15 contains the obtained receiver operating curves, when following the classical Daugman recognition method (dashed line) and our proposal (continuous line) in the $UBIRIS_{id2}$ and $CASIA_{id2}$ data sets. These results indicate a significant decrease of the error rates by our proposal, either in the highly noisy ($UBIRIS_{id2}$) and less noisy images ($CASIA_{id2}$).

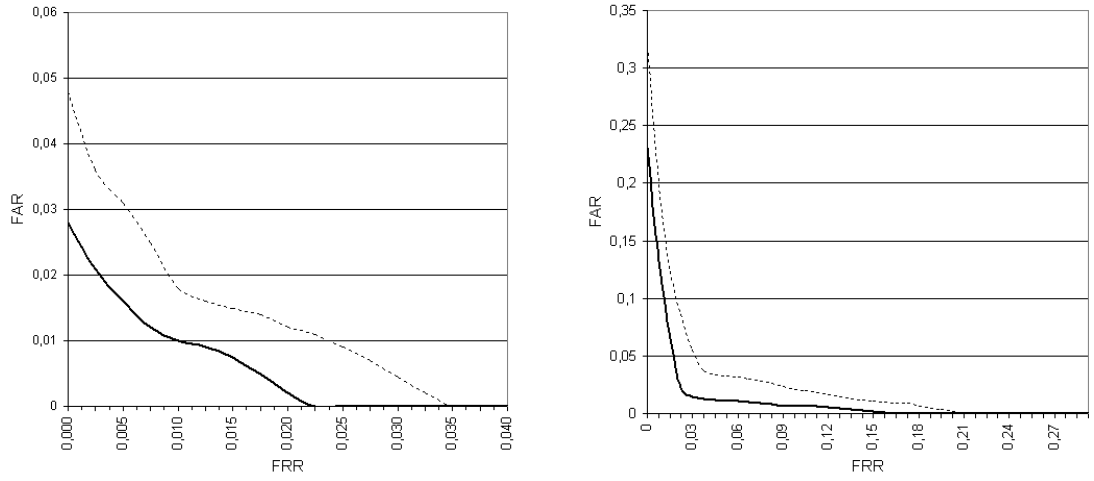

(a) Receiver operating curves obtained in the $CASIA_{id2}$ data set.

(b) Receiver operating curves obtained in the $UBIRIS_{id2}$ data set.

Figure 6.15: Comparison between the receiver operating curves (ROC) obtained by the classical Daugman recognition method (dashed line) and our iris classification strategy (continuous line) in the $CASIA_{id2}$ (figure 6.15a) and $UBIRIS_{id2}$ (figure 6.15b) data sets.

Table 6.3 contains a comparison of the obtained results by the original classification method, as described by Daugman, our iris division and classification proposals and three usual classification fusion strategies (mean, minimum and product). The first column identifies the classification method, the second contains the false rejection rates when preventing the false accepts errors. EER corresponds to the equal error rates and the last column contains the approximate percent value of the area under the ROCs. All the error rates are expressed for a confidence interval of 95%.

We confirmed that our method consistently achieved better results, as the error rates decreased about 40% when compared to the original proposal. These achievements can be observed either in the highly noisy images from the $UBIRIS_{id2}$ data set or in the less noisy images from the $CASIA_{id2}$ one.

This higher accuracy in the recognition of noisy images can be explained by its ability to perform recognition using small portions of the iris whereas avoiding the corruption of the whole signature by localized noise regions. These results led us to conclude that the proposed iris division and classification strategy is more tolerant to noise factors and, for this reason, more adequate for the application is less constrained image capturing environments.

Classification Strategy	FRR, FAR=0, %	EER, %	Error ROC, %
$\text{UBIRIS}_{\text{id2}}$ data set			
Daugman Original	22.95 ± 0.03	3.72 ± 0.01	3.21
Proposed	16.49 ± 0.02	2.38 ± 0.00	1.73
Mean	19.90 ± 0.02	4.98 ± 0.01	3.30
Minimum	18.38 ± 0.02	4.80 ± 0.01	2.39
Product	18.81 ± 0.02	4.81 ± 0.01	2.81
$\text{CASIA}_{\text{id2}}$ data set			
Daugman Original	3.41 ± 0.01	1.44 ± 0.00	0.64
Proposed	2.39 ± 0.00	1.01 ± 0.00	0.55
Mean	3.11 ± 0.00	1.26 ± 0.00	0.61
Minimum	4.62 ± 0.01	1.29 ± 0.00	0.64
Product	2.95 ± 0.00	1.20 ± 0.00	0.60

Table 6.3: Comparison of the error rates obtained when following the original Daugman's recognition method, our classification strategy and three common classification fusion strategies.

6.4.4 Conclusion

In the latter sections we addressed the problems motivated by the existence of noise in the captured iris images and the correspondent increase of the error rates, with particular relevance to the false rejections, in the context of non-cooperative iris recognition.

Common feature extraction strategies usually focus in the lower and middle low frequency components of the signal, which implies that small portions of non-identified noise can corrupt the whole biometric signature and decrease the recognition accuracy.

Based on this, we proposed a new iris classification strategy that divides the iris into 6 regions and makes independent feature extraction and comparison for each of these regions. Iris classification is achieved through a classification rule that uses a threshold set to combine the dissimilarity values resultant from the comparison between correspondent iris regions.

Experiments in the recognition of noisy images showed a significant decrease in the error rates, above 40% in the false rejections. Moreover, as can be seen by the results presented in table 6.3, we performed a comparison between our proposal and three common classification fusion strategies - product, mean and minimum - and the proposed method consistently achieved lower error rates.

6.5 Summary

This chapter was devoted to the description and experimental evaluation of our proposals to deal with noisy iris images for biometric recognition purposes. Assuming that, in spite of noisy, the iris segmentation was accomplished, our main objective was the increase of recognition robustness to such noise factors.

After previously concluding, as described in chapter 5, that the localized noise that obstructs portions of the iris texture can hardly be replaced, we focused our efforts on the development and proposal of methods able to deal with noise and achieve recognition accuracy, even in such challenging conditions.

First, we proposed a method for feature quality measurement, which later constraints the features that are taken into account in the computation of the biometric signatures' dissimilarity. Next, we described our feature selection proposal, that is based on the analysis of the predominant noisy regions of the images captured in each specific imaging environment to select the features with highest discriminating capacity. Finally, our iris division and classification strategies were detailed, in order to avoid that localized noise corrupts the whole biometric signature, when extracting the lower frequency components of the original data.

We concluded that each of these proposals contributes for the increase of the adaptability and robustness of iris recognition to noise factors, satisfying the purposes that motivated them. Moreover, we stress the independence between all of these methods and the particular feature extraction and comparison used by the iris recognition strategy, which is obviously a strong point, regarding its applicability. However, we stress that these results are dependent from the previous accurate iris segmentation, which is highly challenging, given the dynamics of non-cooperative environments. The requirement of optical frameworks that are able to capture iris images with enough quality and of real-time face and eye localization methods, is assumed too.

In short, it is our belief that each of the proposals described in this chapter is propitious for the application in less constrained imaging capture environments, thus in a non-cooperative setting, and contributes to increase the range of domains where iris recognition can be applied.

Chapter 7

Conclusions

During the last three years, the main purpose of our research was the development of reliable personal recognition based on iris images captured at a distance, without requiring the subjects cooperation and under heterogeneous lighting conditions: the non-cooperative iris recognition.

After introducing and delimiting the theme, it must be stressed that the complete achievement of such a recognition system will have a significant impact in a broad range of domains, specially those related with security and reliability. By not demanding the users' cooperation, it is possible to perform covert recognition, which, among other advantages, minimizes of the probability for active counterfeit measures. Oppositely, several questions concerning the users' privacy subsist and should be object of legal framing.

As described along this thesis, the dynamics of the imaging environments lead to the appearance of highly heterogeneous images with the iris information corrupted by several types of noise. These images significantly increase the difficulty of performing reliable recognition, which is a problem identified by several authors.

We believe that this thesis constitutes a step-ahead towards the non-cooperative iris recognition. While evaluating the robustness to noise that common iris recognition proposals present, we found a potential weak point. We concentrated our efforts in the proposal of methods that, together with the existing recognition methods, significantly contribute to the robustness of iris recognition regarding noise factors, as reflections and iris obstructions. As illustrated by figure 1.3, our proposals comprise the main stages of typical recognition systems and the independence between each one and the particular iris recognition strategies must be stressed. Since the earlier stages of our work, one of our main objectives was the

proposal of methods that could be applied to different iris recognition strategies, which contributes for their potential use in different scenarios. We considered this as an achieved goal.

We hope that this thesis has shown the challenge of performing reliable human recognition based on noisy iris images. Again, it must be enhanced the significant decrease in the accuracy of current iris recognition proposals when the captured images contain significant portions of noise. Overcoming this was the main motivation for our work and, as a result, we described and experimentally evaluated methods that act in the iris segmentation and normalization, in the feature extraction and comparison stages. The obtained results were highly satisfactory, reducing the error rates in the recognition of noisy iris images in about 40-50%, which must be considered an achievement.

An overall explanation for the observed improvements in the recognition accuracy can be given by two factors: first, the ability to distinguish between biometric features, either by assigning them quality values or by selecting those with higher discriminant capacity in each specific imaging environment. Second, the avoidance of corruption of the whole biometric signature, as a result of the extraction of the lower frequency components of noisy iris images. The notion of *biometric sub-signature*, resultant of the feature extraction within small iris regions, avoids that localized noise regions can significantly decrease the recognition accuracy, although significantly increased the computational demands of the process itself.

To conclude, we consider that we have accomplished the main purposes of our work. However, the planning and construction of the optical image capturing framework has revealed itself as harder and more expensive than initially thought, and is presently the main subject of our research work, as we expect to build a non-cooperative recognition system prototype.

7.1 Contributions and Achievements

As we searched for the goal of non-cooperative iris recognition, a number of new ideas were developed. These can be summarized as follows: the construction of a new iris image database, the proposal of methods to perform the iris segmentation, the localization of noise regions within normalized images and the increase in the robustness to noise of common iris recognition proposals, with emphasis to the classical Daugman's recognition method.

First, the development of a new iris image database, with distinguishable characteristics from the remaining ones, has represented a valuable resource to the research and development of more robust iris recognition proposals. As it is stated before, the conclusion about the acceptance of the $UBIRIS$ database by the research and academic communities can be gauged by the number of users (more than 360) from 60 countries that requested the access to the database.

The iris segmentation challenges, which are highlighted by the non-cooperative imaging setting, motivated our segmentation proposal. It is based in the creation of an intermediate image, used in the construction of the edge-map. This image has much less information than the captured one and a smaller number of intensities, which facilitates the task of the edge detector and propitiates the accuracy of the form fitting algorithm. It must be stressed that this method has obtained the best results of any of the methods compared, even in images with high portions of noise, either with severe iris obstructions or with very large iris reflection areas.

Assuming that the iris segmentation was accomplished, we focused our efforts in the development of a method that localizes the regions correspondent to noise in the segmented and normalized iris images. This method produces a binary map, where the noise-free and the noise regions are distinguished. This information is used by our feature quality and selection proposals to perform the biometric recognition on noisy iris images.

Starting from the normalized images, together with the correspondent binary maps that localize the noise regions, we developed methods that, more than alternatives, were thought to be used together with the existing iris recognition proposals, in order to increase their robustness to noise and image heterogeneity. With this purpose, we described a method to measure the quality of the extracted biometric features and use this value to constraint the features than are taken into account in the computation of the similarity between iris signatures. Its rationale is to compute the proportion between the noise-free and noise pixels that were used in the computation of each feature. Lower quality values correspond to features that were extracted from typical noise pixels, and, as such, it is probable that the resultant feature value is corrupted and with small discriminating capacity. We further applied a threshold in the feature comparison, in order to compute the similarity between iris signatures using exclusively noise-free features, or at least those that were extracted from a majority of noise-free pixels.

Further, we proposed a feature selection method to increase the iris recognition adaptability to the distinct characteristics of each imaging environment. After having observed

that common iris recognition proposals do not take into account the typical noise regions resultant of each specific lighting conditions and optical hardware used, we proposed a method that uses a training set of images, captured within the environment where the recognition system is functioning, to obtain information about the discriminating capacity of each feature, which we hypothesized that should vary according to the typical noise regions induced by the environment.

Finally, we proposed a strategy to perform the iris classification based in several independent biometric *sub-signatures*. After observing that, commonly, the noise regions of the captured irises are localized in some subpart of the iris, we proposed the division of the segmented and normalized iris image into 6 different regions and performed independent feature extraction and comparison on each region. The hope is that any eventual noise region should be circumscribed to some of the iris sub-regions and will not corrupt the biometric signatures extracted from the noise-free regions. Further, the classification is achieved through a fusion rule, that is based in an inverse correspondence between the necessary similarity between iris signatures to accept a match and the number of correspondent regions that must achieve that minimal similarity.

The results of the mentioned methods were highly encouraging, since each of them isolated improved the recognition accuracy in about 30-40%. Moreover, we stress that the rationale of any of our proposals is quite straightforward and any of them can be used together with different iris recognition strategies. These are obviously strong points, regarding their potential applicability and the eventual optimization, in which our research is currently focused.

7.2 Future Work

We are currently working on the analysis of the requirements for the physical implementation of the non-cooperative prototype system. This has revealed, specially the planning of the optical framework, as a task with higher difficulty than we initially thought.

Simultaneously, we are implementing, and in specific situations adapting and improving, algorithms for the real-time human silhouette, face and and eye detection. Our purpose demands algorithms with high performance, which decreased the number of potential alternatives.

Regarding the experiments and results contained in this thesis, we are presently per-

forming the experimental evaluation of the proposed methods with larger data sets, in order to obtain information about the advantages resultant of the methods with higher statistical relevance. Moreover, we are performing the comparison between three common iris recognition proposals (Daugman's [19], Wildes' [120] and Ma *et al.* [64]) as they are described by the authors and together with the totality of our proposals. This will bring us new information about the improvements in the recognition accuracy, according to different recognition strategies.

The evaluated types of noise should be the subject of further work, since this work has not dealt, for instance, with off-angle iris images. This will obviously introduce new challenges to the recognition that must be overcome, and predictably demand the adjustment of some of our methods to these new constraints.

Appendix A

Implementation

This appendix is devoted to the description of the software implemented to perform our experiments. We detail the most relevant features of the builded framework, which is concerned mainly with user-friendliness and easy-parametrization. We also present the final deployed application, where performance was considered a priority.

A.1 Experiments' Framework

In the earlier stages of our work, the requirements of test and analysis of several iris recognition methods lead us to use MATLAB as the programming environment for the rapid application development (RAD). However, we immediately observed that this environment - that concerns essentially about user friendly and easy code syntax - has very low performance. Since common image processing and pattern matching algorithms are usually of high computational requirements, the complete iris recognition process lasted for several seconds. As an example, it can be referred that an algorithm similar to the Daugman's recognition method uses about 3 minutes to perform one recognition in the verification mode, which makes it impracticable for our purposes.

Therefore, we decided to build an application using the C++ language, with the main purpose of allowing the test and comparison of iris recognition algorithms with maximal performance. The desired application should have two major concerns: parametrization and performance. We wanted the possibility of quick defining and adjusting the parameters of each iris recognition algorithm and of each one of its stages. The code should be optimized to enable the execution of recognition process in few seconds.

The kernel of this application was developed in the last months of 2004 and it has constituted as a valuable tool for the achievement our proposals.

Figure A.1 illustrates a screen capture of the developed framework. The typical image processing algorithms are located in the right panel and can be dragged to the central one, where processes are built. Every algorithm has a number of expected parameters and returns a result that can be further used as the input to other(s) algorithm(s). This run-time definition of image processing methods through the link of algorithms constitutes one of the biggest advantages of the implemented framework.

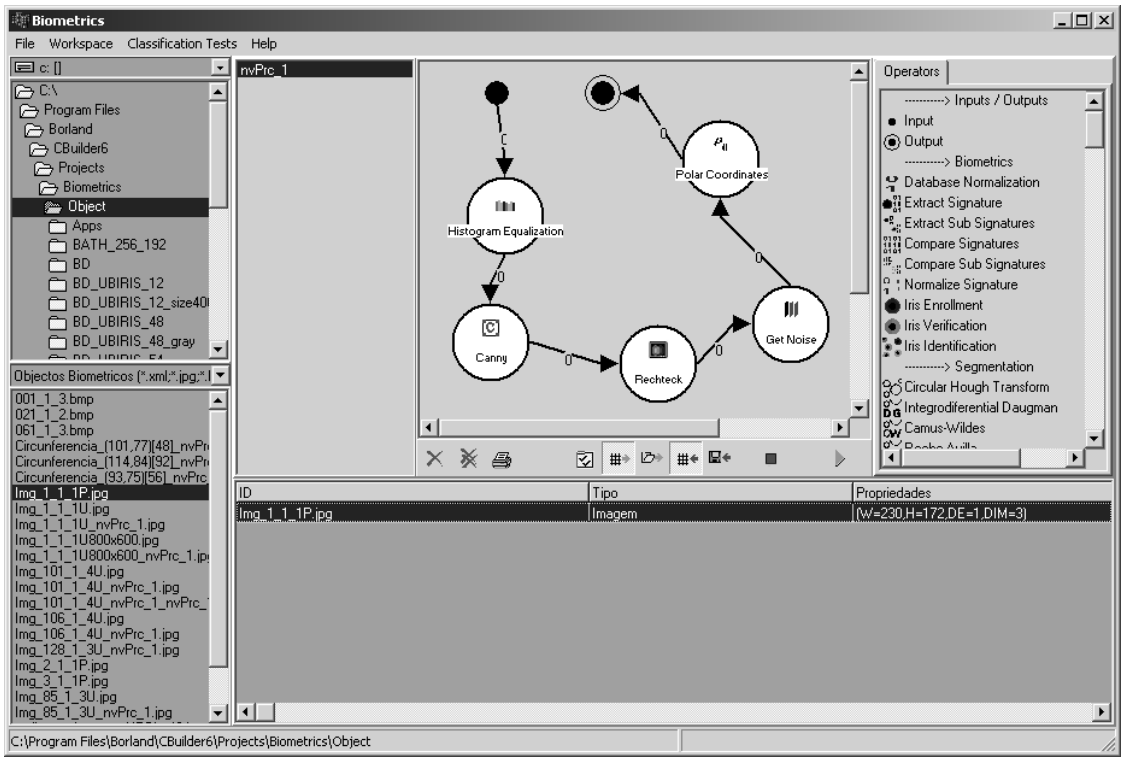

Figure A.1: Developed framework for the test and comparison of iris recognition algorithms.

Another relevant feature of the implemented application is the minimal level of formation required to the users that start to work with it. The only existing basic concepts are: $object$, $operator$ and $process$. The first is anything that can be modified by an operator (e.g., an image or a vector). An operator is simply an algorithm that receives a set of objects as input, performs a simple operation and returns the results, a modified object that can be redirected to another operator. At the highest level, every process is regarded as an ordered set of connected operators, where the connections specify the flow of objects between operators.

The graphical interface allows the users to build complex processes exclusively through drag-and-drop operations. With the purpose of illustrating the simplicity of the creation of a new process, figure A.2 shows the three step sequence needed to construct of an edge-map, through the widely used and well known Canny edge detector, followed by the form fitting task, through the circular Hough transform. First, in a notation similar to popular state diagrams, the process input and output are defined, through drag-and-drop of the respective symbols (figure A.2a). Further, once again through drag-and-drop, both operators are included (figure A.2b) and, if the user wants to adjust the parameters of each operator, the just has to double-click on the desired one. Finally, the flow of objects between operators is defined (figure A.2c). In this example, the initial object is received by the edge detector and its result (binary edge-map) is redirected to the input of the form fitting operator. Finally, this operator returns a $circunference$ object, denoting the image location where the potential for the existence of a circumference is maximal.

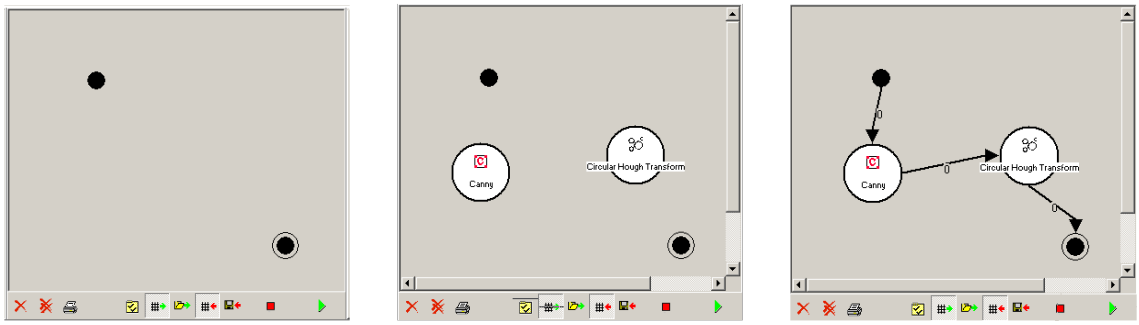

(a) Definition of the process input and output

(b) Inclusion of the operators

(c) Definition of the flow of objects within the process

Figure A.2: Construction of a process through the implemented experiments' framework.

Every operator has a configuration file in the XML format, with a complete specification of the type and number of required parameters, as well their default values. This facilitates the readability and interpretation of the operator itself and its parametrization. Figure A.3 exemplifies the configuration file of one of the implemented image processing operators, the circular Hough transform. It specifies that the operator must receive an *imagem* (image) as parameter and has four configuration parameters: *raio maximo* (maximum radius) and *raio minimo* (minimum radius) respectively indicate the upper and lower limits of the potential radius of the circumferences, and *reduz espaço procura* (reduce search space) and *contida imagem* (contained in image) that act as performance improvement parameters.

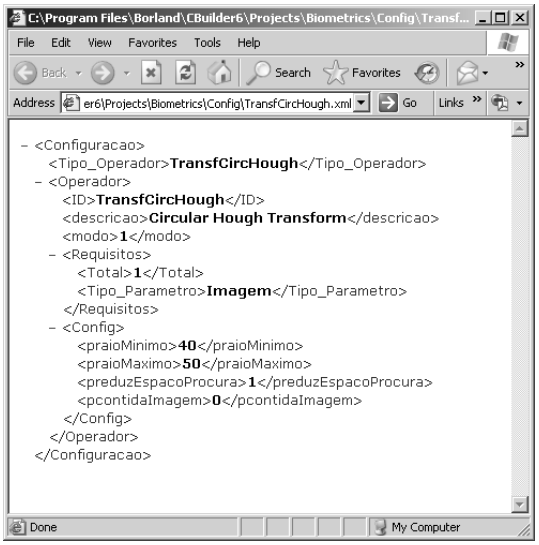

Figure A.3: XML configuration file of the circular Hough transform.

The *Microsoft Windows XP* executable and configuration files of the implemented operators are freely available for download in the $UBIRIS$ website[1] and, from our viewpoint, can constitute a valuable tool for the development and test of biometric recognition proposals. Further, we plan to implement each *operator* as an isolated dynamic link library (DLL), which will enable the dynamic creation of operators and its incorporation in the application without requiring the compilation and rebuilding of the whole source code.

A.2 Application Deployment

In the final stage of our research work, we focused on the deployment of the implemented recognition processes, again with two major concerns: performance and compliance with the defined standards for the biometric field. First, we optimized the source code regarding performance. The compliance with the defined standards was accomplished following essentially the Common Biometric Exchange File Format and the BioAPI. These define respectively the standard structure of the biometric data and of the APIs that develop biometric-related applications. In the following sub-sections they are briefly described.

[1] http://www.iris.di.ubi.pt

A.2.1 Common Biometric Exchange File Format

The Common Biometric Exchange File Format (CBEFF) describes a set of data elements necessary to support biometric technologies in a common way. These data can be placed in a single file used to exchange biometric information between different system components or between systems. The result promotes interoperability of biometric-based application programs and systems developed by different vendors by allowing biometric data interchange [81].

The expected benefits of CBEFF are the ability to identify different biometric data structures (public or proprietary) supporting multiple biometric types within a system or application, the ability to reduce the need for additional software development and the ability to promote development cost savings. CBEFF describes a set of *required* and *optional* fields, a *domain of Use* to establish the applicability of a standard or specification that meets CBEFF requirements, and a process by which new technology or systems can create formats that meet these requirements.

It includes the definition of format and content for data elements such as:

- A biometric data header that contains such information as version number, length of data, whether the data is encrypted or not, etc., for each biometric type available to the application or system;

- Biometric data, with the content not specified;

- Any other required biometric data or data structures;

- Description of the means for obtaining a unique value for identifying the format (owner and type) of the biometric data;

According to this standard, the CBEFF data elements, which are placed in fields inside a CBEFF file, are composed by three fields:

Standard Biometric Header (SBH) Apart from other optional fields, the SBH must contain information about the security options of the data element (plain, encrypted or signed data), the ID of the group or vendor which defined the data element, the specific format of the following BSMB and information about the version of the data element.

Biometric Specific Memory Block (BSMB) This block contains the biometric data in any specific format that must be specificated in the SBH. Thus it can be either a proprietary format, or one agreed upon by a standards body, working group, or industry consortium.

Signature Block (SB) This field holds the signature or MAC data. It can contain algorithm identifier information and/or any parameters needed to perform the signature and/or the MAC function. This field exists only if the header it is defined the encrypted or signed data option.

A.2.2 BioAPI

The BioAPI Consortium was founded to develop a biometric API that brings platform and device independence to application programmers and biometric service providers. The BioAPI Consortium is a group of over 120 companies and organizations that have a common interest in promoting the growth of the biometrics market [6].

The BioAPI Consortium developed a specification and reference implementation for a standardized API that is compatible with a wide range of biometric application programs and a broad spectrum of biometric technologies. In the deployment of our proposed algorithms for iris recognition, we considered valuable, its implementation according to the BioAPI specification. This document is freely available in the Internet and has been created to allow applications to interact with a wide variety of biometric devices and even different types of biometrics, without needing to know the details of how the different devices work. It is compliant with the CBEFF, described in the National Institute of Standards Publication, NISTIR 6529.

It assists the application developers in writing applications truly usable with as wide variety of biometric technologies as possible and to assist BSP developers in writing BSPs that meet the requirements of as many applications as possible. This specification provides:

- Standard access methods to biometric functions, algorithms, and devices.
- Simple application interfaces.
- Robust biometric data management and storage.
- Standard methods of managing biometric data and technology types.

- Support for biometric verification and identification in distributed computing environments.

According to the scope and objectives of our research work, among other potential advantages, we enhanced:

- The rapid development of applications employing biometrics.
- Flexible deployment of biometrics across platforms and operating systems.

A.2.3 Application Performance

Although the time spent in the performance optimization was not the desirable and several work with this purpose remains, we achieved a significant decrease of the average elapsed time of a recognition process. Obviously, this value is strongly dependent of the initial dimension of the captured iris images as well of other parameters that determine the relationship between accuracy and performance. However, it must be stressed that the performance of the final deployed application was about five times better than the one of the experiments' framework and 156 times better than the obtained with the initial MATLAB code. Table A.1 summarizes the average time elapsed for a recognition process in the verification mode (1:1). The first column identifies the type of application and the second specifies the average elapsed time (in seconds). These values were obtained through averaging of 100 recognition processes, on a personal portable computer with a 2.2Ghz *Pentium 4* processor and 512MB of dedicated RAM memory.

Application	**Average Elapsed Time, s.**
MATLAB code	180.36
Experiments framework, C++	5.80
Deployed application, C++	1.15

Table A.1: Average elapsed time for a recognition process in the verification mode (1:1).

Appendix B

Description of the Data Sets

In order to facilitate the reproduction of the presented results and the comparison with other methods, in this appendix we describe the data sets used in our experiments. As can be seen by the following description, the majority of the used data sets comprises images of the $UBIRIS$ database. This is motivated by its higher noise quantities and types, which can be confirmed in table 3.2. When it was considered specially relevant the analysis of a method's accuracy simultaneously in both high and low noise or noisy-free data, images from other databases were used, specially those from $CASIA$ and $UPOL$. $CASIA$ was the first database available for biometric purposes and, as such, it is by far the most used in the iris recognition research and acts almost as a standard comparison measure of common recognition proposals. The $UPOL$ database was the only one found with completely noise-free images, which enables conclusions about a method's accuracy in optimal conditions.

B.1 Experiments' Data Sets

$UBIRIS_{seg}$ - This data set comprises 1877 images of the $UBIRIS$ database belonging to 241 subjects. It enables respectively 8415 and 1752190 intra- and inter-class comparisons and its images have fixed dimensions of 800 $\times$ 600 pixels (width $\times$ height). It was used in the experiments related with the iris segmentation, which are described in chapter 4. Contains images captured in two different sessions, with three weeks of interval. Predominantly, images of the first session have good quality - to simulate the enrollment process - and images of the second session contain all the noise factors that the $UBIRIS$ database incorporates and are highly heterogeneous,

in order to simulate the non-cooperative image capturing.

$UBIRIS_{inp}$ - Comprises 400 segmented and normalized images of the $UBIRIS$ database, belonging to 40 subjects. This data set enables respectively 1800 and 78000 intra- and inter-class comparisons. Images have fixed dimensions of 512 $\times$ 64 pixels (width $\times$ height) and were used in the experiments about the use of inpainting techniques in normalized and noisy iris images. Since it constituted a goal that the images contain large noise regions, we selected those with noise homogeneously distributed across all regions. As the iris obstructions by eyelids and eyelashes are predominant in the lower regions of the normalized iris images, to compensate this, we selected images with large reflections areas, either specular or lighting, which are predominant in the lateral iris regions.

$UBIRIS_{noi}$ - 100 segmented and normalized iris images belonging to 100 different subjects. These images have fixed dimensions of 512 $\times$ 64 pixels (width $\times$ height) and were used in the experiments associated with the detection of noisy regions in normalized iris images. Due to this, images with the highest noise quantities and types of noise were selected, but we verified that the segmentation algorithm can accurately perform the iris segmentation on every image.

$UBIRIS_{ali}$ - This data set comprises 130 images from 13 subjects, enabling a total of 585 and 7800 intra- and inter-class comparisons. Images belong to the $UBIRIS$ database, have fixed dimensions of 800 $\times$ 600 pixels (width $\times$ height) and were used in the experiments of section 6.1. These consisted in the evaluation of the recognition accuracy as the dimension of the irises in the captured images varies. The simulation of the varying size was made through bi-cubic interpolation, between 100% and 10% of the initial images size. As in the majority of the other data sets, we manually verified that the used segmentation algorithm performed its task accurately on every data set image.

$UPOL_{ali}$ - This data set contains 132 images from 44 subjects of the $UPOL$ database. Images have fixed dimensions of 768 $\times$ 576 pixels (width $\times$ height) and enable respectively 132 and 8514 intra- and inter-class comparisons. Similarly to the previous data set, it was used in the experiments described in section 6.1. As the remaining images of this database, all the images are completely noise-free. In order to avoid that segmentation errors could corrupt the analysis, we manually verified that the

segmentation algorithm performed accurately on each of the images.

$UBIRIS_{qua1}$ - These 130 images are from the $UBIRIS$ database and belong to 13 subjects. They have fixed dimensions of 800 $\times$ 600 pixels (width $\times$ height) and enable respectively 585 and 7800 intra- and inter-class comparisons. They were used in the experiments of our proposed method for the feature quality measuring. As we considered useful to evaluate the benefits of this method in images that, although noisy, have different quantities of noise, they correspond to the 130 less noisy images from the originally builded $UBIRIS_{qua}$ data set.

$UBIRIS_{qua2}$ - Similarly to the previous data set, this data set comprises 130 images from 13 subjects and corresponds to the noisiest images from the original $UBIRIS_{qua}$ data set. In spite of having severe iris obstructions by eyelids and eyelashes and large reflection areas (both specular and lighting), we manually verified the accuracy of the segmentation algorithm for every data set image. This enabled us to conclude about the benefits that our proposed method for feature quality measuring could have both in highly and less noisy images.

$UBIRIS_{fs1}$ - This data set contains 200 images from 20 subjects, enabling a total of 1800 and 87000 intra- and inter-class comparisons. Images have fixed dimensions of of (768 $\times$ 576) pixels (width $\times$ height) and were used in the learning stage of our proposed feature selection method. This method should increase the adaptability of the recognition system to typical imaging conditions and, thus, we selected images with similar noise characteristics, namely the predominant type and localization of the noise regions. This enabled the simulation of the typical noise regions that occur in each imaging environment.

$UBIRIS_{fs2}$ - It corresponds to the data set used in the evaluation of the proposed feature selection method. Contains 200 images from 20 subjects, for a total of 1800 and 87000 intra- and inter-class comparisons. The type of experiments where it was used demanded that the images had similar characteristics to the previous data set, in order to simulate the predominant noise regions that result from each specific image capturing environment. As in the above data set, although the images are highly noisy, we manually verified that the used segmentation algorithm can accurately perform its task in every image of the data set.

$CASIA_{fs1}$ - This data set has a similar purpose as the $UBIRIS_{fs1}$, contains an equal

number of images and enables an equal number of intra- and inter- class comparisons. Images have fixed dimensions of 320 $\times$ 280 pixels (width $\times$ height). It was used in the learning stage of the feature selection method described in section 6.3, in order to perform the method's evaluation in less noisy iris images.

$CASIA_{fs2}$ - Similarly to the $UBIRIS_{fs2}$ data set, it was used to evaluate the recognition accuracy of our feature selection method that was trained with $CASIA_{fs1}$ images. Since we decided to have an equal number of training and test images, the data set has 200 images from 20 subjects.

$UPOL_{fs1}$ - This was the third data set used in the learning stage of our feature selection method. Contains 132 images from 44 subjects, enabling a total of 132 and 8514 intra- and inter-class comparisons. Its inclusion in the experiments is justified by our purpose to evaluate the feature selection benefits either in highly, less noisy and noise-free environments. This one was used in the learning stage of the method. As the remaining images of the $UPOL$ database, images are completely noise-free and have fixed dimensions of 768 $\times$ 576 pixels (width $\times$ height).

$UPOL_{fs2}$ - These 132 images from 44 subjects are completely noise-free and were used in the evaluation of the recognition accuracy of our feature selection proposal. The number of possible intra- and inter-class comparisons, as well the dimension of the images are equal to the previous data set.

$UBIRIS_{id1}$ - This data set comprises 200 images from 20 subjects and enables a total of 1800 and 87000 intra- and inter- class comparisons. Its images have fixed dimensions of 800 $\times$ 600 pixels (width $\times$ height). It was used in the learning stage of our iris classification strategy, which demanded the inclusion of iris images with noise distributed across the majority of the iris regions. Thus, we selected essentially images with significant reflections and iris obstruction areas.

$UBIRIS_{id2}$ - These 200 images from 20 subjects allowed us to perform respectively 1800 and 87000 intra- and inter-class comparisons and were used in the evaluation of our iris classification proposal. They have fixed dimensions of 800 $\times$ 600 pixels (width $\times$ height) and contain predominantly large reflection and iris obstructions areas, in order to distribute as evenly as possible the noise across the irises regions.

$CASIA_{id1}$ - We considered useful to evaluate the merits of our iris classification strategy when the images contain small portions of noise and when the noisy regions are

concentrated in specific iris regions. To achieve these purposes, we selected 200 images from 20 subjects of the $CASIA$ database and used this data set in the training stage of our iris classification proposal. As in the above described data sets, the number of selected images allowed respectively 1800 and 87000 intra- and inter-class comparisons. Images have fixed dimensions of 320 $\times$ 280 pixels (width $\times$ height) and its noise regions are almost exclusively related with iris obstructions by eyelids and eyelashes in the vertical iris extremes.

$CASIA_{id2}$ - This data set comprises the same number of images as the $CASIA_{id1}$ and was used in the evaluation of our iris classification strategy. Its images have characteristics similar to the learning data set, which are essentially related with iris obstructions due to eyelids and eyelashes in the vertical iris extremes. The dimensions and number of possible intra- and inter-class comparisons are the same as the previous data set.

Bibliography

[1] Jafar Ali and Aboul Hassanien. An iris recognition system to enhance e-security environment based on wavelet theory. *AMO - Advanced Modeling and Optimization, vol. 5, no. 2*, pages 93–104, 2003.

[2] Denis Baldisserra, Annalisa Franco, Dario Maio, and Davide Maltoni. Fake fingerprint detection by odor analysis. In *Proceedings of the International Conference on Biometric Authentication (ICBA06)*, pages 265–272, Hong Kong, January 2006.

[3] Mary Bellis. Inventors: Police technology and forensic science, 2006. `http://inventors.about.com/library/inventors/blforensic.htm`.

[4] M. Bertalmio, L. Vese, G. Sapiro, and S. Osher. Simultaneous structure and texture image inpainting, 2002.

[5] R.C Bezdek, R. Ehrlich, and W. Full. FCM: The fuzzy c-means clustering algorithm. *Computers and Geosciences, vol. 10*, pages 191–203, 1984.

[6] BioAPI Consortium. BioAPI specification, version 1.1, 2006. `http://www.bioapi.org/`.

[7] Biometric News Portal. Hand vein biometric, 2006. `http://www.biometricnewsportal.com/palm_biometrics.asp`.

[8] W. W. Boles and B. Boashash. A human identification technique using images of the iris and wavelet transform. *IEEE Transactions on Signal Processing, vol. 46, no. 4*, pages 1185–1188, April 1998.

[9] Leo D. Bores. Ocular anatomy, 2002. `http://www.e-sunbear.com`.

[10] Manfred Bromba. Biometrics FAQ's, 2006. `http://www.bromba.com/faq/biofaqe.htm`.

[11] T.A. Camus and R. Wildes. Reliable and fast eye finding in close-up images. In *Proceedings of the IEEE 16th International Conference on Pattern Recognition*, pages 389–394, Quebec, August 2002.

[12] J. Canny. A computational approach to edge detection. *IEEE Transactions on Pattern Analysis and Machine Intelligence, vol. 8*, pages 679–698, 1986.

[13] Kathleen Carr. Keeping an eye on refugees, 2003. `http://www.cio.com/archive/081503/tl_refugees.html`.

[14] Yi Chen, Sarat C. Dass, and Anil K. Jain. Localized iris image quality using 2-D wavelets. In *Proceedings of the 2006 International Conference on Biometric*, pages 373–381, Hong Kong, 2006.

[15] Antonio Criminisi, Patrick Pérez, and Kentaro Toyama. Region filling and object removal by exemplar-based image inpainting. *IEEE Transactions on Image Processing, vol. 13, no. 9*, pages 1200–1212, September 2004.

[16] Jiali Cui, Yunhong Wang, Tieniu Tan, Li Ma, and Zhenan Sun. A fast and robust iris localization method based on texture segmentation. In *Proceedings of the SPIE Defense and Security Symposium, vol. 5404*, pages 401–408, August 2004.

[17] John Daugman. Iris recognition, 2006. `http://www.cl.cam.ac.uk/~jgd1000/`.

[18] John G. Daugman. High confidence visual recognition of persons by a test of statistical independence. *IEEE Transactions on Pattern Analysis and Machine Intelligence, vol. 25, no. 11*, pages 1148–1161, November 1993.

[19] John G. Daugman. Phenotypic versus genotypic approaches to face recognition. In *Face Recognition: From Theory to Applications*, pages 108–123. Heidelberg: Springer-Verlag, 1998.

[20] John G. Daugman. How iris recognition works. *IEEE Transactions on Circuits and Systems for Video Technology, vol. 14, no. 1*, pages 21–30, January 2004.

[21] Kresimir Delac and Mislav Grgic. A survey of biometric recognition methods. In *Proceedings of the* 46^{th} *International Symposium Electronics in Marine (ELMAR-2004)*, pages 184–193, Croatia, June 2004.

[22] A. P. Dempster, N. Laird, and D. Rubin. Maximum likelyhood from incomplete data via the EM algorithm. *Journal of the Royal Statistic Society, vol. 39*, pages 1–38, 1977.

[23] Damien Dessimoz, Jonas Richiardi, Cristophe Champaud, and Andrzej Drygajlo. Multimodal biometrics for identity documents. Technical report, Universy of Lausanne, 2005. `http://www.securitydocumentworld.com/client_files/`.

[24] WhatIs Dictionary. IT encyclopedia and learning center, 2005. `http://whatis.techtarget.com/`.

[25] Division of Criminal Justice Services. Taking bertillon measures, 2006. `http://criminaljustice.state.ny.us/ojis/history/ph_measr.htm`.

[26] Michal Dobes and Libor Machala. UPOL iris image database, 2004. `http://phoenix.inf.upol.cz/iris/`.

[27] Vivekanand Dorairaj, Natalia Schmid, and Gamal Fahmy. Performance evaluation of non-ideal iris based recognition system implementing global ICA encoding. In *Proceedings of the IEEE International Conference on Image Processing (ICIP 2005)*, pages 285–288, Italy, September 2005.

[28] Yingzi Du, Bradford Bonney, Robert Ives, Delores Etter, and Robert Schultz. Analysis of partial iris recognition using a 1-d approach. In *Proceedings of the IEEE International Conference on Acoustics, Speech and Signal Processing (ICASSP'05)*, pages 961–964, U.S.A., March 2005.

[29] Yngzi Du, Robert Ives, Delores Etter, Thad Welch, and Chein Chang. A new approach to iris pattern recognition. In *Proceedings of the SPIE European Symposium on Optics/Photonics in Defence and Security, vol. 5612*, pages 104–116, October 2004.

[30] R. Duda, P. Hart, and D. Stork. *Pattern Classification*. Wiley Interscience, New York, 2001.

[31] Jan Ernst. Iris recognition homepage, 2006. `http://iris-recognition.org`.

[32] Craig Fancourt, Luca Bogoni, Keith Hanna, Yanlin Guo, Richard Wildes, Naomi Takahashi, and Uday Jain. Iris recognition at a distance. In *Proceedings of the 2005 IAPR Conference on Audio and Video Based Biometric Person Authentication*, pages 1–13, U.S.A., July 2005.

[33] Stephen D. Fried. Domain access control systems and methodology, 2004. `http://www.itu.dk/courses/SIAS/E2005/AU2240_01.pdf`.

[34] Guodong Guo, Michael Jones, and Paul Beardsley. A system for automatic iris capturing. *Mitsubishi Electric Research Laboratories*, 2005. `http://www.merl.com/publications/TR2005-044`.

[35] Dan Witsner Hansen and Arthur A.C. Pece. Eye tracking in the wild. *Elsevier Computer Vision and Image Understanding, vol. 98*, pages 256–182, 2005.

[36] Kazuhiro Hotta, Masaru Tanaka, Takio Kurita, and Taketoshi Mishima. An efficient search method based on dynamic attention map by ising model. *IEICE Transactions on Information & Systems, vol. E88-D, no. 10*, pages 2286–2295, October 2005.

[37] Junzhou Huang, Yunhong Wang, Tieniu Tan, and Jiali Cui. A new iris segmentation method for recognition. In *Proceedings of the 17th International Conference on Pattern Recognition (ICPR04), vol. 3*, pages 23–26, 2004.

[38] Ya Huang, Si Luo, and En Chen. An efficient iris recognition system. In *Proceedings of the First International Conference on Machine Learning and Cybernetics*, pages 450–454, China, November 2002.

[39] Li Huiqi and O. Chutatape. Automated feature extraction in color retinal images by a model based approach. *IEEE Transactions on Biomedical Imaging, vol. 51, issue 2*, pages 246–254, February 2004.

[40] Human Recognition Systems, Ltd. Biometric comparison chart, 2006. `http://www.hrsltd.com/identification_technology/biometric_comparison_chart.htm`.

[41] Alfred Iannarelli. *Ear Identification, Forensic Identification Series*. Paramont Publishing, E.U.A., 1989.

[42] Idesia's Biometric Technologies. Biometric comparison table, 2006. http://www.idesia-biometrics.com/technology/biometric_comparison_table.html.

[43] J. Illingworth and J. Kittler. A survey of the Hough transform. *Computer Vision, Graphics and Image Processing*, pages 87–116, October 1998.

[44] Institute of Automation, Chinese Academy of Sciences. CASIA iris image database, 2004. http://www.sinobiometrics.com.

[45] International Biometric Group. Independent test of iris recognition technology, 2005. http://www.biometricgroup.com/reports.

[46] International Biometric Group. Which is the best biometric technology?, 2005. http://www.biometricgroup.com/reports/public/reports/best_biometric.html.

[47] Robert Ives, Anthony Guindry, and Delores Etter. Iris recognition using histogram analysis. In *Proceedings of the* 38^{th} *Asilomar Conference on Signals, Systems and Computers*, pages 562–566, Monterrey, November 2004.

[48] Anil K. Jain. *Fundamentals of Digital Image Processing*. Prentice-Hall International Editions, E.U.A., 1989.

[49] Anil K. Jain, A.Ross, and S. Prabhakar. An introduction to biometric recognition. *IEEE Transactions on Circuits and Systems for Video Technology, vol. 14, no. 1*, pages 4–19, January 2004.

[50] Anil K. Jain, R. Bolle, and S. Pankanti. *Personal Identification in networked society,* 2^{nd} *edition*. Kluwer Academic Publisher, E.U.A., 1999.

[51] Anil K. Jain, Lin Hong, and Sharath Pankanti. Biometric identification. *Communications of the ACM, vol. 43, no. 2*, pages 91–98, February 2000.

[52] Anil K. Jain, Sharath Pankanti, Salil Prabhakar, Lin Hong, Arun Ross, and James L. Wayman. Biometrics: A grand challenge. In *Proceedings of the* 17^{th} *International Conference on Pattern Recognition (ICPR04)*, pages 935–942, Cambridge, December 2004.

[53] Vaclav Matyas Jr. and Zdenek Riha. Toward reliable user authentication through biometrics. *IEEE Security and Privacy, vol. 1, no. 3*, pages 45–49, 2003.

[54] Jaemin Kim, Seongwon Cho, and Jinsu Choi. Iris recognition using wavelet features. *Kluwer Academic Publishers, Journal of VLSI Signal Processing, no. 38*, pages 147–256, November 2004.

[55] W. K Kong and D. Zhang. Accurate iris segmentation method based on novel reflection and eyelash detection model. In *Proceedings of the 2001 International Symposium on Inteligent Multimedia, Video and Speech Processing*, pages 263–266, Hong Kong, May 2001.

[56] Wai-Kin Kong and David Zhang. Detecting eyelash and reflection for accurate iris segmentation. *International Journal of Pattern Recognition and Artificial Intelligence, vol. 17, no. 6*, pages 1025–1034, 2003.

[57] Zhanna Korotkaya. Biometric person authentication: Odor, 2006. `http://www.it.lut.fi/kurssit/03-04/010970000/seminars/Korotkaya.pdf`.

[58] Hanna-Kaisa Lammi. Ear biometrics, 2005. `http://www.it.lut.fi/kurssit/03-04/010970000/seminars/Lammi.pdf`.

[59] Lye Liam, Ali Chekima, Liau Fan, and Jamal Dargham. Iris recognition using self-organizing neural network. In *Proceedings of the IEEE 2002 Student Conference on Research and Developing Systems*, pages 169–172, Malasya, June 2002.

[60] Shinyoung Lim, Kwanyong Lee, Okhwan Byeon, and Taiyun Kim. Efficient iris recognition through the improvement of feature vector and classifier. *ETRI Journal, vol. 23, no. 2*, pages 61–70, June 2001.

[61] Simon Liu and Mark Silverman. A practical guide to biometric security technology. *IT Professional, vol. 3, issue 1*, pages 27–32, January 2001.

[62] Zongyi Liu and Sudeep Sarkar. Improved gait recognition by gait dynamics normalization. *IEEE Transactions on Pattern Analysis and Machine Inteligence, vol. 28, no. 6*, pages 863–876, June 2006.

[63] Li Ma, Tieniu Tan, Yunhong Wang, and Dexin Zhang. Personal identification based on iris texture analysis. *IEEE Transactions on Pattern Analysis and Machine Intelligence, vol. 25, no. 12*, pages 2519–2533, December 2003.

[64] Li Ma, Tieniu Tan, Dexin Zhang, and Yunhong Wang. Local intensity variation analysis for iris recognition. *Pattern recognition, vol. 37, no. 6*, pages 1287–1298, 2004.

[65] Li Ma, Yunhong Wang, and Tieniu Tan. Iris recognition based on multichannel gabor filtering. In *Proceedings of the* 5^{th} *Asian Conference on Computer Vision ACCV2002*, pages 279–283, Melbourne, Australia, January 2002.

[66] Li Ma, Yunhong Wang, and Tieniu Tan. Iris recognition using circular symmetric filters. In *Proceedings of the* 25^{th} *International Conference on Pattern Recognition (ICPR02), vol. 2*, pages 414–417, Quebec, August 2002.

[67] Li Ma, Yunhong Wang, and Dexin Zhang. Efficient iris recognition by characterizing key local variations. *IEEE Transactions on Image Processing, vol. 13, no. 6*, pages 739–750, June 2004.

[68] Judith A. Markowitz. Voice biometrics. *Communications of the ACM, vol. 43, no. 9*, pages 66–73, September 2000.

[69] D. Marr and E. Hildreth. Theory of edge detection. In *Proceedings of The Royal Society London, vol. 207*, pages 187–217, 1980.

[70] D. Martin-Roche, C. Sanchez-Avila, and R.Sanchez-Reillo. Iris recognition for biometric identification using dyadic wavelet transform zero-crossing. *IEEE Aerospace and Electronic Systems Magazine, Mag. 17, no. 10*, pages 3–6, 2002.

[71] George K. Matsopoulos, Nicolaos A. Mouravliansky, Konstantinos K. Delibasis, and Konstantina S. Nikita. Automatic retinal image registration scheme using global optimization techniques. *IEEETransactions on Information Technology in Biomedicine, vol. 3, no. 1*, pages 47–60, March 1999.

[72] Sean McHugh. Digital photography tutorials, understanding image noise, 2006. `http://www.cambridgeincolour.com/tutorials.htm`.

[73] J. McRaven, M. Scheutz, Gy. Cserey, V. Andronache, and W. Porod. Fast detection and tracking of faces in uncontrolled environments for autonomous robots using the CNN-UM. In *Proceedings of the IEEE International Workshop on Cellular Neural Networks and their Applications (CNNA 2004)*, pages 196–201, Budapest, July 2004.

[74] J. Mira and J. Mayer. Image feature extraction for application of biometric identification of iris - a morphological approach. In *Proceedings of the* 16^{th} *Brazilian Symposium on Computer Graphics and Image Processing (SIBGRAPI 2003)*, pages 391–398, Brazil, October 2003.

[75] Multimedia University. MMU iris image database, 2004. `http://pesona.mmu.edu.my/ccteo`.

[76] Mario E. Munich and Pietro Perona. Visual identification by signature tracking. *IEEE Transactions on Pattern Analysis and Machine Inteligence, vol. 25, no. 2*, pages 200–217, February 2003.

[77] Alan Muron and Jaroslav Pospisil. The human iris structure and its usages. *Acta Univ. Palacki, Phisica, vol. 39*, pages 87–95, March 2000.

[78] Ales Muron, Peter Kois, and Jaroslav Pospisil. Identification of persons by means of the fourier spectra of the optical transmission binary models of the human irises. *Elsevier Science, Optics Communications, no. 192*, pages 161–167, June 2001.

[79] Kyong Nam, Kyong Yoon, Jun Bark, and Woo Yang. A feature extraction method for binary iris code construction. In *Proceedings of the* 2^{nd} *International Conference on Information Technology for Application*, pages 284–288, China, January 2004.

[80] National Center for State Courts. Biometrics and the courts, 2006. `http://ctl.ncsc.dni.us/biomet%20web/BMIndex.html`.

[81] National Institute of Standards and Technology. CBEFF common exchange biometric file format, 2001. `http://www.itl.nist.gov/div895/isis/bc/cbeff/CBEFF010301web.PDF`.

[82] National Institute of Standards and Technology. Iris challenge evaluation, 2006. `http://iris.nist.gov/ICE/`.

[83] Ko Nishino and Shree K. Nayar. Eyes for relighting. *ACM Trans. Graph., vol 23, no. 3*, pages 704–711, 2004. `http://doi.acm.org/10.1145/1025706.1025783`.

[84] S. Niyogi and E. Adelson. Analyzing gait with spatiotemporal surfaces. In *Proceedings of the IEEE Workshop Non-Rigid Motion*, pages 24–29, Austin, November 1994.

[85] Manuel M. Oliveira, Brian Bowen, Richard McKenna, and Yu-Sung Chang. Fast digital image inpainting. In *Proceedings of the International Conference on Visualization, Imaging and Image Processing (VIIP 2001)*, pages 261–266, Marbella, September 2005.

[86] P. J. Philips, P. Grother, R. J. Micheals, D. M. Blackburn, E. Tabassi, and J. M. Bone. Frvt2002: Overview and summary, 2002. `http://www.frvt.org/FRVT2002/documents.htm`.

[87] P. Jonathon Philips, Hyeonjoon Moon, Syed A. Rizvi, and Patrick J. Rauss. The FERET evaluation methodology for face-recognition algorithms. *IEEE Transactions on Pattern Analysis and Machine Inteligence, vol. 2, no. 10*, pages 1090–1104, October 2000.

[88] Salil Prabhakar, Sharath Pankanti, and Anil K. Jain. Biometric recognition: Security and privacy concerns. *IEEE Security and Privacy, vol. 1, no. 2*, pages 33–42, 2006.

[89] Hugo Proença and Luís A. Alexandre. UBIRIS: A noisy iris image database. In *Proceedings of the* 13^{th} *International Conference on Image Analysis and Processing (ICIAP2005)*, pages 970–977, Calgary, September 2005. `http://iris.di.ubi.pt`.

[90] Hugo Proença and Luís A. Alexandre. Iris recognition: A feature selection method for non-cooperative envirnoments. *submitted to IJIS Springer International Journal of Information Security*, 2006.

[91] Hugo Proença and Luís A. Alexandre. Iris recognition: An analysis of the aliasing problem in the iris normalization stage. In *Proceedings of the 2006 International Conference on Computational Intelligence and Security (CIS2006) (accepted to)*, Guangzhou, November 2006.

[92] Hugo Proença and Luís A. Alexandre. Iris recogniton: Feature extraction and comparison in noisy images. In *Proceedings of the 2006 IEEE International Conference on Computacional Intelligence for Homeland Security and Personal Safety (CIHSPS2006) (accepted to)*, Washington, October 2006.

[93] Hugo Proença and Luís A. Alexandre. Iris segmentation methodology for non-cooperative iris recognition. *IEE Proc. Vision, Image & Signal Processing, vol. 153, issue 2*, pages 199–205, 2006.

[94] Hugo Proença and Luís A. Alexandre. A method for the identification of inaccuracies in the pupil segmentation. In *Proceedings of the* 1^{st} *International Conference on Availability, Reliability and Security (ARES2006)*, pages 227–230, Vienna, April 2006.

[95] Hugo Proença and Luís A. Alexandre. A method for the identification of noisy regions in normalized iris images. In *Proceedings of the* 18^{th} *International Conference on Pattern Recognition (ICPR2006), vol. 4*, pages 405–408, Hong Kong, August 2006.

[96] Hugo Proença and Luís A. Alexandre. Towards non-cooperative iris recognition: A classification approach using multiple signatures. *(submitted to* 2^{nd} *round of reviews) IEEE Transactions on Pattern Analysis and Machine Inteligence*, 2006.

[97] K.H. Pun and Y.S. Moon. Recent advances in ear biometrics. In *Proceeding of the* 6^{th} *IEEE International Conference on Automatic Face and Gesture Recognition*, pages 164–169, Seoul, May 2004.

[98] Trygve Randen and John Håkon Husøy. Filtering for texture classification: a comparative study. *IEEE Transactions on Pattern Analysis and Machine Inteligence, vol. 21, no. 4*, pages 291–310, 1999.

[99] Zdenek Riha and Vaclav Matyas. Biometric authentication systems. Technical report, Faculty of Informatics, Masaryk University, 2000. `http://www.fi.muni.cz/reports/files/older/FIMU-RS-2000-08.pdf`.

[100] Roger Clark. Biometrics and privacy. Technical report, Department of Computer Science, Australian National University, 2001. `http://www.anu.edu.au/people/Roger.Clarke/DV`.

[101] A. Ross, S. Crihalmeanu, L. Hornak, and S. Schuckers. A centralized web-enabled multimodal biometric database. In *Proceedings of the 2004 Biometric Consortium Conference (BCC)*, U.S.A, September 2004.

[102] Mark A. Sagar, David Bullivant, Gordon D. Mallinson, and Peter J. Hunter. A virtual environment and model of the eye for surgical simulation. In *Proceedings of the* 21^{st} *Annual Conference on Computer Graphics and Interactive Techniques*, pages 205–212, Orlando, July 1994.

[103] Bruce Schneier. The uses and abuses of biometrics. *Communications of the ACM, vol. 42, no. 8*, page 136, 1999.

[104] J. Shen and S.Castan. An optimal linear operator for edge detection. In *Proceedings of the IEEE International Conference on Computer Vision and Pattern Recognition*, pages 109–114, 1986.

[105] Jianhong Shen. Inpainting and the fundamental problem of image processing. *Siam News, vol. 28, no. 5*, 2003.

[106] Timothy K. Shih and Rong-Chi Chang. Digital inpainting: Survey and multilayer image inpainting algorithms. In *Proceedings of the* 3^{rd} *International Conference on Information Technology and Applications (ICITA 2005)*, pages 25–24, Sydney, July 2005.

[107] Daniel Sieberg. Iris recognition at airports uses eye-catching technology, 2000. `http://archives.cnn.com/2000/TECH/computing/07/24/iris.explainer/index.html`.

[108] D. Smerdon. Anatomy of the eye and orbit. *Current Anaesthesia & Critical Care, vol. 11*, pages 286–292, 2000.

[109] Eric Sung, Xilin Chen, and Jie Yang. Towards non-cooperative iris recognition systems. In *Proceedings of the seventh International Conference on Control, Automation, Robotics and Vision (ICARV'02)*, pages 990–995, Singapore, December 2002.

[110] Systems Development Laboratory, Hitachi, Ltd. Security technology for ubiquitous information society, 2006. `http://www.sdl.hitachi.co.jp/english/news/2006/etrics/13.html`.

[111] Data Core Thecnology. Glossary of terms, 2005. http://www.data-core.com/glossary-of-terms.htm.

[112] Christel Tisse, Lionel Martin, Lionel Torres, and Michel Robert. Person identification technique using human iris recognition. In *Proceedings of the 25th International Conference on Vision Interface*, pages 294–299, Calgary, July 2002.

[113] Mihran Tuceryan. Moment based texture segmentation. *Pattern Recognition Letters, vol. 25*, pages 659–698, July 1994.

[114] University of Bath. University of Bath iris image database, 2004. http://www.bath.ac.uk/elec-eng/pages/sipg/.

[115] UTHSCSA Teacher Enrichment Initiatives. Positively aging® & M.O.R.E. curricular programs, anatomy of the human eye, 2001. http://teachhealthk-12.uthscsa.edu/curriculum/vision-hearing/vision01-anatomy.htm.

[116] Mayank Vatsa, Richa Singh, and A. Noore. Reducing the false rejection rate of iris recognition using textural and topological features. *International Journal of Signal Processing, vol. 2, no. 1*, pages 66–72, 2005.

[117] M. Villani, C. Tappert, Ngo Giang, J. Simone, H.St.Fort, and Cha Sung-Hyuk. Keystroke biometric recognition studies on long-text input under ideal and application-oriented conditions. In *Proceedings of the 2006 Conference on Computer Vision and Pattern Recognition Workshop (CVPRW06)*, pages 39–47, New York, June 2006.

[118] Sen Wang. Personal identification based on biometrics, 2006. http://www.sinc.sunysb.edu/Stu/sewang/project/Personal%20Identification%20Based%20on%20Biometrics.htm.

[119] Wikipedia. Wikipedia, the free encyclopedia. http://en.wikipedia.org/wiki/Biometric.

[120] Richard P. Wildes. Iris recognition: an emerging biometric technology. In *Proceedings of the IEEE, vol. 85, no.9*, pages 1348–1363, U.S.A., September 1997.

[121] John D. Woodward, Christopher Horn Jr., Julius Gatune, and Aryn Thomas. Biometrics: A look at facial recognition. Technical report, Rand Corporation, http://www.rand.org/pubs/documented_briefings/DB396, 2003.

[122] John D. Woodward, Katharine Watkins Webb, Elaine M. Newton, Melissa A. Bradley, David Rubenson, Kristina Larson, Jacob Lilly, Katie Smythe, Brian Houghton, Harold Alan Pincus, Jonathan Schachter, and Paul Steinberg. *Army Biometric Applications - Identifying and Addressing Socio-Cultural Concerns*. Rand Corporation, E.U.A., 2001.

[123] Ming-Hsuan Yang, David J. Kriegman, and Narendra Ahuja. Detecting faces in images: A survey. *Transactions on Pattern-Analysis and Machine Intelligence, vol. 24, no. 1*, pages 34–58, January 2002.

[124] Xiaoyan Yuan and Pengfei Shi. A non-linear normalization model for iris recognition. In *Proceedings of the International Workshop on Biometric Recognition Systems IWBRS 2005*, pages 135–142, Beijing, October 2005.

[125] Yau Wei Yun. The "123" of biometric technology. *Synthesis Journal 2002*, 2002.

[126] W. Zhao, R. Chellappa, P. J. Phillips, and A. Rosenfeld. Face recognition: A literature survey. *ACM Computing Surveys, vol. 35, issue 4*, pages 399–458, December 2003.

[127] Yong Zhu, Tieniu Tan, and Yunhong Wang. Biometric personal identification based on iris patterns. In *Proceedings of the* 13^{th} *International Conference on Pattern Recognition (ICPR00)*, pages 2801–2804, Barcelona, September 2000.

[128] Zhiwei Zhu and Qiang Ji. Robust real-time eye detection and tracking under variable lighting conditions and various face orientation. *Elsevier Computer Vision and Image Understanding, vol. 98*, pages 125–255, July 2005.

[129] Douglas Zongker and Anil K. Jain. Algorithms for feature selection: An evaluation. In *Proceedings of the* 11^{th} *International Conference on Pattern Recognition (ICPR96)*, pages 18–22, Vienna, August 1996.

Index